Dissertation presented
as a partial requirement for the degree of
Doctor of Science

First Measurement of $\bar{\nu}_\mu$ Induced Charged-Current π^0 Production Cross Sections on Polystyrene at $E_{\bar{\nu}_\mu}$ 2-10GeV

José Luis Palomino Gallo

Advisor:
Hélio da Motta Filho

Centro Brasileiro de Pesquisas Físicas

Rio de Janeiro, December 2012

Dedicated to the memory of Mama Cata.

Acknowledgements

There is a great number of people I would like to thank. First I would like to thank my supervisor Dr. Hélio da Motta. Hélio is an great advisor. He usually let me work things out for myself instead of giving me something already done. Special thanks to Dr. Jorge Morfin, he was very supportive to the Latino group. Many thanks to our spokespersons, Dr. Deborah Harris and Dr. Kevin McFarland, who have been very nice.

To CAPES and CNPQ for the scholarship (2008-2012), the University of Pittsburgh, Department Physics of and Astronomy for my appointment as a Visiting Scholar (2012). Thanks to CBPF administrative staff José de Almeida Ricardo and Elisabete Vicente. To FERMILAB administrative staff Amanda Thompson, Samantha Poeppelman, Kappatolia Sherman, Barbara Book, Crae Tate, Jackie Cyko and Cheryl Patrick.

This work would not have been possible without the help and support of the electromagnetic final state working group: Dr. Vittorio Paolone, Dr. Steven Mainly, Giuliano Maggi,Dr. Trung Lee, Cesar Sotelo, Jeremy Wolcott, and Jaewon Park. I want to thank my MINERνA fellow collaborators with a special thank to Dr. Dave Schmitz, Dr. Gabriel Perdue, Dr. Jyotsna Osta, Brian Tice for all the help. This work is mostly based on the brilliant reconstruction developed by all the collaborators. Many people have contributed to the success of my thesis.

To my true love, my lovely wife Ruth. I could not have achieved this without your support and enthusiasm, and I do not have the right words to fully describe my gratitude but to say thank you baby.

To my wise mother Esther, who educated me and taught me to respect people. She always took care of me. I love you Mother. To my sisters Cielana and Belen, whom I adore and who were always encouraged me to keep fighting for a better future. To my nieces Illariy and Killay who always make me smile. To my china Chola, a very important woman in my life.

I would also like to thank my CBPF colleagues. My great friend David martinez. He is kind of crazy and the nicest person that I have ever met. Cesar Sotelo and Arturo Fiorentini, great students and great partners. It was a great pleasure have worked with you guys.

To the Ponce Calero family, they are kind persons and very supportive, thanks.

I enjoyed learning a lot of new things during my stay at FERMILAB. We met a lot of new friends, Bari, Anatoli, Sergei, Brandon, Hector, Salvador, Fabiola and O'Sheg. Aaron, Miroslava, Lili, Ivan, Jorge (Yorsh), Enrique, Roger, Noemi, Juan Pablo (Cuervo), Guillermo (Boludo), Edgar, Hector, Juan Carlos, Carlos (Caldo de Paloma), Soraya, Cesar (Pollack), Alfonzo (Peye), Mike, Farinaldo, Rafaela, Andres, Norma and Laza.

Abstract

Understanding of the π^0 production via anti-neutrino-nucleus charged current interaction in the neutrino energy region of 1-10 GeV is essential for neutrino oscillation experiments. In this thesis, we present a measurement of charged current π^0 production from anti-muon neutrinos scattering on a polystyrene scintillator (CH) target in the MINERνA experiment. A method for selecting and reconstructing $CC\pi^0$ events is presented. The π^0 and μ^+ are fully reconstructed in the final state allowing for the measurement of the final state kinematics and the neutrino energy. We describe the two methods developed in this analysis for π^0 reconstruction in the MINERvA experiment: Hough Transform and Angle Scan. Interacting neutrinos have energy $\sim 3.0GeV$ and π^0 have energy $\sim 0.3GeV$. The total $CC\pi^0$ inclusive cross-section is presented as a function of neutrino energy and Q^2. The total $CC\pi^0$ exclusive cross-section is presented as a function of neutrino energy, Q^2 and the final state kinematics. Cross Section ratio between $CC\pi^0$ exclusive and $CC\pi^0$ inclusive for data and Monte Carlo are presented. Neutrino beam data corresponding to 1.019×10^{20} protons on target have been analyzed. For $CC\pi^0$ inclusive sample we reconstructed 891 events, and for $CC\pi^0$ exclusive sample we reconstructed 514 events.

MINERνA Collaboration

I.Albayrak[7],L. Aliaga[15],M. Andrews[5],S. Avvakumov[16], B. Baldin[5],J.L. Bazo[15],G. Blazey[12], A. Bodek[16], D. Boehnlein[5],S. Boyd[14], R. Bradford[16],W.K. Brooks[10], A. Bruell[10], D. Buchholtz[13], H. Budd[16],D. Casper[3],C. Castromonte[2],D. Cherdack[19],M.E. Christy[7], J. Chvojka[16],M.A.C. Cummings[12],D.S. Damiani[21],D. Drakoulakos[1],S. Dytman[14],R. Ent[10], G.A.Fiorentini[2],J. Felix[6],R. Flight[16],A. Gago[15],H. Gallagher[19],D. Gaskell[10],R. Gilman[17], C. Gingu[5],C. Glasshausser[17],R. Gran[11], N. Grossman[5],D. A. Harris[5],X. Jiang[17],T. Kafka[19], C.E Keppel[7],J. Kilmer[5],S. M.S. Kim[14],Kopp[18], M. Kostin[5],S.Kulagin[8],G. Kumbartzki[17], L. Loiacano[18],S. Manly[16], W.A. Mann[19],K. McFarland[16],D. Meekins[10],W. Melnitchouk[10], G. Moreno[6],J.G. Morfin[5],H. da Motta[2],D. Naples[14],J.K. Nelson[21], G. Niculescu[9], I. Niculescu[9],R. Ochoa[20],W. Oliver[19],J.L.Palomino[2],V. Paolone[14],J. Park[16],E. Paschos[4], O. Pereyra[20],A. Pla-Dalmau[5],M. Proga[18],R. Ransome[17],M. A. Reyes[6],P. Rubinov[5], V. Rykalin[12],W. Sakumoto[16],P. Shanahan[5],H. Schellman[13],R.M. Schneider[21],E. Schulte[17], C. Simon[3],J. Solano[20],P. Spentzouris[5],P. Stamoulis[1],J. Steinman[16],J. Tatar[3],V. Tvaskis[7], G. Tzanakos[1],M. Vaz[2],S. Wood[10],G. Zavala[6],B. Ziemer[3],M. Zois[1]

University of Athens, Athens, Greece[1]

Centro Brasileiro de Pesquisas Fisicas, Rio de Janeiro, Brazil[2]

University of California, Irvine, California[3]

University of Dortmund, Dortmund, Germany[4]

Fermi National Accelerator Laboratory, Batavia, Illinois[5]

Universidad de Guanajuato, Guanajuato, Mexico[6]

Hampton University, Hampton, Virginia[7]

Institute for Nuclear Research, Moscow, Russia[8]

James Madison University, Harrisonburg, Virginia[9]

Jefferson Lab, Newport News, Virginia[10]

University of Minnesota Duluth, Duluth, Minnesota[11]

Northern Illinois University, DeKalb, Illinois[12]

Northwestern University, Evanston, IL[13]

University of Pittsburgh, Pittsburgh, Pennsylvania[14]

Pontificia Universidad Catolica del Peru, Lima, Peru[15]

University of Rochester, Rochester, New York[16]

Rutgers University, New Brunswick, New Jersey[17]

University of Texas-Austin, Texas[18]

Tufts University, Medford, Massachusetts[19]

Universidad Nacional de Ingenieria. Lima, Peru[20]

William and Mary College, Williamsburg, Virginia[21]

Contents

List of Figures

List of Tables

Chapter 1

Introduction

Neutrino physics has been a very active field both experimentally and theoretically. Neutrinos play a very important role in various branches of subatomic physics as well as in astrophysics and cosmology. Currently there is evidences that neutrinos have mass [1] and can change flavor [2].

In this thesis we describe our work in the Main Injector Neutrino Experiment for $\nu - A$, known as MINERνA , a neutrino scattering experiment that uses Fermilab NuMI beamline. This thesis presents the first measurement of cross-sections for $\bar{\nu}$-Induced Charged-Current π^0 Production, for both inclusive and exclusive processes.

Chapter 2 introduces basic aspects of neutrino physics and briefly describes the history of neutrino from its theoretical conception to the present day.

Chapter 3 describes the NuMI beamline and the MINERνA experiment.

Chapter 4 describes the two methods that have been developed for identification and reconstruction of π^0's (Hough Transform and Angle Scan) and then analytically compares both algorithms to maximize the reconstruction in the $0 - 2\ MeV$ region.

Chapter 5 describes the simulation, event reconstruction and the event selection.

Chapter 6 presents the calculation of the cross-section for $CC\pi^0$ inclusive and $CC\pi^0$ exclusive as a function of the neutrino energy, Q^2, π^0 energy and the angle between π^0 and $\bar{\nu}_\mu$.

Chapter 7 summarizes our results and presents the conclusions.

We add three appendixes to this thesis. Apendix A shows a test of our methods applied to a ν_μ sample. Appendix B shows resolution and quality plots for the analysis. Appendix C describes the method of discriminating between electrons and photons by the deposited energy.

Chapter 2

Neutrino Physics

2.1 History

Neutrinos are light neutral particles that do not interact through the strong nuclear force. When it meets matter, a neutrino travels deep to nucleon, then it either continues on as a neutrino or change to its associated lepton. In 1911, an experiment realized by Von Bayer, Otto Hahn and Lise Meitner [3] suggested that the energy emitted in the β decay has a continuos rather than discrete spectrum. This observation was in contradiction with the energy conservation law since, apparently, there was energy loss in the process.

In 1927 Ellis e Wooster [4] stablished, without doubts, that the energy spectrum of the β decay is, in fact, continuous. In radioactive decays a nucleus changes into different nucleus when a neutron decays into a proton with the emission of an electron and an antineutrino.

$$n \rightarrow p + e + \overline{\nu} \tag{2.1}$$

In the absence of the antineutrino, energy conservation requires the electron and the proton to share the neutron energy. However, experiments showed that those electrons are not monoenergetic but present a continuous energy distribution that corresponds exactly to a 3 particle final state where the particles share the energy.

In an open letter to *Liebe Radioaktive Damen und Herren*[1] in a physics conference in Tubingen, Germany, in 1930 Wolfgang Pauli proposed[5] that the existence of a neutral weakly interacting fermion emitted in the β decay could solve the problem. This neutral fermion, with mass close to the electron mass and no electric charge, was called neutron. When in 1932

[1] Dear Radioactive Ladies and Gentlemen

Chadwick discovered the neutron that we know today[6] Fermi called Pauli's particle neutrino (little neutron) to diferentiate it from the heavy Chadwick's neutron. In 1933 after comparisons between Fermi [7] and Perrin [8] spectrums it was postulated that the neutrino should have no mass.

In 1934 Fermi[9] used Dirac,Heisenberg and Pauli's quantum electrodinamics to formally develop the β decay theory. In 1956 Reines and Cowan[10] made the first direct observation of the neutrino. They employed a nuclear reactor as a source of 1 MeV antineutrinos and a target of water and cadmium chloride to observe the reaction[2]

$$\overline{\nu}_e + p \rightarrow n + e^+ \tag{2.2}$$

In 1958, Goldhaber observed that neutrinos have left hand helicity [11] and in 1959 Davis showed that a ν can be distinguished from its antiparticle $\overline{\nu}$ [12]. In 1960 an experiment by Lederman [13] at the Brookhaven Alternating Gradient Synchrotron(AGS) detected a new type of neutrino, the ν_μ.

In 1973 the Gargamelle giant bubble chamber at CERN announced the experimental observation of the weak neutral currents[14]. Experiments with solar neutrinos began on 1968 when Davis [15] revealed a discrepancy between theoretical predictions and the measured solar neutrino flux. This discrepancy came to be known as the solar neutrino problem.

A discrepancy between the expected and the measured flux was also observed in experiments with atmospheric neutrinos that registered the apparent disappearance of muon neutrinos in a few hundred kilometers of propagation. Experiments that measured the flux of solar neutrinos found results suggesting that electron neutrinos disappeared in the traveling distance between Sun and Earth.

These results led Gribov and Pontecorvo[16], in 1968, to describe neutrino flavor oscillation if the neutrinos have mass. The disappearance of atmospheric neutrinos (ν_μ) and solar neutrinos (ν_e) is not easy to explain in oscillation terms if mass terms are not included. It is important to notice that neutrino oscillation is not predicted by Standard Model.

[2]The very small interaction probability required the very intense flux of antineutrinos provided by the reactor and a very large volume of the target.

It has been a long journey since the pioneers hitherto during which we have witnessed an intense experimental and theoretical activity aimed at a better understanding of neutrino interactions with nucleons and nuclei. The discovery of the neutrinos and neutrino oscillations started a new era of physics.We have found evidences that neutrinos have mass a fact that goes beyond the Standard Model. Many important neutrino beam facilities have been built at JPARC, CERN and Fermilab in the past years aimed at the detailed study of neutrinos.

2.2 Neutrino Properties

Several properties of neutrinos have already been observed and measured like the ones briefly described below.

2.2.1 Neutrino Flavors

The standard model of particle physics contains three neutrino flavors: ν_e, ν_μ and ν_τ. Each neutrino forms a doublet with a corresponding charged lepton. The ν_τ was discovered not even 13 years ago[17]. The number of neutrinos participating in the electroweak interaction can be determined by the Z^0 decay width. It was beautifully confirmed at LEP (CERN)[18, 19, 20, 21], long before the observation of the ν_τ, that there are only three light neutrinos.

In 1995 LSND claimed that three neutrinos were not enough to explain their results and introduced a sterile neutrino [22].This sterile neutrino does not undergo weak interactions nor interacts in any other way (except gravity). MiniBooNE results from late March 2007 showed no evidence of muon neutrino to electron neutrino oscillations in the LSND region, refuting a simple 2-neutrino oscillation interpretation of the LSND results. More advanced analyses of their data are currently being undertaken by the MiniBooNE collaboration.

2.2.2 Helicity

Wu showed in the late 1950s that parity is violated in weak interactions[23] and Goldhaber[11] observed that neutrinos have spin antiparallel to their momentum (left-handed) and antineutrinos have it parallel (right-handed). Therefore, only left-handed neutrinos and right-handed antineutrinos are included in the Standard Model.

2.2.3 Neutrino mass

Currently, the absolute values of the neutrino masses are unknown. The Standard Model assumes that neutrinos are massless. However, no fundamental aspect of the Standard Model

forbids massive neutrinos and it is quite straightforward to insert neutrino mass terms into the Standard Model Lagrangian. There are two basic methods to generate neutrino mass terms that are both gauge and Lorentz invariant[24].

Dirac mass. This is obtained by introducing extremely heavy right-handed neutrinos which have not yet been observed. These neutrinos appear in many Grand Unified Theories. The mass term in the Lagrangian is therefore:

$$\mathcal{L}_{Dirac} = -(\overline{\nu}_L M \nu_R + \overline{\nu}_R M \nu_L), \tag{2.3}$$

where $\nu_{L,R}$ are the neutrino flavour eigenstates and M is the 3x3 neutrino mass matrix.

Majorana mass. A massive Majorana neutrino can be created by modifying the Higgs sector in the Standard Model. An additional singlet, doublet or triplet is added to the original Higgs doublet, although this introduces a new mass scale in the form of the Higgs vacuum expectation value. The mass term in the Lagrangian is:

$$\mathcal{L}_{Majorana} = \frac{1}{2}\overline{\nu}^c_L M \nu_L + h.c. \tag{2.4}$$

In this case neutrinos are their own anti-particles since ν^c_L is a right-handed neutrino. These mass terms violate lepton number conservation by two units and their presence could be indicated by the observation of neutrinodouble beta decay, nuclear transitions of the type,

$$(Z, A) \rightarrow (Z - 2, A) + 2e-, \tag{2.5}$$

which are only possible in the presence of massive Majorana-type neutrinos. The non-observation of this transition in current experiments sets a limit to the mass of the electron neutrino of m_{ν_e} < 0.5eV if the ν_e is assumed to be a Majorana particle.

2.3 Weak Interactions

Since Pauli's prediction of the neutrino, this particle has played an important role in the understanding of the weak interactions. Fermi was the first to include the neutrino in the description of the β-decay process.

In the Standard Model, neutrinos are considered massless and purely left-handed. This is in contrast to the experimental evidence for non-zero mass neutrino as discussed previously. However, even though the non-zero mass is necessary for neutrino oscillations, it is not at all important for neutrino nucleon scattering simply because it is too small. This tiny mass will not affect any of the calculations, therefore, we can assume it to be zero in all that follows.

Historically, the neutrino-lepton charged current and neutral-current interactions have been used to study the nature of the weak force in great detail. The electroweak interaction is part of the Standard Model and is based on a local $SU(2) \times U(1)$ gauge symmetry. After spontaneous symmetry breaking via the Higgs mechanism we get for the interaction part of the Lagrangian,[25]

$$\mathcal{L}_{int} = \mathcal{L}_{CC} + \mathcal{L}_{NC} + \mathcal{L}_{EM} \tag{2.6}$$

The weak charged current (CC) couples with the charged W boson field, the weak neutral current (NC) couples with neutral Z boson and the electromagnetic current(EM) couples with the photon field. The leptonic part of the Langragian is schematically shown in Fig.2.1.

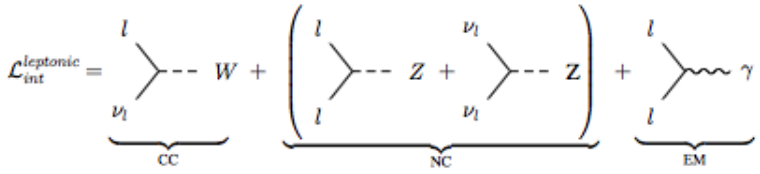

Figure 2.1: Leptonic part of the interaction Lagrangian (l = e, μ or τ)

$\mathcal{L}_{CC}$ is the charged current Lagrangian that couples neutrinos and anti-neutrinos via a $W^{\pm}$ boson to their charged lepton partners and vice versa, is described by equation 2.7.

$$-\mathcal{L}_{CC} = \frac{g}{2\sqrt{2}}\left(j_W^{\mu} W_{\mu} + j_W^{\mu,\dagger} W_{\mu}^{\dagger}\right) \tag{2.7}$$

The second type of interaction, $\mathcal{L}_{NC}$ is the neutral current Lagrangian that couples neutrinos and anti-neutrinos via the Z^0 boson, is given by equation 2.8.

$$-\mathcal{L}_{NC} = \frac{g}{2cos\theta_W} j_Z^{\mu} Z_{\mu} \tag{2.8}$$

, here W_{μ} and Z_{μ} represent the heavy gauge boson field,g is the weak coupling constant, θ_W is the Weinberg angle. These are the only possible neutrino interactions in the Standard Model. Using this formalism, it is possible to articulate all neutrino interactions [26] within this simple framework.

The leptonic charged weak current j_W^{μ} is given by the form,

$$j_W^{\mu} = 2 \sum_{\alpha=e,\mu,\tau} \bar{\nu}_{L,\alpha} \gamma^{\mu} l_{\alpha L} \tag{2.9}$$

The leptonic neutral-current term, j_Z^{μ} , describes the exchange of the neutral boson Z^0,

$$j_Z^{\mu} = 2 \sum_{\alpha=e,\mu,\tau} g_L^{\nu} \bar{\nu}_{\alpha L} \gamma^{\mu} \nu_{\alpha L} + g_L^{f} \bar{l}_{\alpha L} \gamma^{\mu} l_{\alpha L} + g_R^{f} \bar{l}_{\alpha L} \gamma^{\mu} l_{\alpha R} \tag{2.10}$$

Here $\nu_{\alpha L(R)}$ and $l_{\alpha L(R)}$ correspond to the left (right) neutral and charged leptonic fields, while g_L^{ν} , g_L^f , and g_R^f represent the fermion left and right-handed couplings. Table 2.1, details these values.

Fermion	g_L^f	g_R^f	g_V^f	g_A^f
ν_e, ν_μ, ν_τ	$+\frac{1}{2}$	0	$+\frac{1}{2}$	$+\frac{1}{2}$
e, μ, τ	$-\frac{1}{2} + sin^2\theta_W$	$+sin^2\theta_W$	$-\frac{1}{2} + 2sin^2\theta_W$	$-\frac{1}{2}$
u, c, t	$\frac{1}{2} - \frac{2}{3}sin^2\theta_W$	$-\frac{2}{3}sin^2\theta_W$	$\frac{1}{2} - \frac{4}{3}sin^2\theta_W$	$+\frac{1}{2}$
d, s, b	$-\frac{1}{2} + \frac{1}{3}sin^2\theta_W$	$+\frac{1}{3}sin^2\theta_W$	$-\frac{1}{2} + \frac{2}{3}sin^2\theta_W$	$-\frac{1}{2}$

Table 2.1: Values for g_V (vector), g_A (axial), g_L (left) and g_R (right) coupling constants for the known fermion fields

2.4 Neutrino in the Standard Model

The standard model is the theory that describes fundamental particles and how they interact. The standard model is conceptually simple and comprehensive. It is a most succesful theory with various measurements confirming its predictions. It is, however, incomplete since it does not describe everything (gravity, for instance, is not included). The Standard model is only able to describe three of the four forces[3].

Everything around us is made of matter particles and complex interactions, that could be explained with only 6 quarks, 6 leptons and force carrier particles, see table 2.2, Quarks and Leptons consist of six particles, which are related in pairs, or generations. The lightest and most stable particles make up the first generation, whereas the heavier and less stable particles belong to the second and third generations. Force carrier particles (bosons) mediate the interactions: gluons for the strong interaction; $W^{\pm}$ and Z^0 for the weak interaction and the photon for the electromagnetic interaction.

The Standard Model (SM) is based on the gauge group, with three fermion generations, where a single generation consists of five different representations of the gauge group equation 2.11

$$GSM = SU(3)_C \times SU(2)_L \times U(1)_Y \tag{2.11}$$

[3]the strong force, the weak force and the electromagnetic force

QUARKS		
Quarks	Mass	Electric charge
up (u)	$2.3^{+0.7}_{-0.5}$ MeV/c^2	$+\frac{2}{3}$
down (d)	$4.8^{+0.7}_{-0.3}$ MeV/c^2	$-\frac{1}{3}$
strange (s)	95±5 MeV/c^2	$-\frac{1}{3}$
charm (c)	1.275±0.025 GeV/c^2	$+\frac{2}{3}$
bottom (b)	4.65±0.03 GeV/c^2	$-\frac{1}{3}$
top (t)	173.5±0.6 ± 0.8 GeV/c^2	$+\frac{2}{3}$
LEPTONS		
Leptons	Mass	Electric charge
electron (e)	0.510998928 ± 0.000000011 MeV/c^2	-1
electron neutrino (ν_e)	< 2 eV/c^2	0
muon (μ)	105.6583715 ± 0.0000035 MeV/c^2	-1
muon neutrino (ν_μ)	< 0.19 MeV/c^2	0
tau (τ)	1776.82 ± 0.16 MeV/c^2	-1
tau neutrino (ν_τ)	< 18.2 MeV/c^2	0
BOSONS		
Bosons	Mass	Electric charge
photon(γ)	$< 1 \times 10^{-18}$ eV/c^2	0
W$^\pm$	80.385± 0.015 GeV/c^2	±1
Z^0	91.1876 ± 0.0021 GeV/c^2	0
gluon (g)	0	0
Higgs	125 GeV/c^2	0

Table 2.2: Particles in the SM [27] [28] [29]

The Standard Model of weak and electromagnetic interactions was first proposed in 1967 by A.Salam[30] and S.Weinberg[31]. The neutrino interactions within the SM are given by equations 2.7 2.8 where SM has three active neutrinos. The neutrinos reside in six left-handed weak isospin doublets[4] and nine right-handed singlets, see table 2.3, where N_ν is the number of neutrino flavors.

L_L(1,2,-1/2)	Q_L(3,2, 1)	E_R(1,1,-1)	U_R(3,1, 2/3)	D_R(3,1,-1/3)
$\binom{\nu_e}{e}_L$	$\binom{u}{d}_L$	e_R	u_R	d_R
$\binom{\nu_\mu}{\mu}_L$	$\binom{c}{s}_L$	μ_R	c_R	s_R
$\binom{\nu_\tau}{\tau}_L$	$\binom{t}{b}_L$	τ_R	t_R	b_R

Table 2.3: Three matter fermion generations. Each generation consists of five different representations of the gauge group

The measurement of the decay width of the Z^0 boson into neutrinos makes the existence of three, and only three, light (that is, $m_\nu < m_Z/2$) active neutrinos an experimental fact. When expressed in units of the SM prediction for a single neutrino generation, one gets:

$$\begin{aligned} N_\nu &= 2.994 \pm 0.012 \qquad \text{(Standard Model fits to LEP data)} \\ N_\nu &= 3.00 \pm 0.06 \qquad \text{(Direct measurement of invisible Z width)} \end{aligned} \tag{2.12}$$

2.5 Oscillation

The discovery of non-zero neutrino masses is closely related to the discovery of neutrino oscillations. Neutrino oscillations are only possible with massive neutrinos due to a distinction between flavor and mass eigenstates. The idea was first introduced by Gribov and Pontecorvo[16]. The principle is analogous to the time evolution of a classical coupled oscillator starting with an excitation that is not a normal mode. For simplicity we consider a system with only two neutrinos. Neutrinos produced in charged current interactions are flavor eigenstates denoted as ν_e and ν_μ. Those eigenstates have no well defined mass and are linear superpositions of the mass eigenstates ν_1 and ν_2 with masses m_1 and m_2, respectively:

$$|\nu_e\rangle = |\nu_1\rangle cos\theta + |\nu_2\rangle sin\theta, \tag{2.13}$$

$$|\nu_\mu\rangle = -|\nu_1\rangle sin\theta + |\nu_2\rangle cos\theta, \tag{2.14}$$

[4]the right-handed neutrinos are not included in the SM because the neutrinos interact only weakly and are presumed massless in the model.

where θ is the neutrino mixing angle. At time t = 0 we have a pure weak eigenstate, say $|\nu(0)\rangle = |\nu_\mu\rangle$. But ν_μ is a superposition of the mass eigenstates each of which is propagating with the time dependence dictated by the free Hamiltonian. Therefore at a time t the state will be given by

$$|\nu(t)\rangle = -|\nu_1\rangle sin\theta e^{-iE_1 t} + |\nu_2\rangle cos\theta e^{-iE_2 t}, \tag{2.15}$$

where $E_{1,2} = \sqrt{(p^2 + m_{1,2}^2)} \sim p + \frac{m_{1,2}^2}{2p}$. The probability of finding a neutrino with electron flavor is then

$$\begin{aligned} P(\nu_\mu \to \nu_e; t) &= |\langle \nu_e | \nu(t) \rangle|^2 \\ &= sin^2\theta cos^2\theta | - e^{-iE_1 t} + e^{-iE_2 t}|^2 \\ &= sin^2\theta cos^2\theta sin^2 \left(\frac{\Delta m^2 t}{4E} \right) \\ &= sin^2\theta cos^2\theta sin^2 \left(\frac{\Delta m^2 L}{4E} \right) \end{aligned} \tag{2.16}$$

where $\Delta m^2 = m_2^2 - m_1^2$ is the squared mass difference and $E = p$. The last equation is valid for highly relativistic particles ($L = t$) with L being the travelled distance.

Note that only the mass difference squared appears, hence measuring oscillation probabilities will not give absolute values of the neutrino masses, it can only say definitely that at least one of the two neutrinos has a non-zero mass. The two-flavor-oscillation scheme can be easily extended to three flavor mixing. The neutrino mixing Pontecorvo-Maki-Nakagawa-Sakata matrix then contains three angles θ_{12}, θ_{13}, θ_{23}, one Dirac CP violating phase and possibly two Majorana phases. Further we have three squared mass differences: Δm_{12}^2, Δm_{13}^2, Δm_{23}^2 Since the off-diagonal matrix elements seem to be large, also CP violation might be larger than in the quark sector.

2.6 Neutrino Interactions

To describe neutrino interactions, we must mention general information coming from D. Schmitz talk on neutrinos [32]. "Everything we see around us is made of only three particles: protons, neutrons and electrons". So, a natural question rises: is the entire universe made only of these three particles. We know that for every proton, neutron or electron, the universe contains 1 billion neutrinos. If we talk about the probability that a neutrino interacts with matter, we must take a deep breath and digest the idea that a typical neutrino from the Sun would pass right through 10 quintillion people standing in line and not interact with any of

them. Neutrinos are not rare in the universe; therefore it is important have a comprehensive knowledge about them.

In the last decades, scientists have detected and measured neutrinos from a variety of sources, both natural and man-made. Knowledge of the neutrino interaction cross sections is an important and necessary key in any measurement of neutrinos. With the advent of new precision experiments, like MINERνA , the demands on our understanding of neutrino interactions is increasing.

There is a summary of all neutrino interactions [33], where the authors, first establish the formalism of neutrino interactions by considering the simplest case of neutrino-electron scattering, then they shift to neutrino interaction cross sections at,

Thresholdless processes: $E_\nu = 0 - 1MeV$

Low-energy nuclear processes: $E_\nu = 1 - 100MeV$

Intermediate energy cross sections: $E_\nu = 1 - 20GeV$

High-energy cross sections: $E_\nu = 20 - 500GeV$

Ultra-high-energy neutrinos: $E_\nu = 0.5TeV - 1EeV$

We concentrate our study in the intermediate energy[5] where several distinct neutrino scattering mechanisms start to play a role. The options fall into three main categories:

- **Elastic and quasielastic scattering:** Neutrinos can elastically scatter off an entire nucleon liberating a nucleon (or multiple nucleons) from the target. In the case of charged current neutrino scattering, this process is called as "quasielastic scattering" and for neutral-current scattering this is traditionally referred to as "elastic scattering".

- **Resonance production:** Neutrinos can excite the target nucleon to a resonance state. The resulting baryonic resonance decays to a variety of possible mesonic final states producing combinations of nucleons and mesons.

- **Deep inelastic scattering:** Given enough energy, the neutrino can resolve the individual quark constituents of the nucleon. This is called deep inelastic scattering and manifests with the creation of a hadronic shower.

[5]This energy range is often called as the "transition region" because it corresponds to the boundary between quasielastic scattering on the one end and deep inelastic scattering on the other

As a result of these competing processes, the final state may include particles of neutrino interactions from the emission of nucleons to more complex final states including pions, kaons, and collections of mesons.

In order to better understand these neutrino cross sections, new experiments such as KEK to Kamioka (K2K), Mini Booster Neutrino Experiment (MiniBooNE), Main INjector ExpeRiment: nu-A (MINERνA), Main Injector Neutrino Oscillation Search (MINOS), Neutrino Oscillation MAgnetic Detector (NOMAD), SciBar Booster Neutrino Experiment (SciBooNE), and Tokai to Kamioka experiment (T2K) have started to study this intermediate energy region in greater detail. New theoretical approaches have also recently emerged.

2.6.1 Quasielastic scattering

For neutrino energies less than $2GeV$, neutrino-hadron interactions are predominantly quasielastic (QE). In a charged current neutrino QE interaction, the target neutron is converted to a proton. In the case of an antineutrino scattering, the target proton is converted to a neutron,

$$\nu n \rightarrow \mu^{-} p, \qquad \bar{\nu} p \rightarrow \mu^{+} n \tag{2.17}$$

The main interest in experiments between 1970-1990, was testing the vector-axial vector (V-A) nature of the weak interaction and in measuring the axial-vector form factor of the nucleon, topics that were considered particularly important in providing an anchor for the study of NC interactions.

Several experiments relied heavily on the formalism first written down in [34]. The Quasielastic differential cross section[6] can be expressed as

$$\frac{d\sigma}{dQ^2} = \frac{G_f^2 M^2}{8\pi E_\nu^2}\Big[A \pm \frac{s-u}{M^2}B + \frac{(s-u)^2}{M^4}C\Big] \tag{2.18}$$

where (-)+ refers to (anti)neutrino scattering, G_F is the Fermi coupling constant, Q^2 is the squared four-momentum transfer ($Q^2 = -q^2 > 0$), M is the nucleon mass, m is the lepton mass, E_ν is the incident neutrino energy, and $s - u = 4ME_\nu - Q^2 - m^2$. The factors A, B, and C are functions of the familiar vector, F1 and F2, axial-vector F_A, and pseudoscalar F_P form factors of the nucleon.

For the axial-vector form factor, it was customary to assume a dipole form, equation 2.19, which depends on two empirical parameters: the value of the axial-vector form factor at $Q^2 = 0$, $g_A = F_A(0) = 1.2694 \pm 0.0028$ and the value of the Axial mass (M_A).

[6] In the case of QE scattering off free nucleons

$$F_A(Q^2) = \frac{g_A}{(1 + Q^2/M_A^2)^2} \tag{2.19}$$

Values of M_A ranging from 0.65 GeV to 1.09 GeV were obtained in the period from the late 1960s to early 1990s. By the end of this period, the neutrino QE cross section could be accurately and consistently described by V-A theory assuming a dipole axial-vector form factor with $M_A = 1.026 \pm 0.021 GeV$[35]. Most neutrino experiments use a relativistic Fermi-gas model [36], when simulating their QE scattering event. Other approaches have been developed in recent years to incorporate more sophisticated treatments, the added nuclear effects tend to reduce the predicted neutrino QE cross section beyond the Fermi-gas model, typically on the order of $10\% - 20\%$.

Figure 2.2 summarizes the existing measurements of ν_μ QE scattering cross sections as a function of neutrino energy.

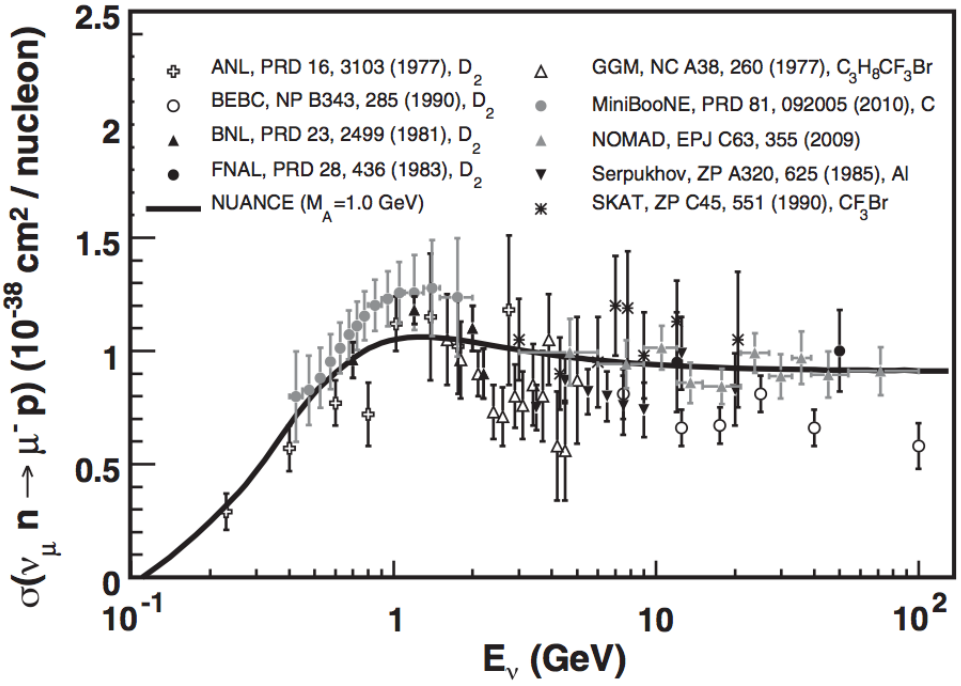

Figure 2.2: Cross section, $\nu_\mu n \to \mu^- p$, as a function of neutrino energy on a variety of nuclear targets. The free nucleon scattering prediction assuming $M_A = 1.0 GeV$ is shown for comparison

Figure 2.3 shows the status of measurements of the corresponding antineutrino QE scattering cross section. Recent results from the NOMAD experiment have expanded the reach out to higher neutrino energies, however, there are currently no existing measurements of the antineutrino QE scattering cross section below 1 GeV.

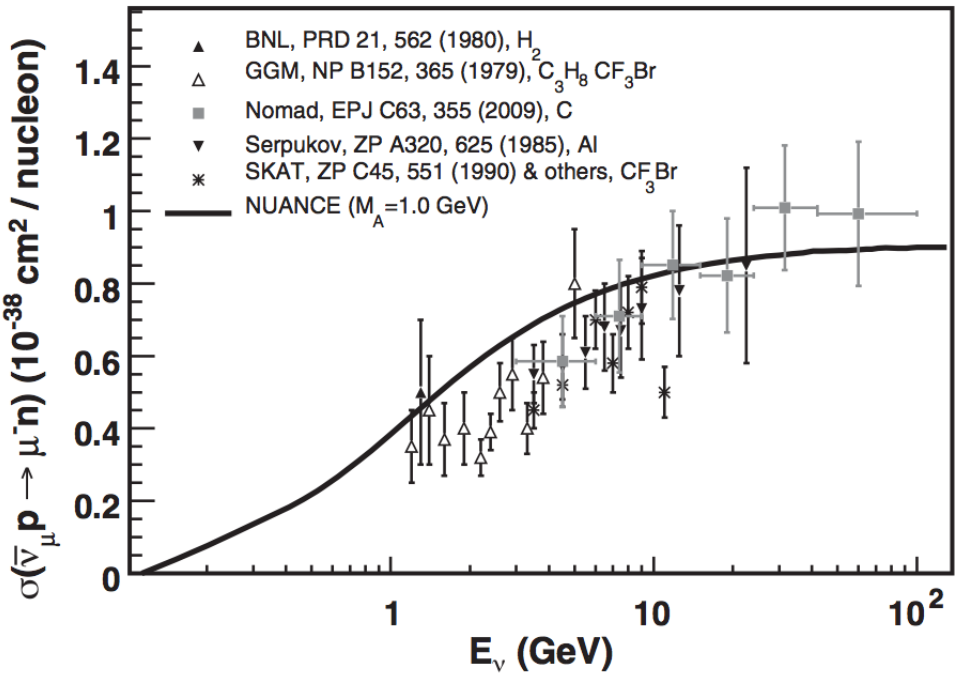

Figure 2.3: Cross section, $\bar{\nu}_\mu p \to \mu^+ n$, as a function of neutrino energy on a variety of nuclear targets.

2.6.2 Resonant single pion production

We need to consider another interaction, an inelastic interaction. Neutrinos can excite the struck nucleon to an excited state. In this case, the neutrino interaction produces a baryon resonance (N^*). The baryon resonance quickly decays, most often to a,

$$\nu N \to \mu^- N^*, \qquad N^* \to \pi N' \tag{2.20}$$

In scattering off of free nucleons, there are seven possible resonant single pion reaction channels, three charged current, see 2.21, 2.22 and 2.23

$$\nu_\mu p \to \mu^- p \pi^+, \qquad \bar{\nu}_\mu p \to \mu^+ p \pi^- \tag{2.21}$$

$$\nu_\mu n \to \mu^- p \pi^0, \qquad \bar{\nu}_\mu p \to \mu^+ n \pi^0 \tag{2.22}$$

$$\nu_\mu n \to \mu^- n \pi^+, \qquad \bar{\nu}_\mu n \to \mu^+ n \pi^- \tag{2.23}$$

, and four neutral current, see 2.24, 2.25, 2.26 and 2.27.

$$\nu_\mu p \to \nu_\mu p \pi^0, \qquad \bar{\nu}_\mu p \to \bar{\nu}_\mu p \pi^0 \tag{2.24}$$

$$\nu_\mu p \to \nu_\mu n\pi^+, \qquad \bar{\nu}_\mu p \to \bar{\nu}_\mu n\pi^+ \tag{2.25}$$

$$\nu_\mu n \to \nu_\mu n\pi^0, \qquad \bar{\nu}_\mu n \to \bar{\nu}_\mu n\pi^0 \tag{2.26}$$

$$\nu_\mu n \to \nu_\mu p\pi^-, \qquad \bar{\nu}_\mu n \to \bar{\nu}_\mu p\pi^- \tag{2.27}$$

Improved measurements and predictions of neutrino-induced single pion production have become important because of the role such processes play in the interpretation of neutrino oscillation data. The Rein and Sehgal model is the most commonly used by Neutrino experiment for calculations. This model gives predictions for both CC and NC resonance production and a prescription for handling interferences between overlapping resonances.

Figures 2.4, 2.5 and 2.6 summarize the historical measurements of CC neutrino single pion production cross sections as a function of neutrino energy.

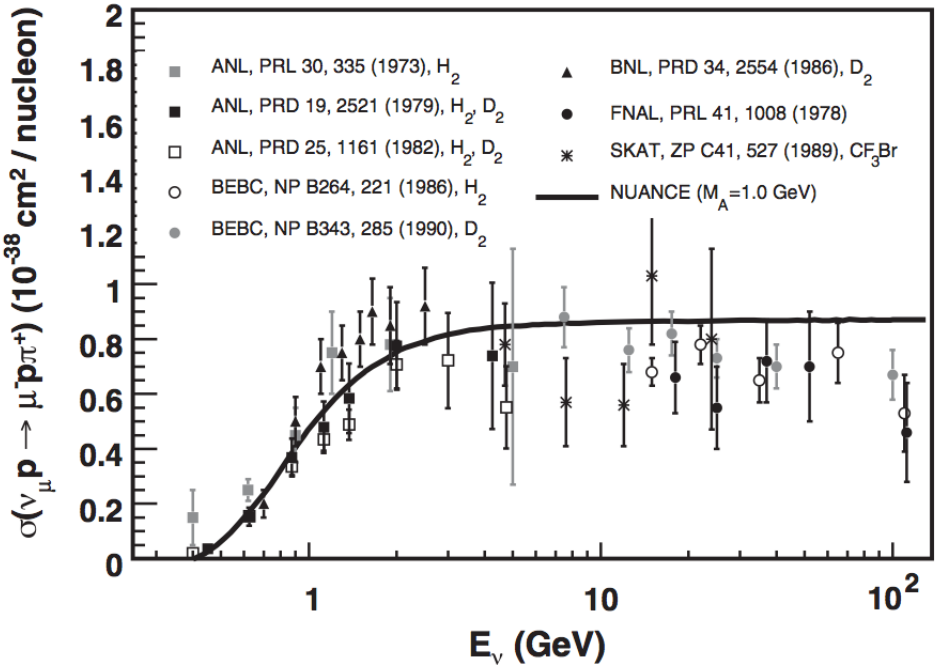

Figure 2.4: Current cross section measurements for the CC process, $\nu_\mu p \to \mu^- p\pi^+$, as a function of neutrino energy.

NC and CC processes producing pion are important for the neutrino physics. $NC\pi^0$ production is often the largest ν_μ-induced background in experiments searching for $\nu_\mu \to \nu_e$ oscillations. $CC\pi$ production processes can present a non-negligible complication in the determination of

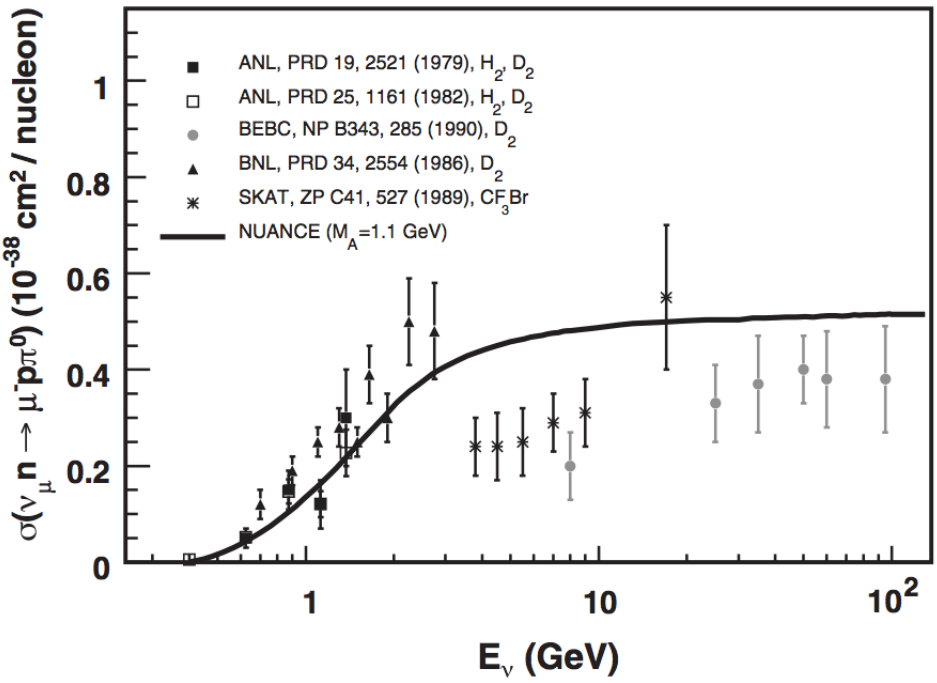

Figure 2.5: Current cross section measurements for the CC process, $\nu_\mu n \to \mu^- p\pi^0$,as a function of neutrino energy.

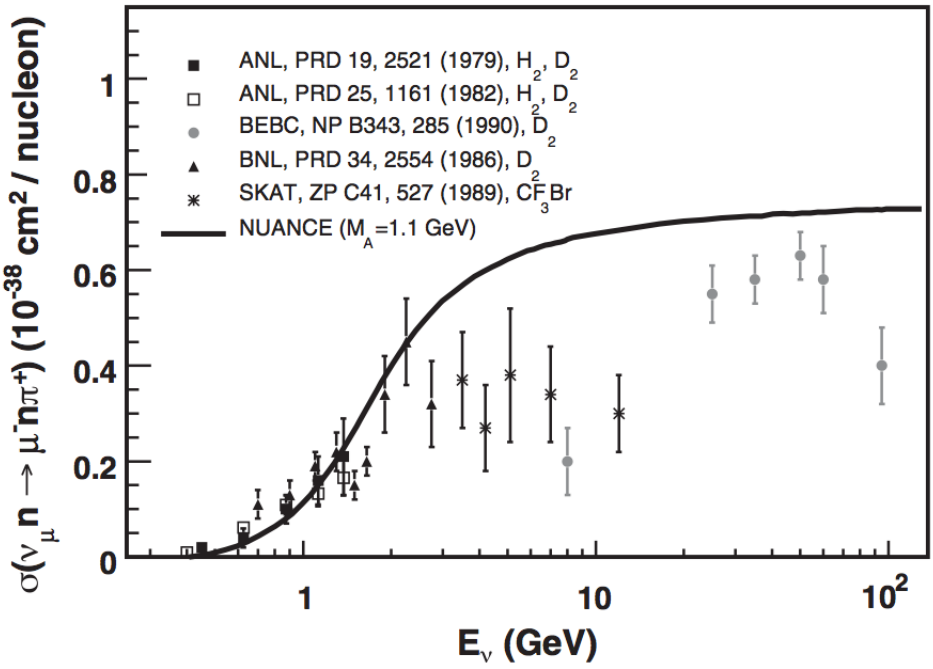

Figure 2.6: Current cross section measurements for the CC process, $\nu_\mu n \to \mu^- n\pi^+$, as a function of neutrino energy.

neutrino energy in experiments measuring parameters associated with ν_μ and $\bar{\nu}_\mu$ disappearance. Also experimental input to the ratio between NC and CC cross section must be taken

Channel	Experiment	Target	No. Events
$\bar{\nu}_\mu p \to \mu^+ p\pi^-$			
	BEBC	D_2	300
	BEBC	H_2	609
	GGM	CF_3Br	282
	FNAL	H_2	175
	SKAT	CF_3Br	145
$\bar{\nu}_\mu n \to \mu^+ n\pi^-$			
	BEBC	D_2	545
	GGM	CF_3Br	266
	SKAT	CF_3Br	178
$\bar{\nu}_\mu p \to \mu^+ n\pi^0$			
	GGM	CF_3Br	179
	SKAT	CF_3Br	83

Table 2.4: Measurements of antineutrino CC $\bar{\nu}$ single pion production from BEBC ([37], [38], [39]), FNAL ([40]), Gargamelle ([41]), and Sepukhov heavy liquid chamber (SKAT) ([42]).

seriously because most of data analyzed exist in that form, [43], [44], [45], [46], [47], [48] and [49]. It should be noted that many of the same baryon resonances that decay to single pion final states can also decay to photons. Such radiative decay processes have small branching fractions ($< 1\%$) yet, like NC π^0 production, they still pose non-negligible sources of background to oscillation searches.

A summary of the corresponding measurements in antineutrino scattering is detailed in table 2.4. Many of these measurements were conducted on light targets and served as a crucial verification of cross section predictions at the time.

Modern experiments have realized the importance of final-state effects, often directly reporting the distributions of final-state particles they observe. Such "observable" cross sections are more useful in that they measure the combined effects of nuclear processes and are much less model dependent. We define our signal, according to final state particles. Table 2.5 lists a collection of some of the most recent pion production cross section reported. Measurements have been produced in the form of both ratios and absolute cross sections, all on carbon-based targets. Similar measurements on additional nuclear targets are clearly needed to help round out our understanding of nuclear effects in pion production interactions.

Experiment	Target	Process	Cross Section
K2K	C_8H_8	$\nu_\mu CC\pi^+/QE$	σ, $\sigma(E_\nu)$
K2K	C_8H_8	$\nu_\mu CC\pi^0/QE$	σ
K2K		$\nu_\mu NC\pi^0/CC$	σ
MiniBooNE	CH_2	$\nu_\mu CC\pi^+/QE$	$\sigma(E_\nu)$
MiniBooNE	CH_2	$\nu_\mu CC\pi^+$	σ, $\sigma(E_\nu)$, $\frac{d\sigma}{dQ^2}$, $\frac{d\sigma}{dT_\mu}$, $\frac{d\sigma}{dT_\pi}$, $\frac{d\sigma}{dT_\mu dcos\theta_\mu}$, $\frac{d\sigma}{dT_\pi dcos\theta_\pi}$
MiniBooNE	CH_2	$\nu_\mu CC\pi^0$	σ, $\sigma(E_\nu)$, $\frac{d\sigma}{dQ^2}$, $\frac{d\sigma}{dE_\mu}$, $\frac{d\sigma}{dcos\theta_\mu}$, $\frac{d\sigma}{dP_\pi}$, $\frac{d\sigma}{dcos\theta_\pi}$
MiniBooNE	CH_2	$\nu_\mu NC\pi^0$	σ, $\frac{d\sigma}{dP_\pi}$, $\frac{d\sigma}{dcos\theta_\pi}$
SciBooNE	C_8H_8	$\nu_\mu NC\pi^0/CC$	σ

Table 2.5: measurements of single pion production by neutrinos. In the last column, refers to a measurement of the total flux- integrated cross section. Measurements are listed from K2K ([50]; [51]; [52]), MiniBooNE ([53]; [54]; [55]; [56]), and SciBooNE ([57]).

2.6.3 Coherent pion production

In addition to resonance production, neutrinos can also coherently produce single pion final states. In this case, the neutrino coherently scatters from the entire nucleus, transferring negligible energy to the target (A). These low$-Q^2$ interactions produce no nuclear recoil and a distinctly forward-scattered pion, compared to their resonance mediated counterparts. Both NC and CC coherent pion production processes are possible,

$$\nu_\mu A \to \nu_\mu A\pi^0, \qquad \bar{\nu}_\mu A \to \bar{\nu}_\mu A\pi^0 \tag{2.28}$$

$$\nu_\mu A \to \mu^- A\pi^+, \qquad \bar{\nu}_\mu A \to \mu^+ A\pi^- \tag{2.29}$$

While the cross sections for these processes are predicted to be comparatively small, coherent pion production has been observed across a broad energy range in both NC and CC interactions of neutrinos and antineutrinos. Figure 2.7 shows the measurements of coherent pion production cross sections for a variety of nuclei.

2.6.4 Summary of CC neutrino and antineutrino cross sections

Many results over CC (anti)neutrino interactions have been accumulated over many decades using a variety of neutrino targets and detector technologies. Figures 2.8 and2.9 summarize the existing measurements of CC neutrino and antineutrino cross sections across this intermediate energy range. Most of our knowledge of neutrino cross sections in this intermediate energy

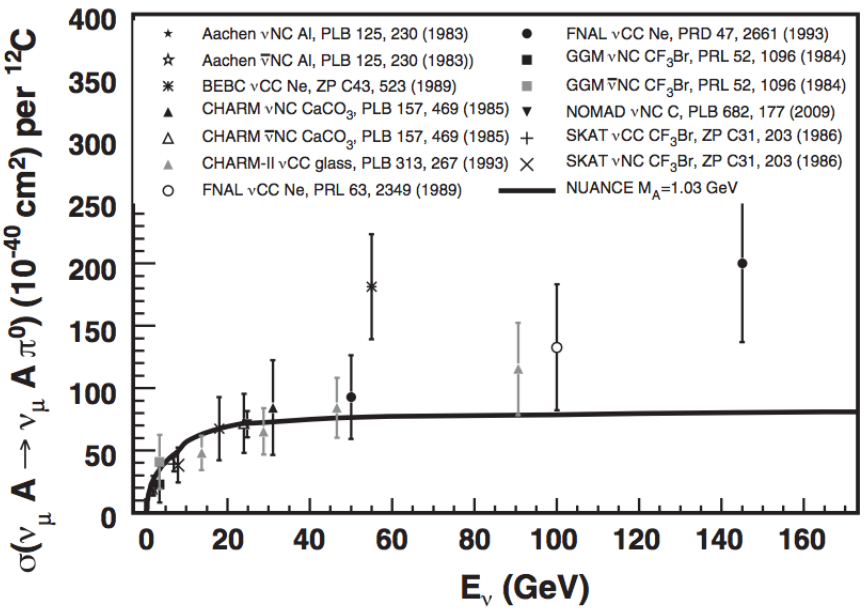

Figure 2.7: Measurements of absolute coherent pion production cross sections from a variety of nuclear targets and samples. Both NC and CC data are displayed on the same plot after rescaling the CC data using the prediction that $\sigma_{NC} = \frac{1}{2}\sigma_{CC}$. In addition, data from various targets have been corrected to carbon cross sections assuming $A^{1/3}$ scaling.

range comes from early experiments that collected relatively small data samples (few thousand events).

Historically, adequate theoretical descriptions of quasielastic, resonance-mediated, and deep inelastic scattering have been formulated; however, there is no uniform description which globally describes the transition between these processes or how they should be combined. Moreover, the full extent to which nuclear effects impact this region is a topic that has only recently been appreciated.

2.6.5 Neutrino Kinematics for $CC\pi^0$

In this dissertation we need to reconstruct the neutrino energy and the momentum transfer (Q^2). For that reason it is important to reconstruct the muon and the two photons that can be used to infer the properties of the incident neutrino (energy and direction).

In order to reconstruct the neutrino energy, we use an approximation given by R. Nelson [58], which replaces the typical lepton momentum used to derive the standard CCQE neutrino energy formula. A $CC\pi^0$ event is of the form,

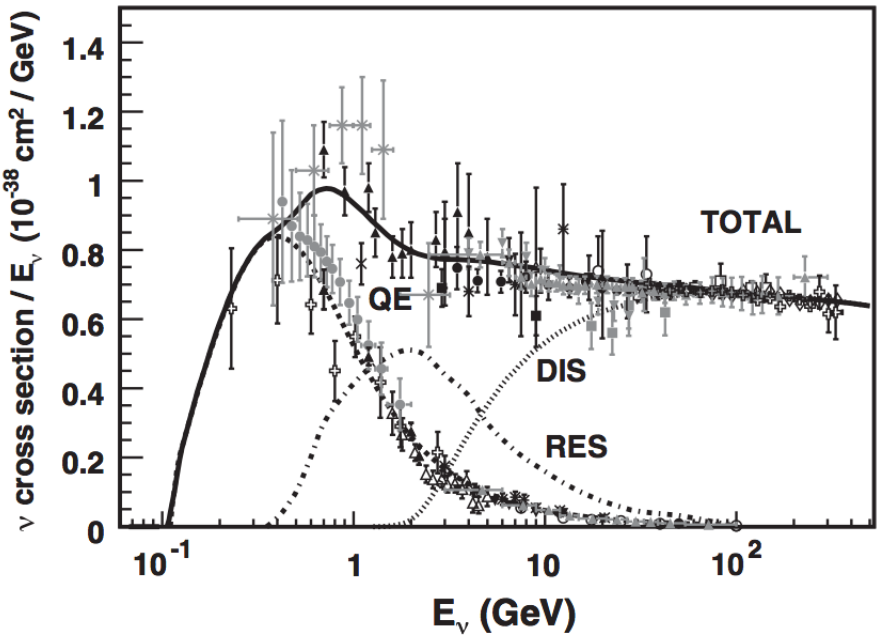

Figure 2.8: Total neutrino per nucleon CC cross sections (for an isoscalar target) divided by neutrino energy as a function of energy. Same data as in Figs(2.2, 2.3), plus additional low energy CC inclusive data from ▲ ([59]), ∗ ([60]), ■ ([61]), and ★ ([62]). Predictions provided by the NUANCE generator.

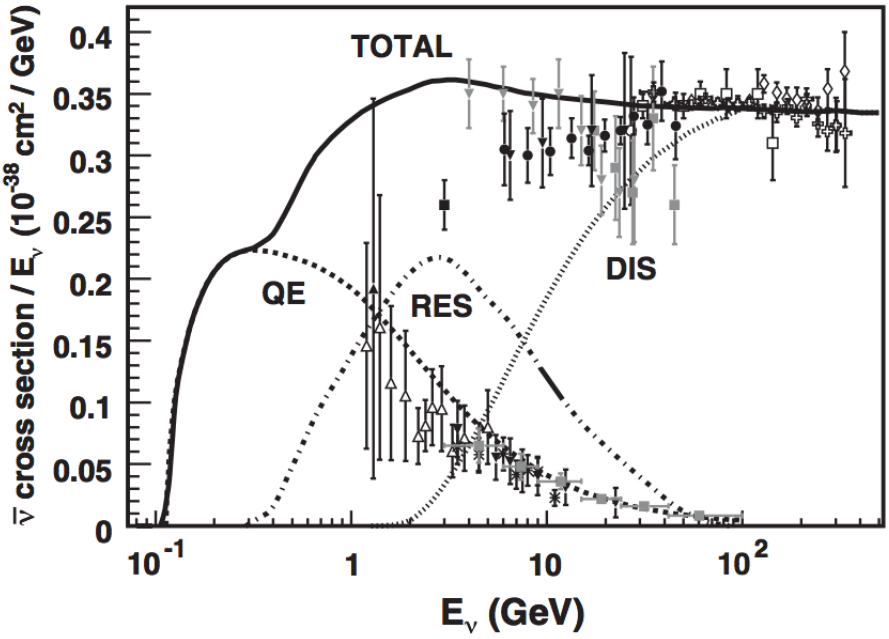

Figure 2.9: Total anti-neutrino per nucleon CC cross sections divided by neutrino energy as a function of energy. Same data as in Figs(2.2, 2.3), plus additional low energy CC inclusive data from ▲ ([59]), ∗ ([60]), ■ ([61]), and ★ ([62]). Predictions provided by the NUANCE generator

$$\begin{aligned} \overline{\nu}_\mu + p &\rightarrow n + \mu^+ + \pi^0 \\ &\rightarrow n + X \end{aligned} \tag{2.30}$$

where $X = \mu^+ + \pi^0$, following momentum conservation $P_{\overline{\nu}_\mu} + P_p = P_n + P_X$

$$\begin{aligned} P_n^2 &= (P_{\overline{\nu}_\mu} + P_p - P_X)^2 \\ m_n^2 &= m_{\overline{\nu}_\mu}^2 + m_p^2 + m_X^2 + 2P_{\overline{\nu}_\mu} \cdot P_p - 2P_{\overline{\nu}_\mu} \cdot P_X - 2P_p \cdot P_X \\ m_n^2 - m_p^2 - m_X^2 &= 2E_{\overline{\nu}_\mu}E_p - 2E_{\overline{\nu}_\mu}E_X + 2E_{\overline{\nu}_\mu}|\overline{P}_X|cos\theta - 2m_pE_X \\ m_n^2 - m_p^2 - m_X^2 + 2m_pE_X &= 2E_{\overline{\nu}_\mu}(m_p - E_X + |\overline{P}_X|cos\theta) \end{aligned} \tag{2.31}$$

which leads to our neutrino energy expression for $CC\pi^0$.

$$E_{\overline{\nu}_\mu} = \frac{1}{2}\frac{m_n^2 - m_p^2 - m_X^2 + 2m_pE_X}{m_p - E_X + |\overline{P}_X|cos\theta} \tag{2.32}$$

The 4-momentum transfer to the hadronic system, Q, is often represented by its relativistic invariant, $Q^2 = -q^2$, where q is the 4-momentum of the $W^\pm$ boson. It is clear that the 4-momentum transfer can be constructed from just the lepton and incoming neutrino energy as,

$$Q^2 = 2E_{\overline{\nu}_\mu}(E_\mu - |p_\mu|cos\theta_\mu) - m_\mu^2 \tag{2.33}$$

If we already estimated the neutrino energy, and, neglecting the muon mass, we can reconstruct Q^2 by:

$$Q^2 = 4E_{\overline{\nu}_\mu}E_\mu sin^2\frac{\theta_\mu}{2} \tag{2.34}$$

Both expression are going to be used in our main reconstruction on $CC\pi^0$ inclusive and $CC\pi^0$ exclusive samples. In this dissertation our energy and Q^2 reconstruction are good enough, in order to calculate our total cross sections and cross section as function of the Q^2.

Chapter 3

MINERvA Experiment

3.1 The NuMI beamline

Fermilab NuMI beamline provides a high intensity ν_μ beam for several experiments like MINOS, MINERνA , NOνA. NuMI neutrinos are the final decay product of charged mesons, most kaons and pions, generated by the collision of 120 GeV protons[1], with a graphite target. Figure 3.1 shows NuMI main parts and components. A detailed description may be found at [63] e [64].

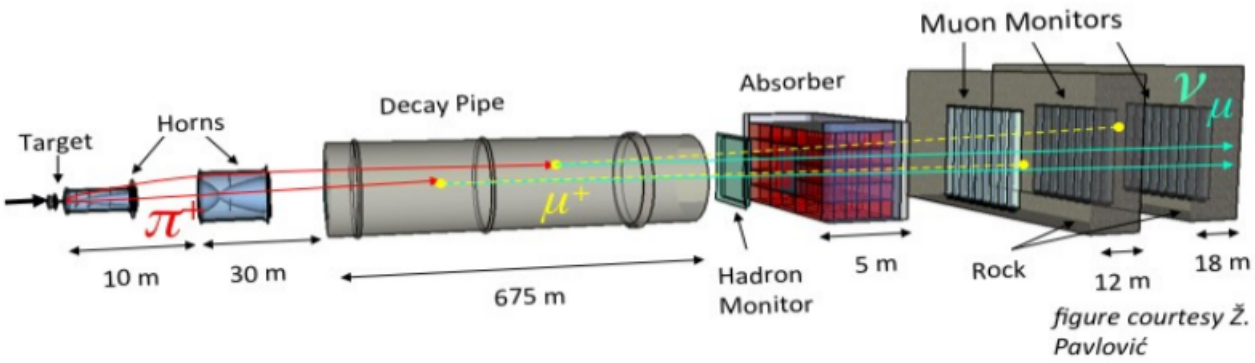

Figure 3.1: NuMI beamline components.

Protons go through several stages before achieving 120 GeV: the LINAC, the booster and the Main Injector. The LINAC accelerates the protons up to 400 MeV and sends them to the booster that accelerates them up to 8 GeV. At the final stage the Main Injector takes the protons to the final 120 GeV. Every 1.9 s a 9.7 μs spill with about $2,5 \times 10^{13}$ protons is extracted and sent towards a $0.95m$ long segmented water cooled graphite target. The target represents

[1] extracted from the Fermilab Main Injector

0.95 interaction lengths to minimize meson production and each segment is 6.4 mm thick to minimize reabsorption.

Positive mesons are focused by magnetic horns acting as parabolic magnetic lenses that create a toroidal field peaking at 3 T. The horns are water cooled and operated by a pulsed 200 kA current [64]. After the horns pions and kaons travel through a vacuum region where they decay producing a μ and a ν_μ. The decay area is a $675m$ long $2m$ diameter cylinder kept at a residual pressure of about 1 Torr or less. Hadrons still present at this stage are stopped at a beam absorber consisting a water cooled aluminum core surrounded by a steel block and an external concrete chamber. The resulting neutrino beam consists of 97,8% ν_μ and few $\bar{\nu_\mu}$ (1.8%) and ν_e (0.4%) the last being the result of the decay of muons.

Figure 3.2 shows the possible energy configurations of the NuMI beam: low energy (LE) and medium energy (ME). Different energies are achieved by changing the distance between the target and the second horn in a movement similar to the lenses of an optical system[2] Pions and kaons of different momenta are selected and focused in the decay region resulting in different energy spectra.

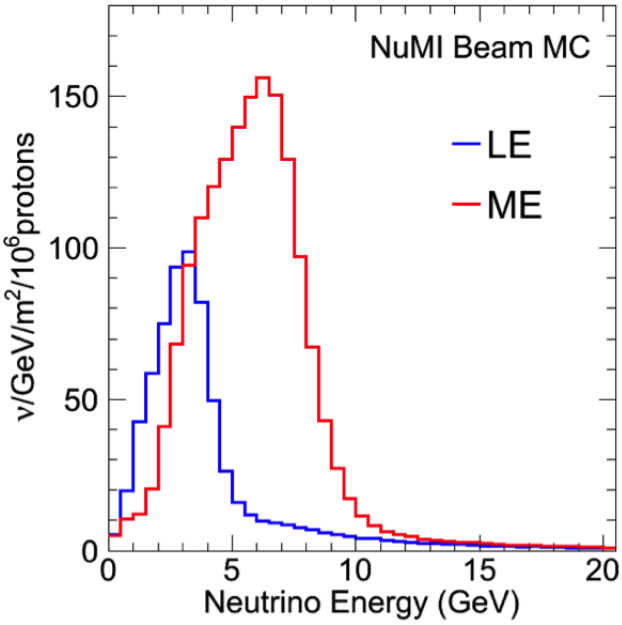

Figure 3.2: NuMI configurations. Low Energy and Medium Energy, plot generated with FLUKA [65]

[2] The target is assembled on a system of rails that allows moving the target for a distance of $2.5m$.

Changing the horns polarization makes mesons of the opposite signal to be focused so the NuMI can have a beam of neutrinos or antineutrinos. NuMI provides an intense beam for the MINOS experiment whose near detector is housed in an experimental hall 100 m underground at FERMILAB grounds. MINERνA detector is placed just upstream the MINOS near detector.

3.2 The MINERνA detector

MINERνA main objective is to study neutrino scattering with matter with high statistics. MINERνA must be able to:

- identify muons and measure their momenta with precision;
- identify hadrons and π^0 and measure their momenta;
- measure hadronic and electromagnetic showers;
- distinguish neutral current and charged current interactions;

Figure 3.3 shows the MINERνA detector in the experimental hall 100 m underground.

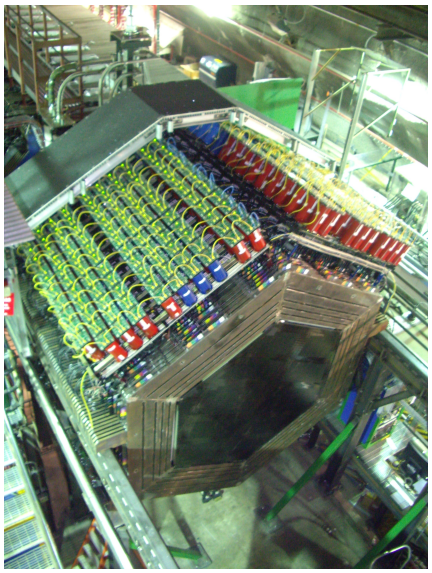

Figure 3.3: Top view of the MINERνA detector.

The MINERνA detector, shown schematically in figure 3.4, consists basically of two subdetectors: the Inner Detector and the Outer Detector. The Inner Detector itself is subdivided in four subdetectors:

- Nuclear targets;

- Active target;
- Electromagnetic calorimeter (ECAL);
- Hadronic calorimeter (HCAL).

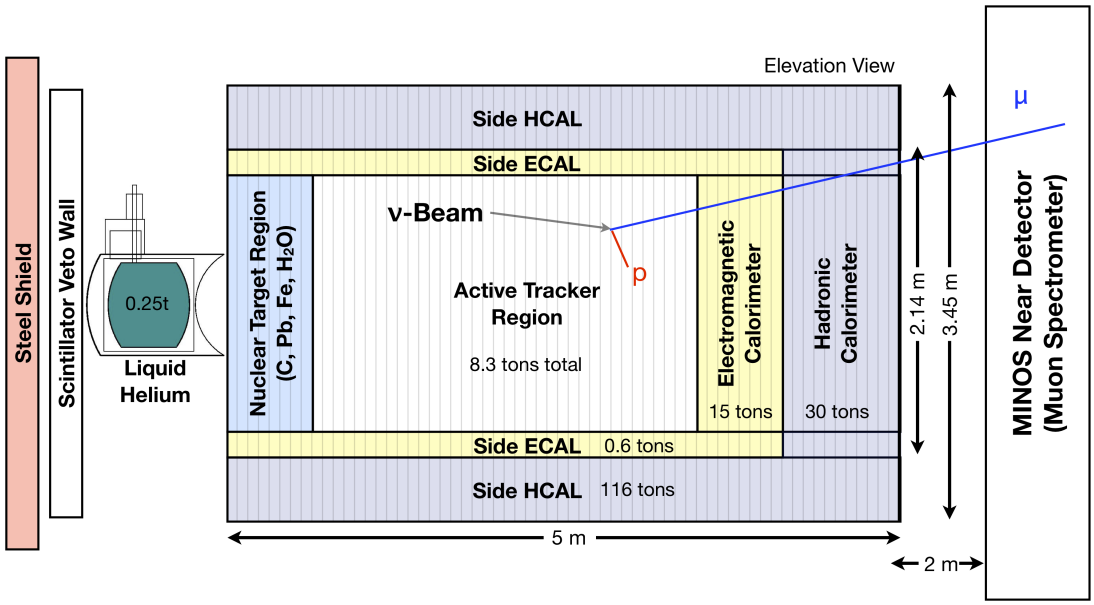

Figure 3.4: Schematic view of the MINERνA detector.

The active target (the core of the detector) consists of strips of solid scintillator. It is the primary volume where interactions happen and where all the analysis is centered. That includes deep inelastic scattering, photon tracking, detection of protons, particle identification through $\frac{dE}{dx}$ (loss of energy by unit of length). Since scintillators, due to their low density, can not hold the whole event, its volume is surrounded by a sampling detector that constitutes the electromagnetic and hadronic calorimeters. In these detectors scintillating strips are interleaved with absorbers (lead sheets in the electromagnetic calorimeter and steel sheets in the hadronic calorimeter). Upstream the detector a veto wall is used to identify charged particles that traverse the detector.

The detector has the shape of a $5.9m$ hexagonal prism of cross section varying from 3.35 m to 4.10 m. The total mass of scintillators is 6.4 ton. Nuclear targets consisting of Fe

(998kg), Pb(1023kg), C(120kg), liquid He (250kg) and H_2O are upstream of the detector[3]. The detector high granularity (see scintillating strip description in section 3.3) assures precise vertex reconstruction. The detector is segmented in scintillating planes (section 3.3) and use the Outer Detector(OD) as a supporting structure.

The Inner Detector(ID) has scintillating planes with strips arranged in three different orientations: X, U and V as shown in figure 3.5. U and V planes are rotated $\pm 60^o$ relative to X. Two scintillating planes XU or XV make a module. This arrangement allows tracking reconstruction. Figure 3.6 illustrates one module of the detector active region (structure of a module is depicted on the right).

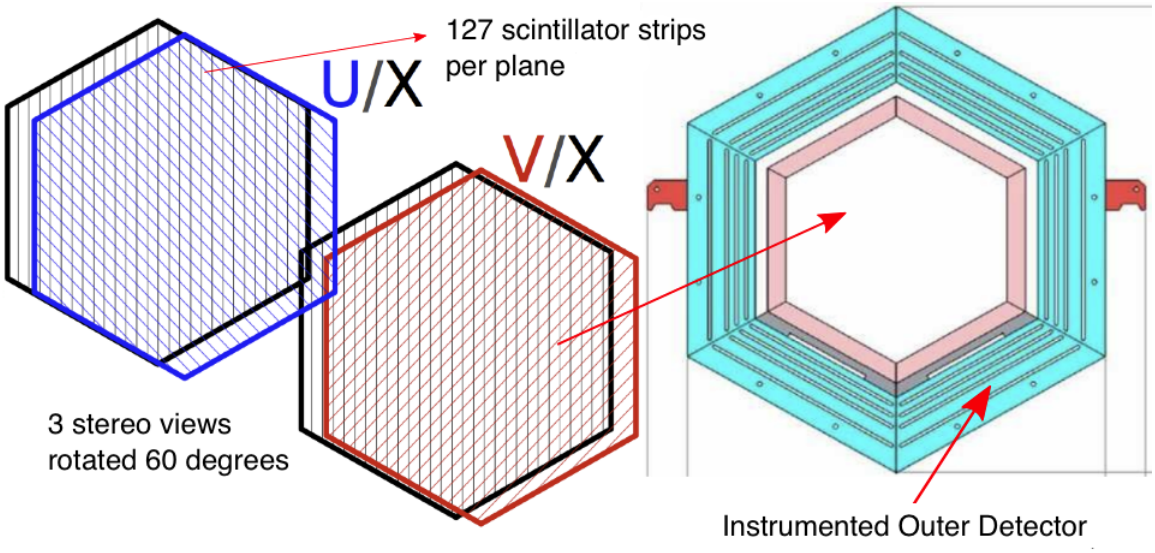

Figure 3.5: Detector active module, featured, X, U and V planes. Note the $\pm$ 60^o rotation of the planes U and V relative to the X planes.

Figure 3.7 shows a module of the electromagnetic calorimeter. Lead sheets are 0.2 cm thick and are placed between scintillating planes.

The Inner Detector(ID) is surrounded by a system of absorbers and scintillators that constitute the Outer Detector(OD) (formed by towers arranged at the sides of the hexagon). The downstream part of the detector has a hadronic calorimeter (HCAL) with 1 inch thick absorbers per scintillating plane as shown in figure 3.8. The electromagnetic calorimeters(ECAL) have 0.2 cm thick Pb sheets as absorbers. The ECAL high granularity assures a good resolution for the energy of electrons and photons and make it possible to determine their direction.

[3]Considering a transversal section with radius = 90cm

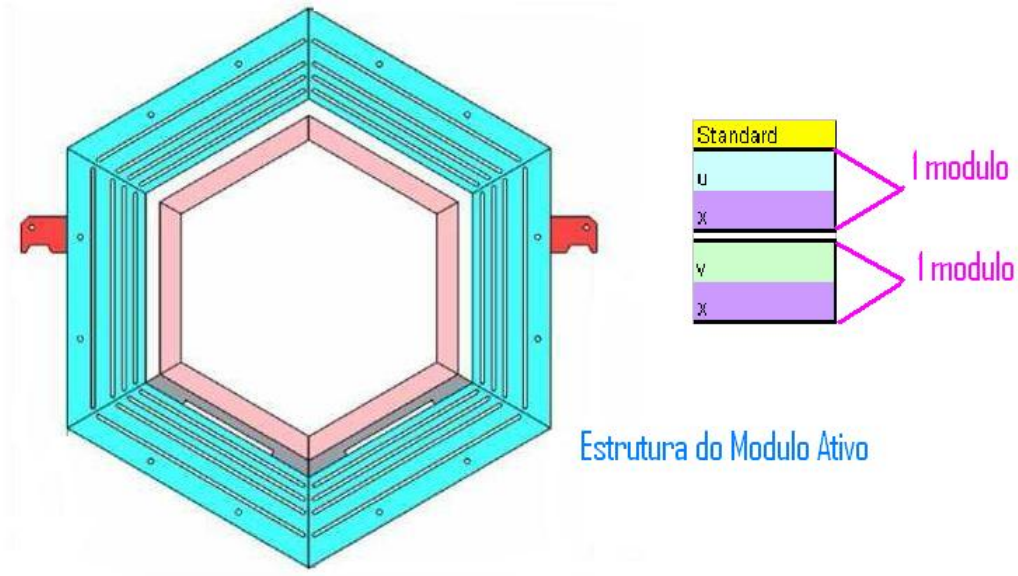

Figure 3.6: Detector ative module. Structure of a module is depicted on the right.

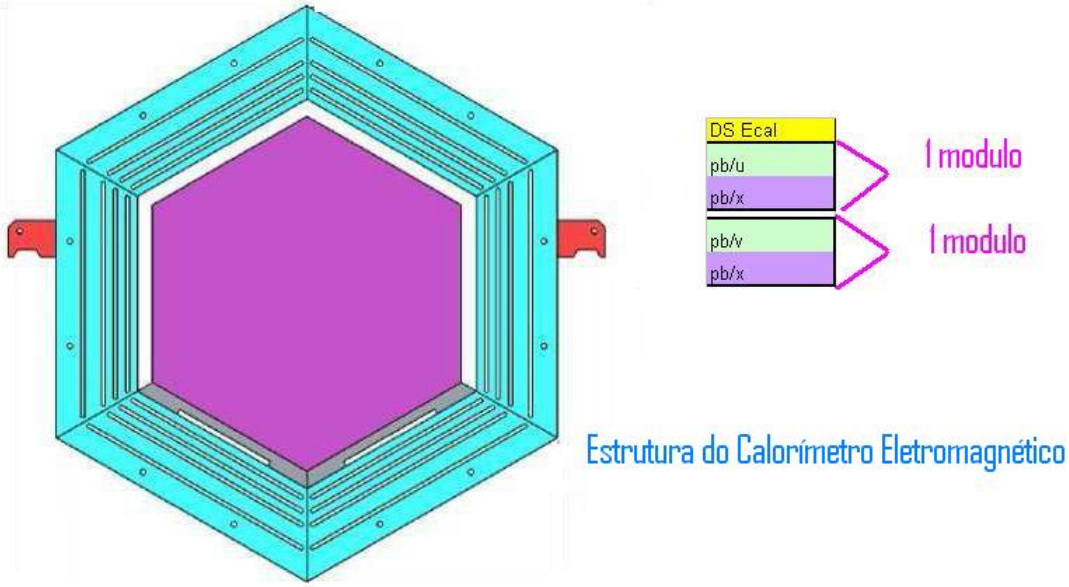

Figure 3.7: Module of the electromagnetic calorimeter. Structure of modules is depicted on the right.

The nuclear target region (figure 3.4) has absorbers placed between active targets making it possible the study of events in different nuclear targets.

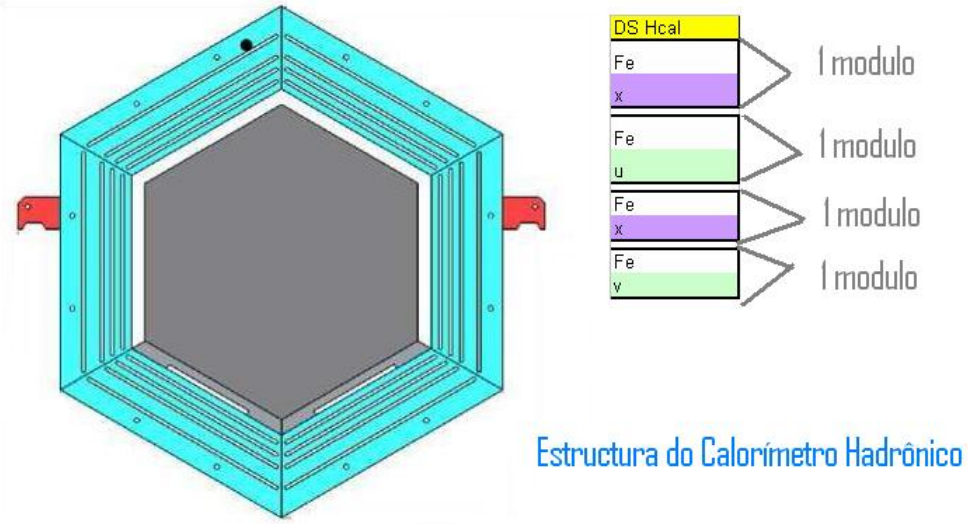

Figure 3.8: Module of the hadronic calorimeter. Structure of the modules with alternating Fe and scintillating planes is depicted on the right.

3.3 The scintillating strips

The active part of the MINERνA detector is built with triangular prisms of solid scintillator (polystyrene, Dow 663) doped with POP (1% per weight) and POPOP (0.03% per weight)) coated by a reflective layer of TiO_2 and traversed by a 1.2 mm WLS optical fiber (Kuraray Y11 doped at 175ppm) as shown in figure 3.9). The WLS fibers go to optical connectors in both ends of the modules from where clear fibers guide the light to multianode photomultipliers.

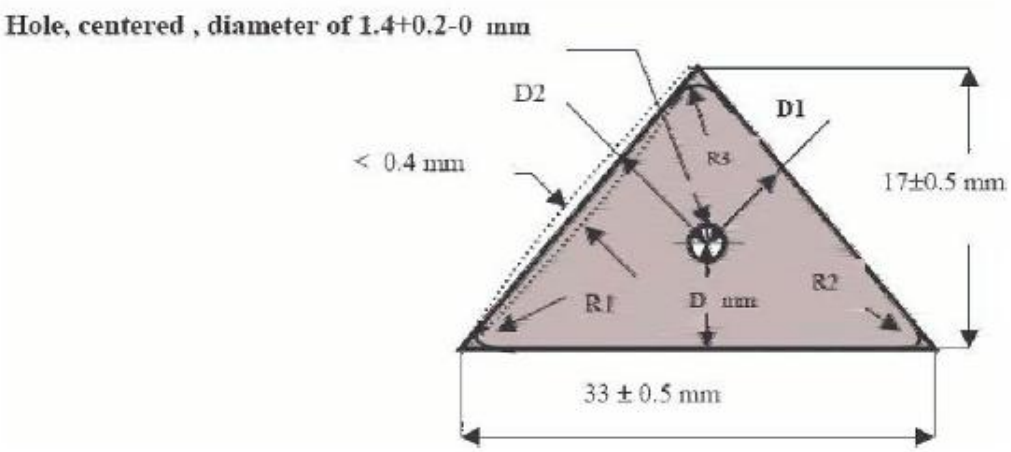

Figure 3.9: Transversal cut of the triangular scintillating prism used in the Inner Detector.

To improve coordinate resolution these triangular elements are assembled in planes (fig-

ure 3.10). Interpolation of the charge split between neighbor scintillating strips allows the determination of the coordinate.

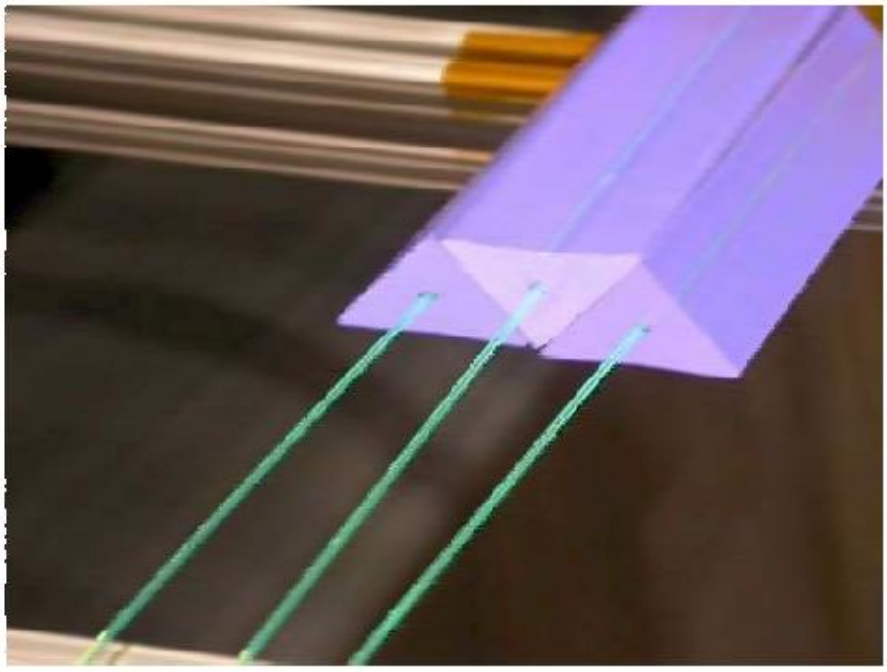

Figure 3.10: Scintillating prisms arranged to form a plane. Each prism holds an optical fiber along its full length.

3.4 Photodevices

The light collected in the scintillators must be converted into electric pulses whose characteristics represent the deposited energy. The light signal is strong enough for photodevices with 15% quantum efficiency. MINERνA detector employs 64 channel multianode photomultiplier R7600U-00-M64 manufactured by Photonics [66]

3.5 Calorimeters

MINERνA measures the energy of charged particles ($p, \pi^{\pm}, K^{\pm}, \mu^{\pm}$) and neutral particles (π^0, K^0, γ) with energies in the order of few GeV by means of two systems of calorimeters: a set of alternated lead and scintillator planes downstream of the active target for electromagnetic calorimetry and a set of alternated steel and scintillator planes downstream of the active target for hadronic calorimetry; a set of lead, steel, carbon and scintillator blocs assembled around the active target for both electromagnetic and hadronic calorimetry.

3.5.1 Electromagnetic calorimeter

High energy photons are detected by means of the production of pairs of charged particles that give rise to a shower of e^+, e^- and γ. Since pair production cross section is proportional to Z^2, lead sheets are commonly used to produce showers of reasonable size. The typical length of the shower varies with the energy; however, for photons of a few GeV, as the ones we expect in our experiment, 99% of the energy will stay in 4 cm of Pb (7 radiation lengths).

The electromagnetic calorimeter downstream of the active target is made of 20 layers of Pb (2 mm thick each) alternated with scintillating planes formed by the triangular scintillating prism of scintillator described in 3.3. The expected energy resolution is $6\%/\sqrt{E}$ where E is given in GeV. The side electromagnetic calorimeter is also made of 2 mm thick layers of Pb alternated with layers of scintillator. Photons penetrating the side electromagnetic calorimeter in an angle up to 25^o relative to the beamline are absorbed. Photons penetrating at higher angles will not be totally absorbed by the electromagnetic side calorimeter and will penetrate the side hadronic calorimeter where the remaining shower will be totally contained.

Since the main objective of the downstream layers of Pb, Fe and C (that are thicker) is to work as a target, the calorimetry is not as efficient in this region as it is in the upstreem modules. The way the targets are positioned presents an interaction length between 5 and 10 to the shower. Since the photons in this direction are of lower energy the showers that initiate in the central region will be totally contained in the detector.

3.5.2 Hadronic calorimeter

The downstream hadronic calorimeter is placed just after the electromagnetic calorimeter and is made of 20 layers of Fe (2.54 cm thick each) alternated with scintillating planes. The combined action of 4 cm of Pb and 50 cm of Fe stops muons with energy up to 600 MeV and protons with energy up to 800 MeV [4]. The side hadronic calorimeter has layers of Fe and scintillator (totaling 43.4 cm of Fe and 12.5 cm of scintillator) that is enough to stop 750 MeV protons penetrating at 90^o and 1 GeV protons penetrating at 30^o.

The expected energy resolution of the hadronic calorimeter is around $50\%\sqrt{E}$ for hadrons with energy above 1 GeV. For less energetic particles the resolution is expected to be 50% or less, depending of the energy.

[4] Since the interaction length for Fe is 16 cm protons and pions of higher energy are likely to be stopped

3.6 Nuclear targets

MINERνA has nuclear targets of Fe, C, Pb, He and H_2O (table 3.1). Iron is a cheap and common absorber used in neutrino experiments. Lead is the material with higher Z that is easy to obtain. Ideally the nuclear targets should consist of many thin targets interleaved with tracking layers so as to allow the determination of the multiplicity of final states and the energy of each low energy particle. However, several factors limit the size and number of targets and tracking layers. The intrinsic detector spatial resolution is of the order of 1 cm in the z direction (the beam direction) making thiner targets ineffective. Sheets thicker than 2.5 cm (like MINO's) would not significantly improve our knowledge of low energy particles spectrum that is one of MINERνA's objective and, to improve statistics, we would have to use about 1 ton of each target.

Target material	Mass (ton)	Charged current sample (K)
Helium	0.25	14
Carbon	0.12	9.0
Iron	0.99	54
Lead	1.02	57
water	0.39	20

Table 3.1: Charged current events expected at each nuclear target.

MINERνA target was implemented according to the following scheme where each F represents a XU or XV structure (a FF pair is a set XUXV): FF Pb/Fe [target 1] FFFF Pb/Fe [target 2] FFFF Pb/Fe/C [target 3] FFFF Pb[target 4] FFFF Pb/Fe [target 5]. Targets 1 and 2 have 60% Fe and 40% Pb totaling 230 kg of Fe and Pb in each target. Target 3 has 50% C, 30% Fe and 20% Pb totaling 140 kg of C, 110 kg of Fe and 110 Kg of Pb. Target 4 is pure Pb with a total mass of 170 kg. Target 5 has 60% Fe and 40% Pb each with 115 kg. The total mass of Fe and Pb is, respectively, 685 kg and 855 kg. Total expected number of CC events is 2 millions for Fe, 2.5 millions for Pb and 400,000 for C. Figure 3.11 shows the target configuration, including the water target. It is a hexagonal shaped box (with the same dimensions as the detector) placed immediately before the other targets. The He target will be installed immediately upstream of the detector as illustrated in figure 3.4

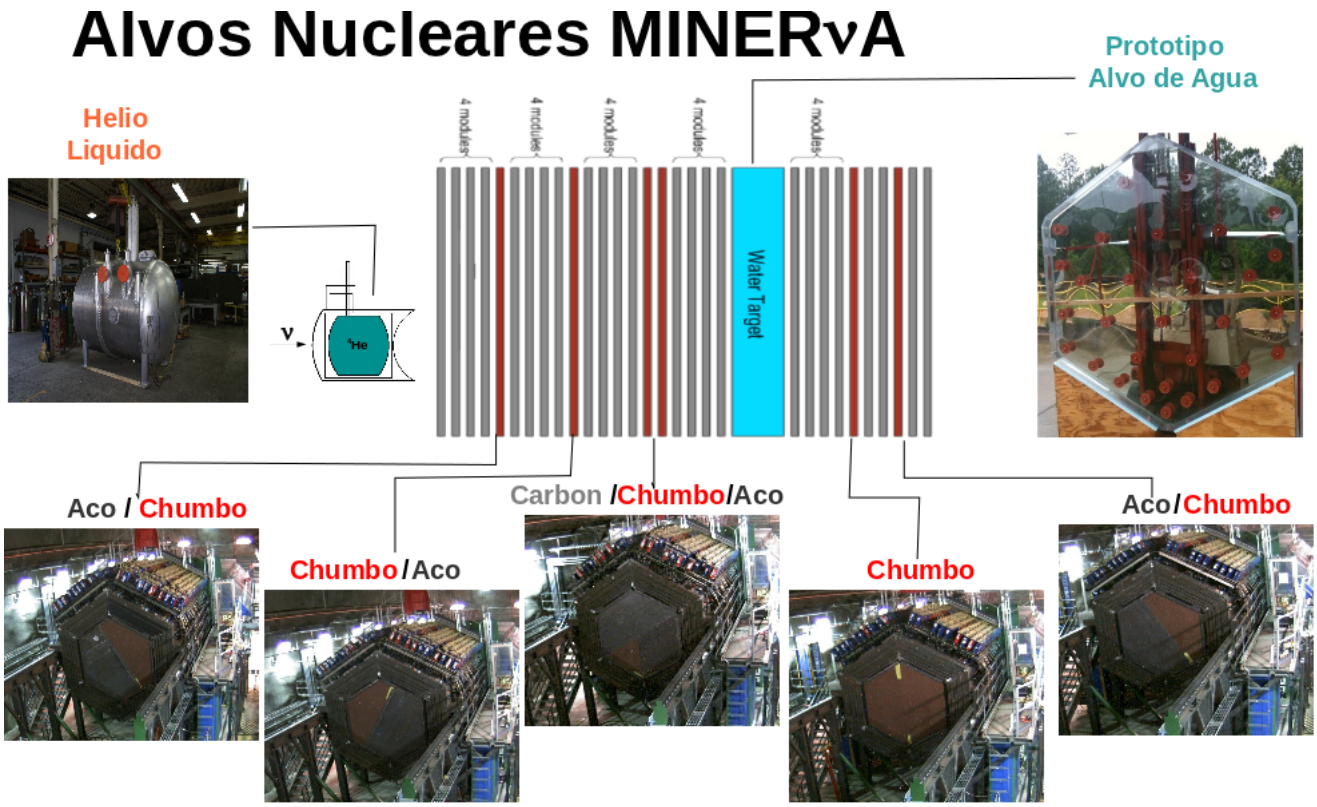

Figure 3.11: MINERνA Nuclear targets

3.7 Electronic and data acquisition (DAQ)

Table 3.2 summarizes the requirements of the electronics of the MINERνA detector. The requirements are motivated by the following objectives:

- Fine spacial resolution taking advantage of the light sharing between adjacent scintillating bars;
- $\pi^{\pm}$ and p identification by dE/dx;
- Efficient pattern recognition using timing to identify the direction of the trajectory and to identify interactions that occur during the same spill;
- Ability to identify strange particles and muon decays through coincidence techniques;
- Negligible dead time in each spill.

MINERνA DAQ requirements are modest due to the relatively low event rate (about 100 kBytes/s).

Parameter	value
spill	12 μs
Repetition time	>1.9 s
Number of channels	30,972
Occupation per spill	2%
gain variation of the photodevice	4.5 dB
Time resolution	3 ns

Table 3.2: Some parameters and requirements for the electronics at MINERνA .

3.7.1 DAQ hardware

MINERνA active elements have their signals sent to 64 multianode photomultipliers (MAPMT). Information about amplitude and time is digitalized by the electronics and stored for readout by the data acquisition system (DAQ). Each readout electronic front-end board (FEB) is connected to one single fotomultiplier.

Groups of up to 10 FEB are read and the result sent to a crate read-out controller (CROC) housed in a VME crate. Each CROC can accommodate 4 chains of FEB readout. A total of 12 CROCs is needed for the whole MINERνA detector. The VME crates also house a CROC interface module (CRIM), a MINERνA timing module (MTM) and a 48 V power supply. There are no CPU in the VME crates. The DAQ works during the whole spill. After a period of 12 μs the DAQ reads all channels that have a signal above a predefined threshold. Even with a high occupancy rate the total number of bytes that are read in each spill is below 200 kB with zero suppression (1 MB without zero suppression). Dead time is negligible.

The photomultipliers are powered by 48 V power supplies. MINERνA uses the same hardware for data acquisition and for the detector control system (DCS). A single connection is used for the FEB readout and as communication channel for the control of the detector (as, for instance, the control of the MAPMT voltages). The main computers for the DAQ and for the slow control system (the system that controls and monitors the slow varying variables) are close to the VME electronics and are connected to FERMILAB network by two high speed TCP/IP lines. A two CPU server controls the whole system: one CPU dedicated to data acquisition and the other dedicated to control and monitoring. All DAQ machines run on Scientific Linux.

3.7.2 DAQ software

MINERνA software runs in the GAUDI framework originally developed for the LHCb collaboration. The expected average of data without data suppression is only 100 kB/s and a two seconds window is available for each 10 μs spill. The highly predicable beam time makes a complex trigger system unnecessary. Instead of such a complex system we simply have a gate signal that opens immediately before the arrival of the beam and all charge and time information from the whole detector is registered just after the end of the spill. The slow control system is also simple with each MAPMT having its own local power supply and with the FEB being in charge of reading the high voltages, temperatures and other parameters used for monitoring and control. A schematic diagram of the DAQ is shown in figure 3.12.

3.8 Perspectives for the MINERνA Experiment

Between 1 and 10 GeV all relevant neutrino data comes from bubble chamber experiments that run between 1960 and 1980. Gargamelle 12 feet bubble chamber, Brookhaven 7 feet chamber, CERN BEBC, Serpukov's SKAT and FERMILAB 15 feet chamber studied neutrino and antineutrino interactions with nuclei.

Despite low statistics the excellent image resolution of bubble chambers made many experiments possible. However, bubble chamber data do not cover the whole neutrino energy spectrum, all nuclear target and all kinds of neutrinos necessary for a complete understanding of neutrino interactions. Table 3.3 summarizes the current experimental status of those projects.

The complete MINERνA detector started taking data in march 2010 and should continue until 2014. In this period the experiment is expected to collect 14.5 M charged current events (CC). Table 3.4 presents the expected number of events in different processes.

MINERνA run at NuMi LE configuration until june 2012 along with the MINOS experiment and will run at ME configuration along with the NOνA after the 2012 shutdown. A small percentage of the NuMI flux is estimated to consist of ν_e. One important goal of the MINERνA experiment is to measure ν_e flux and energy spectrum more accurately than the ones that can be obtained by MINOS.

MINERνA also makes more precise low energy cross section measurements possible. For total cross section we must consider the contributions, $\sigma_{TOT} = \sigma_{QE} + \sigma_{RES} + \sigma_{DIS}$ where

σ_{QE}: quasielastic :$\nu(\overline{\nu})n(p) \rightarrow \mu^-(\mu^+)p(n)$

Experiment	Year	Reaction	Measurement	Events	Reference
Gargamelle	1977	$\nu/\overline{\nu}$-propane/freon	semi-inclusive	ν:1,061	[67]
	1977	$\nu/\overline{\nu}$-propane/freon	π production	$\overline{\nu}$:1,200	
Gargamelle	1978	$\overline{\nu}$-propane/freon	$\overline{\nu}(\pi^0)$	139	[68]
	1978	$\overline{\nu}$-propane/freon	$\overline{\nu}(\pi^-)$	73	
Gargamelle	1978	ν-propane/freon	$\nu p \to \nu p \pi^0$	240	[69]
	1978	ν-propane/freon	$\nu p \to \nu p \pi^+$	104	
	1978	ν-propane/freon	$\nu p \to \nu n \pi^0$	31	
	1978	ν-propane/freon	$\nu p \to \nu n \pi^+$	94	
Gargamelle	1979	$\nu/\overline{\nu}$-propane/freon	$\nu(1\pi^0)$	178	[70]
	1979	$\nu/\overline{\nu}$-propane/freon	$\overline{\nu}(1\pi^0)$	139	
BNL-Counter	1977	$\nu/\overline{\nu}$-Al/C	$\nu(\pi^0)$	204	[71]
	1977	$\nu/\overline{\nu}$-Al/C	$\overline{\nu}(\pi^0)$	22	
ANL-12	1974	ν-D_2/ν-H_2	$\nu p \to \nu n \pi^+$	8	[72]
	1974	ν-D_2/ν-H_2	$\nu p \to \nu p \pi^0$	18	
ANL-12	1980	ν-D_2	$\nu n \to \nu p \pi^-$	?	[73]
ANL-12	1981	ν-D_2	$\nu n \to \nu p \pi^-$	?	[74]
	1981	ν-D_2	$\nu p \to \nu p \pi^0$	8	
	1981	ν-D_2	$\nu p \to \nu p \pi^+$	22	
BNL-7	1981	ν-D_2	$\nu n \to \nu p \pi^-$	200	[75]

Table 3.3: Current neutral current measurements.

Process	Total	CC/t	NC/t
Quasielastic	0.8 M	0.27 M	0.09 M
Resonant production	1.7 M	0.53 M	0.16 M
Transition: Resonant to DIS	2.1 M	0.67 M	0.21 M
DIS, Structure functions and PDF at high x	4.3 M	1.37 M	0.4 M
Coherent production of π	0.13 M	0.09 M	0.04 M
Production of charmed and strange barions	>240 k		
Generalized parton distribution	around 10 k events		
Nuclear effects	He: 0.6 M, C: 0.4 M, Fe: 2.0 M e Pb: 2.5 M		

Table 3.4: Estimated number of events for different processes.

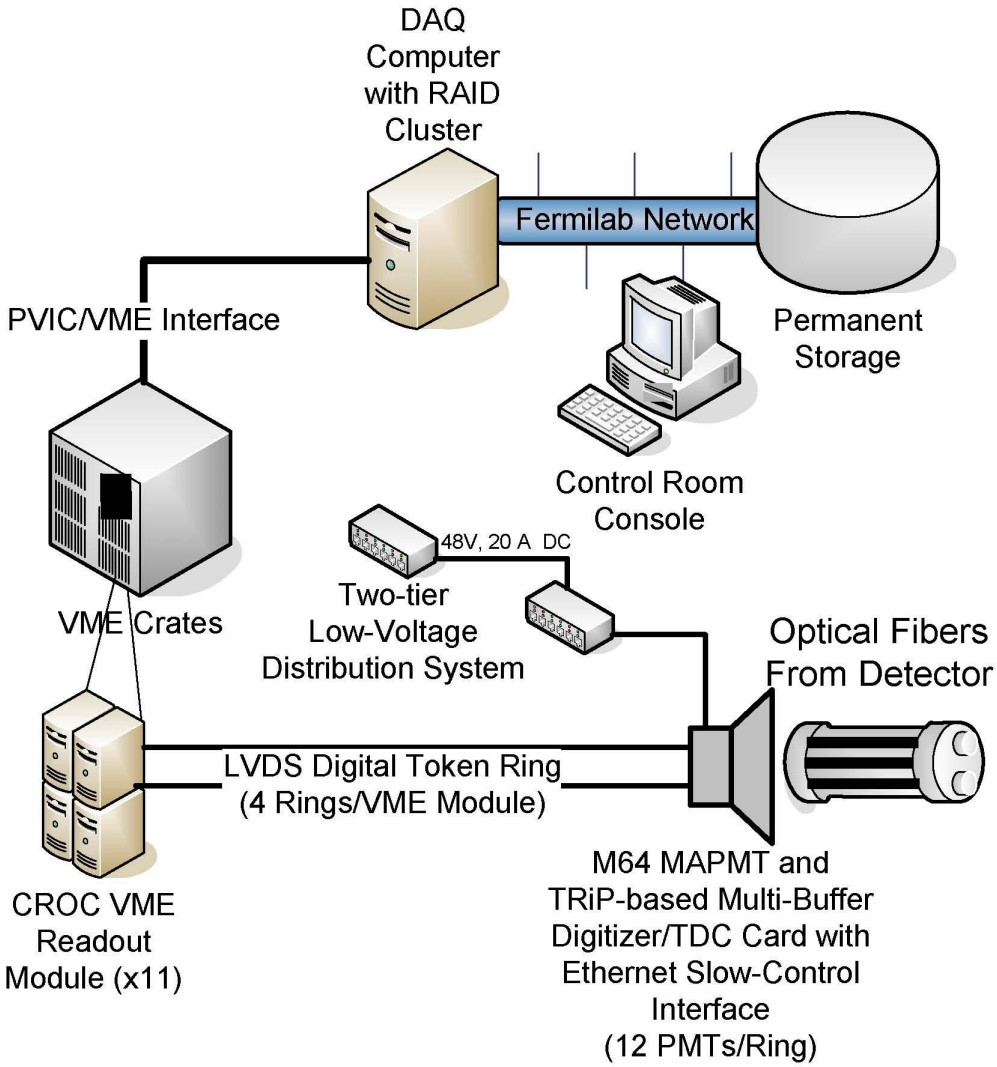

Figure 3.12: Schematic diagram of MINERνA data acquisition system.

σ_{RES}: resonant : $\nu N \rightarrow \mu N^*$

σ_{DIS}: deep inelastic scattering :$\nu N \rightarrow \mu X$

Quasielastic events provide an opportunity for a high precision measurement of $\sigma(E_\nu)$ and $d\sigma/dQ^2$ that are important for the study of neutrino oscillation, the determination of axial vector form factor F_A (particularly at high Q^2), the study of the intranuclear proton scattering and the dependence to the mass number A (targets C, Fe and Pb).

The detector high granularity and tracking capability allow the identification of events with different topologies. Figure 3.13 illustrates how three different topologies show in the detector.

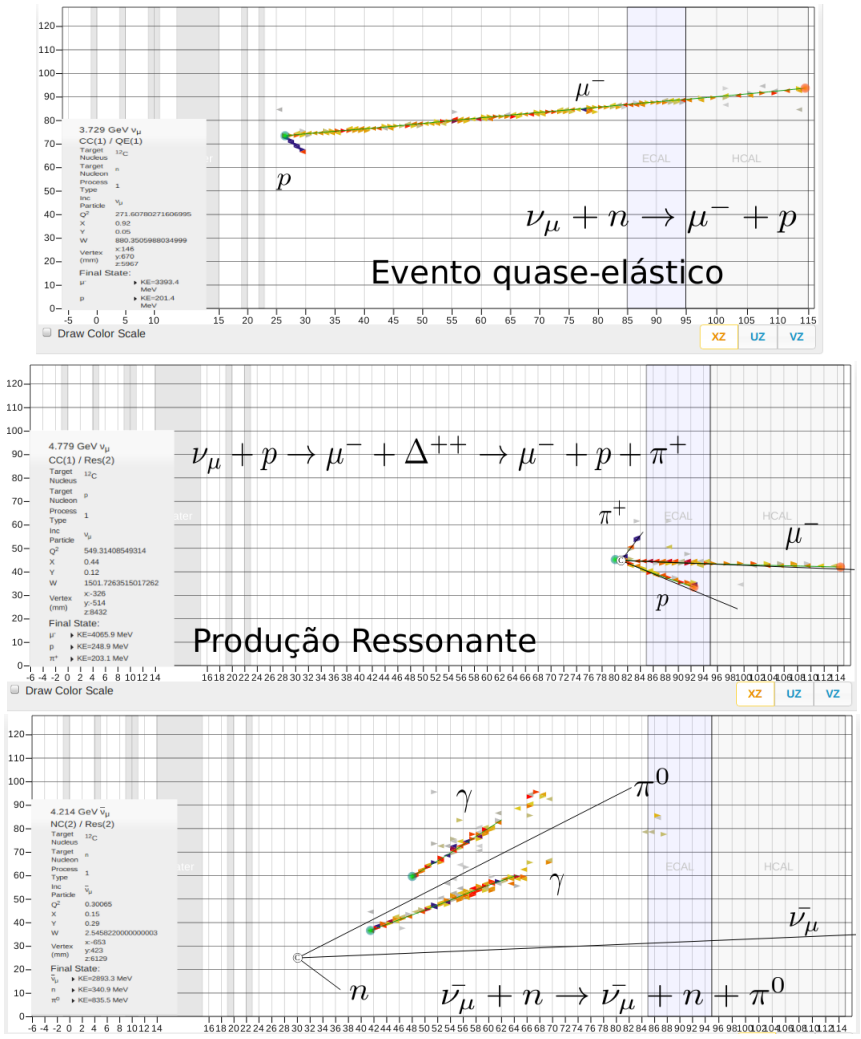

Figure 3.13: Simulation results showing how MINERνA can differentiate several event topologies.

A neutrino scattering experiment at the NuMI beamline is an invaluable opportunity for a high precision study of several topics. Some of these topics have either not been systematically studied or have few results with big statistical and systematical errors. Some subjects that can be studied by the MINERνA experiment are:

- Measurement of the quasi-elastic neutrino-nucleon cross section and its dependence on E_ν and Q^2;
- Measurement of π production cross section in charged current and neutral current interactions;

- Precise measureament of the coherent π production and its dependence on A;
- Study of nuclear effects in neutrino interactions;

These items are important subjects by themselves. Moreover, they are essential for the minimization of systematic errors in oscillation experiments.

Figure 3.14 shows current cross sections measurements and the energy range of several experiments. Note the broad region covered by MINERνA.

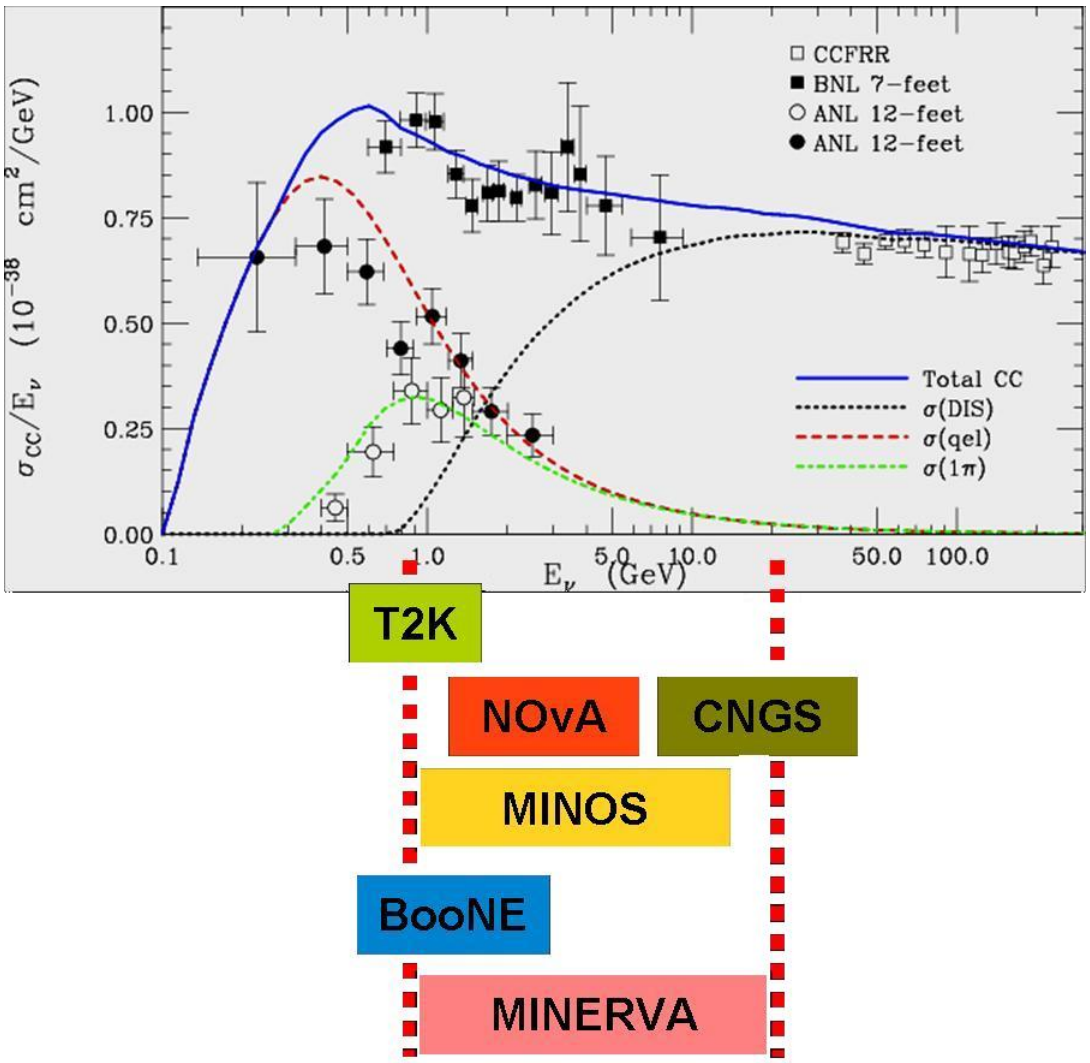

Figure 3.14: Current cross section neasuremnents for several processes. The energy range covered by several current and future experiments is shown.

Data shown in figure 3.14 belong to experiments from last century 70s and 80s and have low statistics and high systematic errors. MINERνA will reduce the uncertainties as shown in table 3.5.

Estimated cross section uncertainty		
Process	Current	After MINERνA
Quasielastic	20 %	5 %
Resonant production	40 %	5/10 % (CC/CN)
DIS	20 %	5 %
Coherent production of π	100 %	20 %

Table 3.5: Cross section uncertainty: current and expected after MINERνA.

3.8.1 Quasi-elastic scattering

Quasi-elastic scattering is the dominant process in interactions ν-A in the $E_\nu < 2$ GeV region. Precise measurement of this process cross section and its dependence to the energy and to A is of fundamental importance for neutrino oscillation experiments.

Plot at top of figure 3.15 summarizes the current knowledge of the quasielastic cross section. The plot at the bottom shows the expected measurements from MINERνA.

3.8.2 Resonant pion production

High statistics, multiplicity of nuclear targets, low detection threshold and excellent calorimetry and tracking system allow MINERνA to make significant improvements in the measurements of resonant pion production in neutrino interactions. These measurements will set limits to the absolute and relative cross sections, to the shape of the Q^2 distribution and will allow the first direct comparison of neutrino interactions in different targets.

3.8.3 Pion Coherent Production

MINERνA high rates, multiple nuclear targets, high granularity, high track reconstruction capability and good calorimetry make it possible the study of neutrino-nucleus coherent scattering in both charged and neutral current processes with a precision that has not yet been achieved.

Figure 3.16 shows current results for pion coherent production together with the results expected from MINERνA.

3.8.4 Coherent Cross Section Dependence on A

MINERνA will compare coherent production cross section for C and Pb. The A dependence of the cross section is very dependent of the model used for the calculation, specially the model for hadron-nucleus interactions. Measuring the A dependence provides a test of the models.

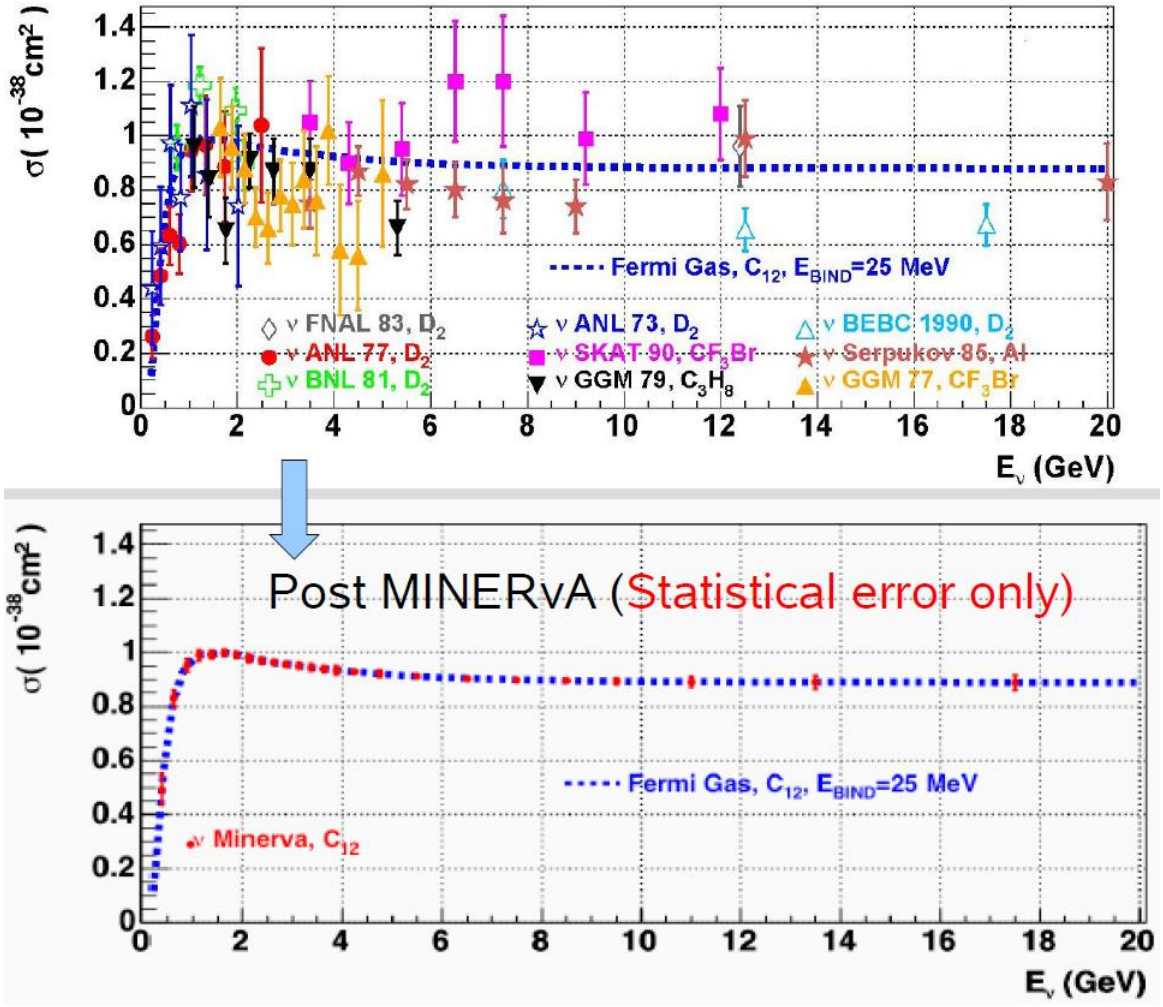

Figure 3.15: Top: current measurements of the quasielastic cross section. The blue dotted line uses a Fermi gas model. Bottom: results expected from MINERνA (statistical errors only) .

The Rein-Seghal and the Paschos model, for instance, respectively predict 0.223 and 0.259 as the ratio between the NC production cross section for ν-C and ν-Pb. Figure 3.17 shows the A dependence as predicted by both models. The MINERνA experiment can provide a check of the models.

3.8.5 Deep Inelastic Scattering (DIS)

The study of deep inelastic scattering plays an important role in the understanding of the parton distribution functions (PDF). PDF describe how partons are distributed in protons and other hadrons and are defined in terms of matrix element operators . Using neutrinos for DIS studies is important because only neutrinos can resolve the flavors of the nucleus constituents. MINERνA can use neutrinos to measure the parton structure with a high statistics. MINERνA

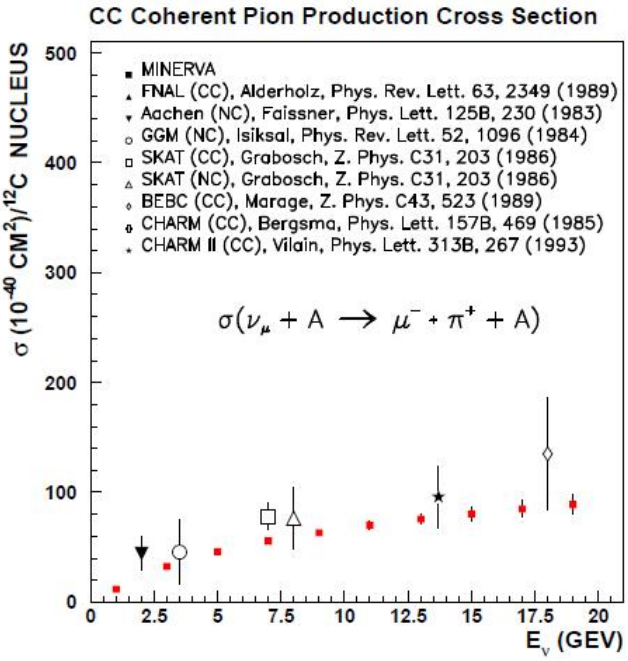

Figure 3.16: Current and expected results from MINERνA for pion coherent production.

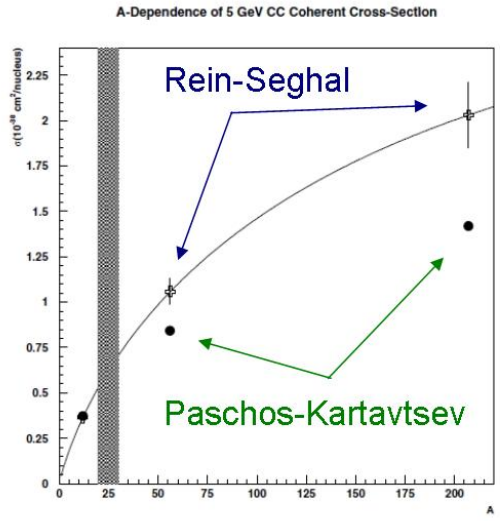

Figure 3.17: Cross section as a function of A. The shaded area shows the region of previous measurements. Crosses are the Rein-Sehgal prediction for ν scattering by C, Fe and Pb and the circles are the Paschos-Kartavtsev predictions. The MINERνA experiment can provide a check of the models.

has the capability to do the first independent calculation of the structure functions $F_1^{\nu N}(x,Q^2)$, $F_1^{\bar{\nu} N}(x,Q^2)$, $F_2^{\bar{\nu} N}(x,Q^2)$, $F_2^{\nu N}(x,Q^2)$,$xF_3^{\nu N}(x,Q^2)$, and $xF_3^{\bar{\nu} N}(x,Q^2)$. Parton distributions can be calculated through the sums and differences of these structure functions. The MINERνA

experiment can use the structure functions of ν and $\bar{\nu}$ to improve the measurement of these PDFs.

MINERνA multiple targets make it possible the measurement of cross section and structure functions for several nuclear targets. This is important to establish a connection between previous measurements and MINERνA measurements at high Q^2 and allow the first measurement of nuclear effects in neutrino scattering.

3.9 Event Reconstruction

Before getting any physical information one must reconstruct the physical events with the characteristics of the particles that go through the detector. Reconstruction starts with objects like hits, clusters, blobs and tracks. We use a coordinate system showed in the figure 3.18, X-Y axis are defined over the MINERνA plane, Z axis is perpendicular to this plane. The neutrino beam points down at 3.3 degrees with respect to Z axis.

Due to the detector geometry all information comes in the form of hits (or Digits in the MINERνA framework). The hits (signals left in each part of the detector) can either be in the Inner Detector(ID) or in the Outer Detector(OD) and carry information about time, position (in two dimensions) and the energy deposited in the scintillating bars.

A clusters is a set of hits that meet some requirements (like being close to each other). To form a cluster hits are first ordered by plane, module and strip. In the second step adjacent hits are grouped forming the cluster. A track is made from a sequence of clusters and can be short or long depending on how much the particle travels in the detector.

A blob is a three-dimensional object consisting of a collection of clusters. This collection of clusters represents the deposited energy. Figure 3.19 shows the main objects employed in the reconstruction of a MINERνA event. Groups of clusters that do not belong to a track can be part of an electronic or hadronic shower. We use the MINOS Near Detector like our muon spectrometer, Figure 3.20 shows the reconstructed track left by a muon that is viewed at the MINOS detector.

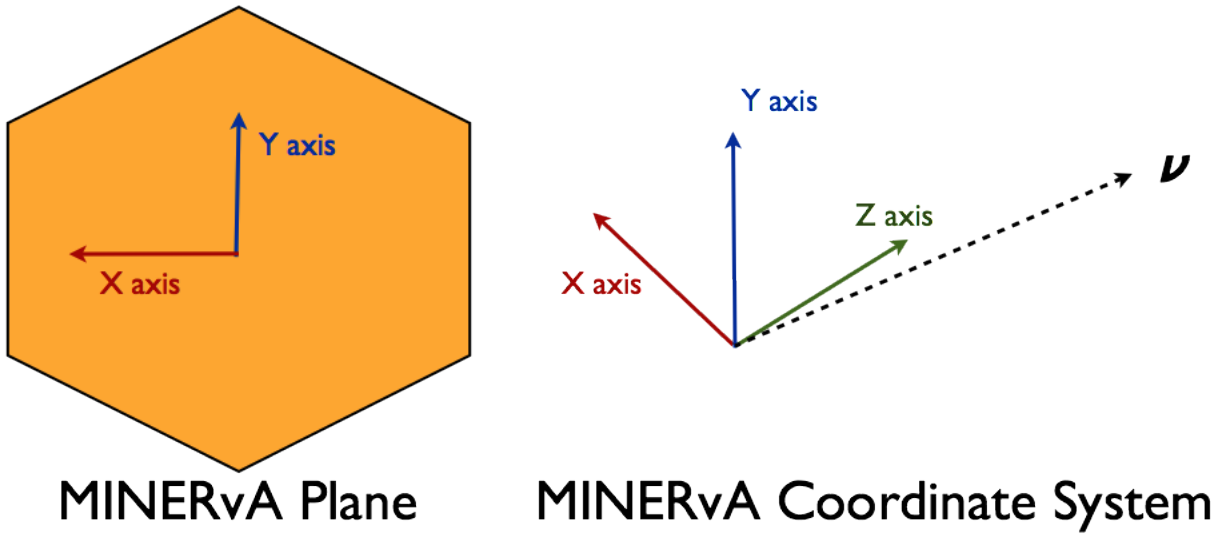

Figure 3.18: MINERνA coordinate system, X-Y plane are defined by MINERνA plane, Z is perpendicular to this plane.

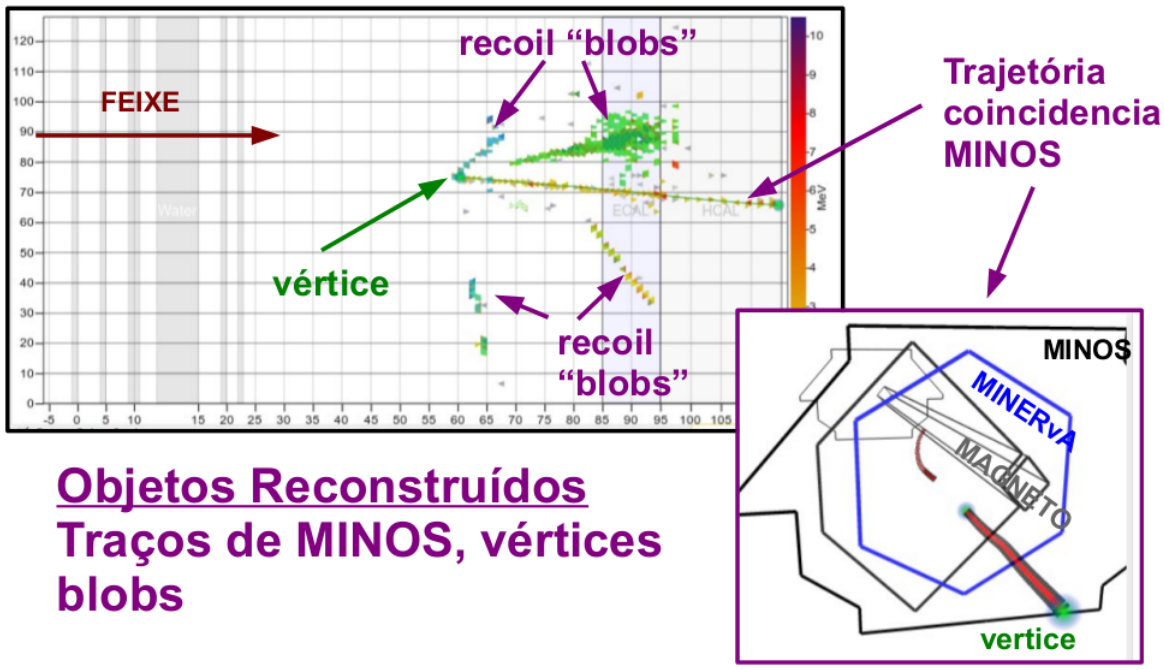

Figure 3.19: Objects reconstructed at MINERνA and MINOS. Small triangles represent hits. The track is the line and blobs are the green or blue objects .

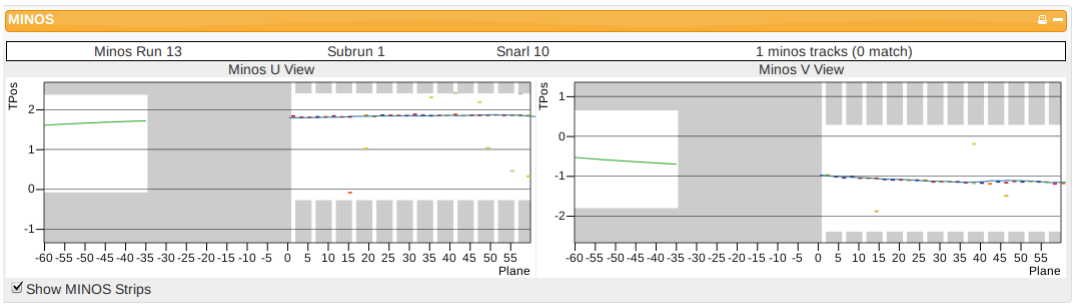

Figure 3.20: Muon track in the MINOS detector.

Chapter 4

Neutral Pion Reconstruction

This chapter describes the reconstruction of π^0. We have developed two methods for π^0 reconstruction that require the reconstruction of the electromagnetic showers produced by the photons resulting from the decay of the π^0. The interaction vertex is determined by the reconstruction of the muon associated with the interacting $\overline{\nu}_\mu$. All clusters that are not included in a track by the MINERνA track reconstruction algorithm are input to our shower reconstruction algorithms.

Energy range of neutral pions on CCπ^0 sample averages 400 MeV . Therefore, our electromagnetic showers resulting from the π^0 decay photons are below 400 MeV. Shower reconstruction is based in grouping adjacent clusters. In the low level of energy of π^0 the electromagnetic showers contain gaps and, in many cases, two showers are too close to each other making reconstruction and discrimination difficult.

4.1 The π^0 meson

Pions are the lightest mesons[1] and play an important role in understanding the low-energy properties of the strong nuclear force. A π^0 decays mostly of the time ($98.82 \pm 0.034\%$) in two photons($\pi^0 \rightarrow \gamma + \gamma$) that we must reconstruct in order to reconstruct the π^0 . These photons produce electromagnetic showers through pair production mechanism ($\gamma \rightarrow e^+ + e^-$). The second most common decay mode, with probability of $1.19 \pm 0.034\%$, is the Dalitz decay into a photon and an electron positron pair ($\pi^0 \rightarrow e^+ + e^- + \gamma$).

In particle physics, decay means that a particular particle disappears and is replaced by two or more so-called decay products. We call the initial particle a mother particle and the decay

[1] hadronic subatomic particles composed of one quark and one antiquark

products the daughter particles. The daughter particles can in turn decay into granddaughter particles and so on until a final stable product is reached. In our analogy the π^0 is the mother and the two decay photons are the daughters

4.2 Angle Scan

This method was developed with the idea of using the decay topology itself to distinguish two different electromagnetic showers. The main idea behind the method is grouping clusters that fall within a conical region starting at the event vertex. These groups of clusters are stored as blobs.

This reconstruction takes the event topology into account and assumes that every cluster (group of hits) has a direction, defined by the straight line connecting the cluster to the vertex. Each cluster is associated to the angle between the cluster direction and the z axis as illustrated in figure 4.1. We fill a 1D histogram where every entry is the angle associate to the cluster weighted by the number of photoelectrons associated to the cluster (a measurement of the cluster energy). The histogram is a kind of map of the event topology that we want to reconstruct.

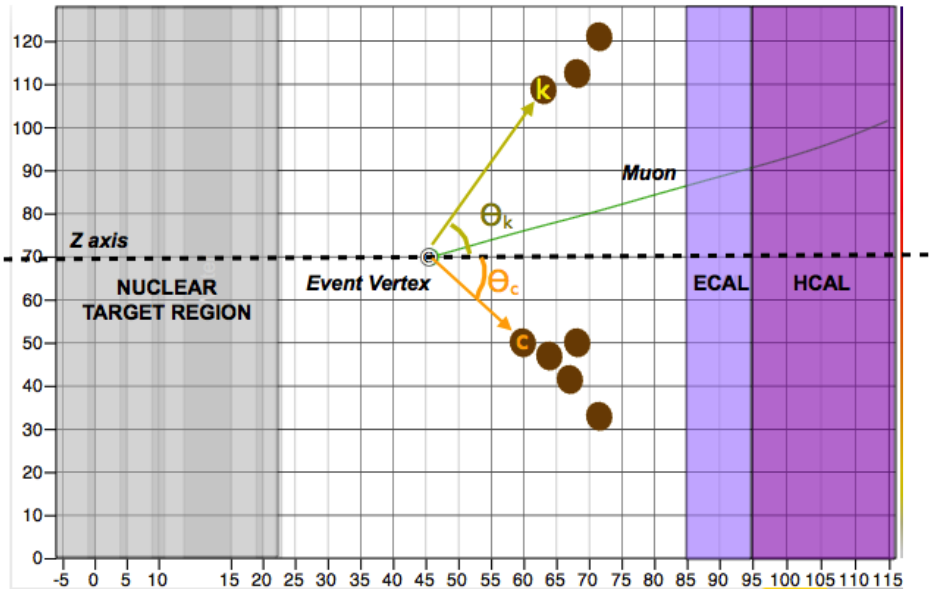

Figure 4.1: The angle (θ_i)between the cluster direction and the z axis is associated to the cluster "i". Our plot shows the angle for two clusters with indexes "k" and "c".

The histogram is scanned bin by bin in search of isolated and continuous distributions representing electromagnetic showers. Figure 4.2 illustrate the process. Two isolated distributions

(Group 1 and Group 2), each defined by two bins, correspond to the two clusters shown in the event display.

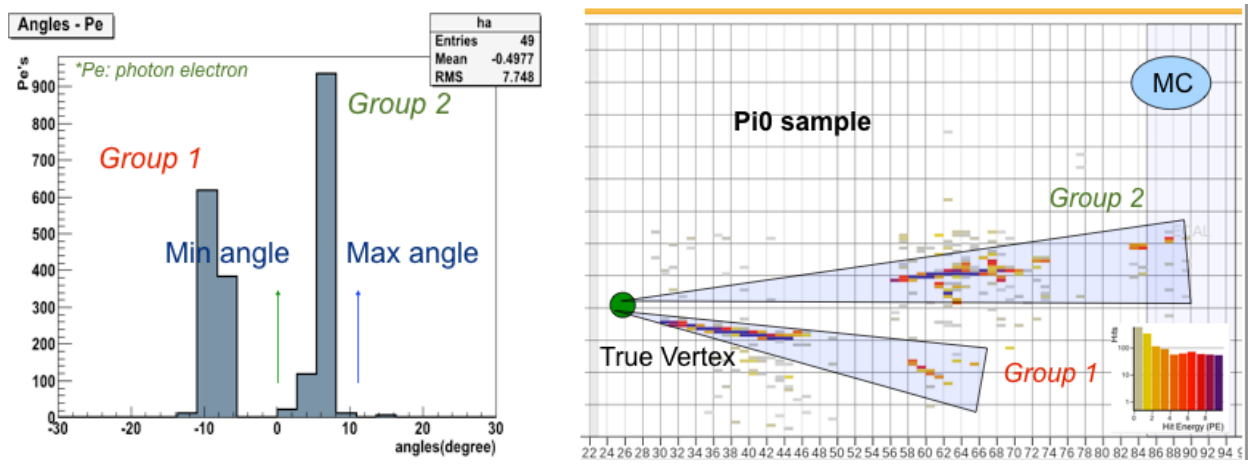

Figure 4.2: Left: Histogram mapping the event display. X-axis represents the angle of the clusters relative to the true vertex. Y-axis represents Photo-electron deposition of the cluster. Right: π^0 event display showing the true vertex where the conical regions containing the electromagnetic showers start.

After identifying groups and their bin limits (minimum and maximum angles) all clusters that fall inside of a conical region defined by the minimum and maximum angle are grouped. In the sample of figure 4.2 group 1 (bottom shower) and group 2 (top shower) are reconstructed with all the clusters inside the conical regions. Note that the conical shape allows the inclusion of all clusters in the main direction regardless of gaps in the showers (as we see in group 1)[2]

The MINERνA detector contains 3 stereo views (X-U-V), any single particle passing trough the detector, leaves clusters in each view. In the absence of other particles those clusters obey the MINERνA geometry condition $X = U + V$. This condition is important when we follow the inverse process; several clusters from severals particles, can be associated to their primary particle using this condition. Our reconstruction starts in the X view, where electromagnetic showers (blobs) are selected. Then we add information from the U and V views clusters to have a complete information about the blob.

To include clusters from the U and V views we re-organize triplets clusters (X-U-V), where the X clusters come from the blob cores created in the first step. For a given triple cluster be

[2]The gaps in the showers are not due to any detector inefficiency but result from low energy electrons and positrons that are slow to interact.

part of a blob, they must be related by X = U + V, but our detector resolution and cluster position errors don't allow perfect match, so, we need to find a minimum value of δ (Eq. 4.1).

$$\delta = X_{TPos} - U_{TPos} - V_{TPos}, \tag{4.1}$$

where X_{TPos} represents the transversal position of the cluster in the X view (Perpendicular position respect to beam direction).

For a given X cluster (from the core blob) and U-V clusters several δ's are calculate. The smallest δ defines the "3 views point" in the detector where the shower particle interacts leaving a 3D position marked. Finally we include clusters around the main direction, drawing 2D cones in the same line defined by the main clusters, per view, because not all clusters are located in the center of the electromagnetic showers.

The Angle Scan method has been developed for the reconstruction of gammas with profile well defined and above $50MeV$. Angle Scan is able to include clusters that happen beyond the showers' gaps as seen in figure 4.3. The left plot shows showers from two gammas. Angle Scan was able to reconstruct both showers despite their difference in size. The right plot shows showers with gaps. Angle Scan reconstructed both completely. Other methods would probably reconstruct just the first part of the shower missing the part after the gap. That leads to an incomplete description of the shower and consequently, to a wrong calculation of the π^0 mass.

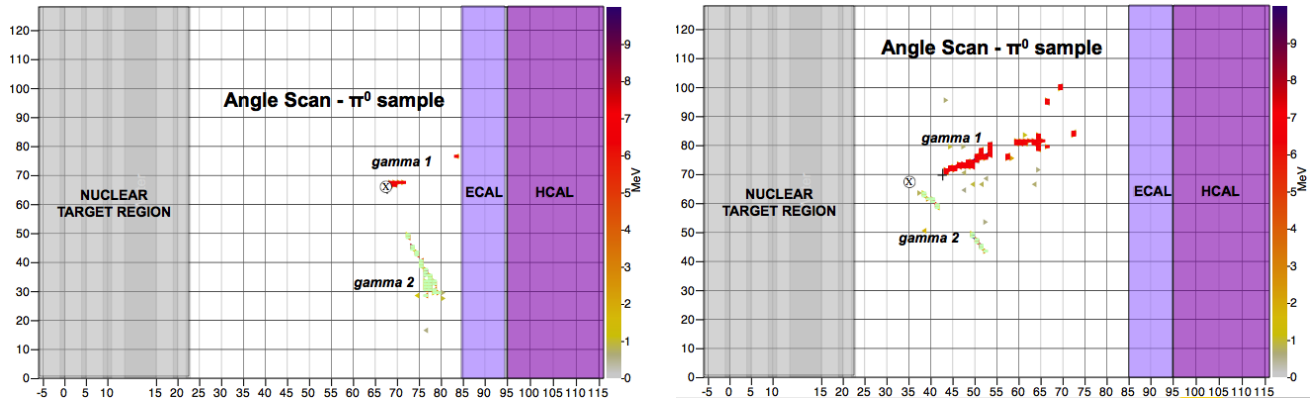

Figure 4.3: Left: Angle Scan applied to a sample where one of the showers is much smaller than the other. Rigth: Angle Scan applied to showers with gaps.

4.3 Hough Transform

In 1962 Paul Hough proposed a technique for recognition of complex patterns[76] that came to be know as Hough Transform. We have used Hough Transform to implement an algorithm to reconstruct lines [77] in an electromagnetic shower that is then used for the π^0 reconstruction. These lines represent the main direction of the shower[3]. When a straigth line is parametrized as shown in Fig.4.4 the following equation applies

$$\rho = xcos\theta + ysin\theta \tag{4.2}$$

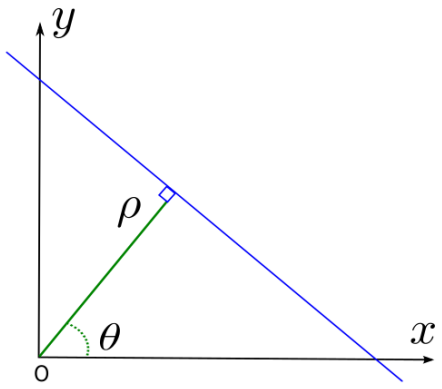

Figure 4.4: The line we want to reconstruct is shown in blue. This line is uniquely defined by ρ and θ.

Each straight line in the X-Y space corresponds to a single point in the Hough space (θ-ρ). If we fix coordinates (x,y), then θ must varies from 0 to 180 degrees and ρ take values given by Eq 4.2, leading to sinusoidal curves (in the Hough space) for every point in the cartesian plane.

To find the line passing through a set of collinear points in x-y space, we need to find, in the θ-ρ space, the common point where all Hough curves intersect. Fig.4.5 shows two points in the x-y space and the two corresponding curves in the θ-ρ space. The values of ρ and θ where the curves intercept define the straight line passing through the two points in x-y space[4]. The same happens when we have several points defining a straight line as shown in Fig.4.6. Each point generates a sinusoidal curve in the Hough space. The coordinates of the point where the sinusoidal curves intercept define the parameters of the straight line going through the points.

[3]Main direction is defined by the line with the most energetic hits.

[4]A point in x-y space is represented in Hough space as a line, and a point in Hough space is represented as a line in x-y plane.

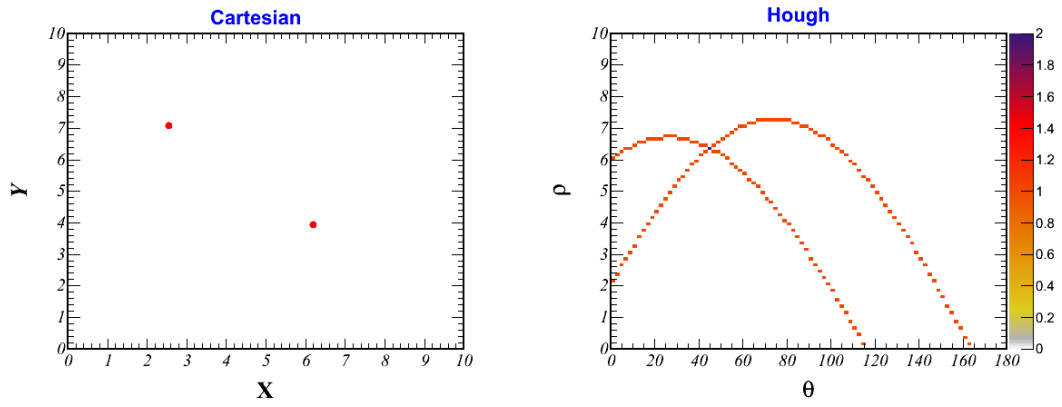

Figure 4.5: Left: 2 single points in the cartesian plane (2 hits in MINERvA detector, for instance). Right: 2 Hough lines defined by the 2 single points, in Hough Space

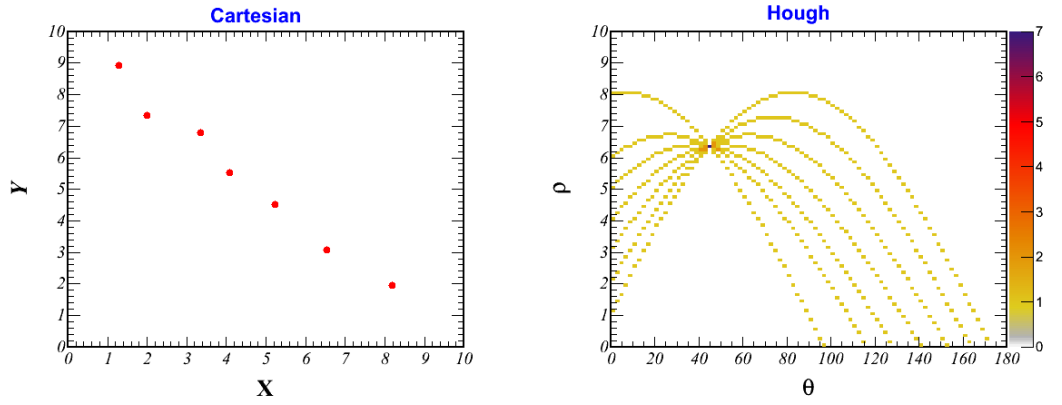

Figure 4.6: Left: Representation of a track seems as a sequence of points. Right: Hough space showing the point where Hough lines are intercepted. This point represents a straight line in the cartesian plane.

Using Hough Transform for shower reconstruction requires a center of reference, the origin of the coordinate system. It would be natural to set the reference at the origin of MINERνA reference system. This choice, however, presents a problem because the lines that we are reconstructing, all of them are located in the detector fiducial region, which is located $6m$ away from the origin of the MINERνA reference system. Many lines get too close to each other, making the reconstruction difficult. An easy solution for this problem is to place the reference point in the most energetic cluster as illustrated in figure 4.7.

Figure 4.8 shows a π^0 event reconstructed by both methods: Angle Scan and Hough Transform. Angle scan works well when the two gammas are well separated but shows a poor performance when the gammas are too close or the separation angle between them is small.

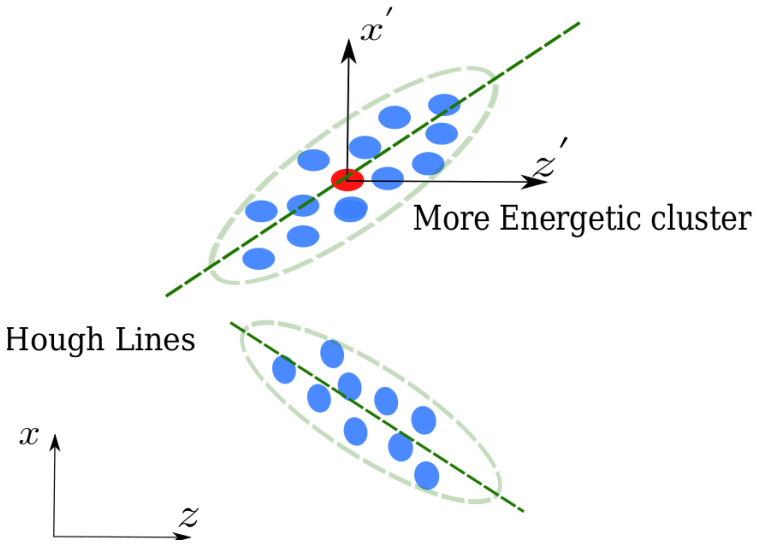

Figure 4.7: Moving the reference point to the most energetic cluster is a simple solution to improve the quality of reconstruction when two gammas are too close to each other.

Note how the Angle Scan didn't find 2 blobs, just 1 blob (red blob). Hough Transform method can handle this kind of event. Note that, this method reconstructs 2 blobs (red blob and green blob). In this thesis both methods are used in order to optimize the π^0 reconstruction.

A question rises from the previous example, if Hough Transform method can reconstruct events where Angle Scan fails, why don't use just the Hough Transform method ?. Figure 4.9 shows the counter example, Hough Transform needs more information to define a line, (it can certainly define a line with 2 hits but, probably it is not our main gamma direction). For this event, the Hough Transform method does not reconstruct 2 blobs (just the red blob). Angle Scan only need to run a scan over all clusters to find evidence of shower. It does not need too many clusters. For this event Angle Scan method reconstructs 2 blobs (green and red).

4.4 Shower Energy reconstruction

To reconstruct the energy of an electromagnetic shower (E_{reco}), we add up the energy of the clusters that belong to the blob. A cluster raw signal must, however, be calibrated to represent the energy of the cluster.

For that purpose we use the calorimetric constants calculated in Cesar Sotelo's Master thesis[78]. We follow equation 4.3, this general formula[5] that includes the calorimetric constants(k_{Traker},

[5]In his thesis Cesar describes every step of the process as well as how to use the calibration constants.

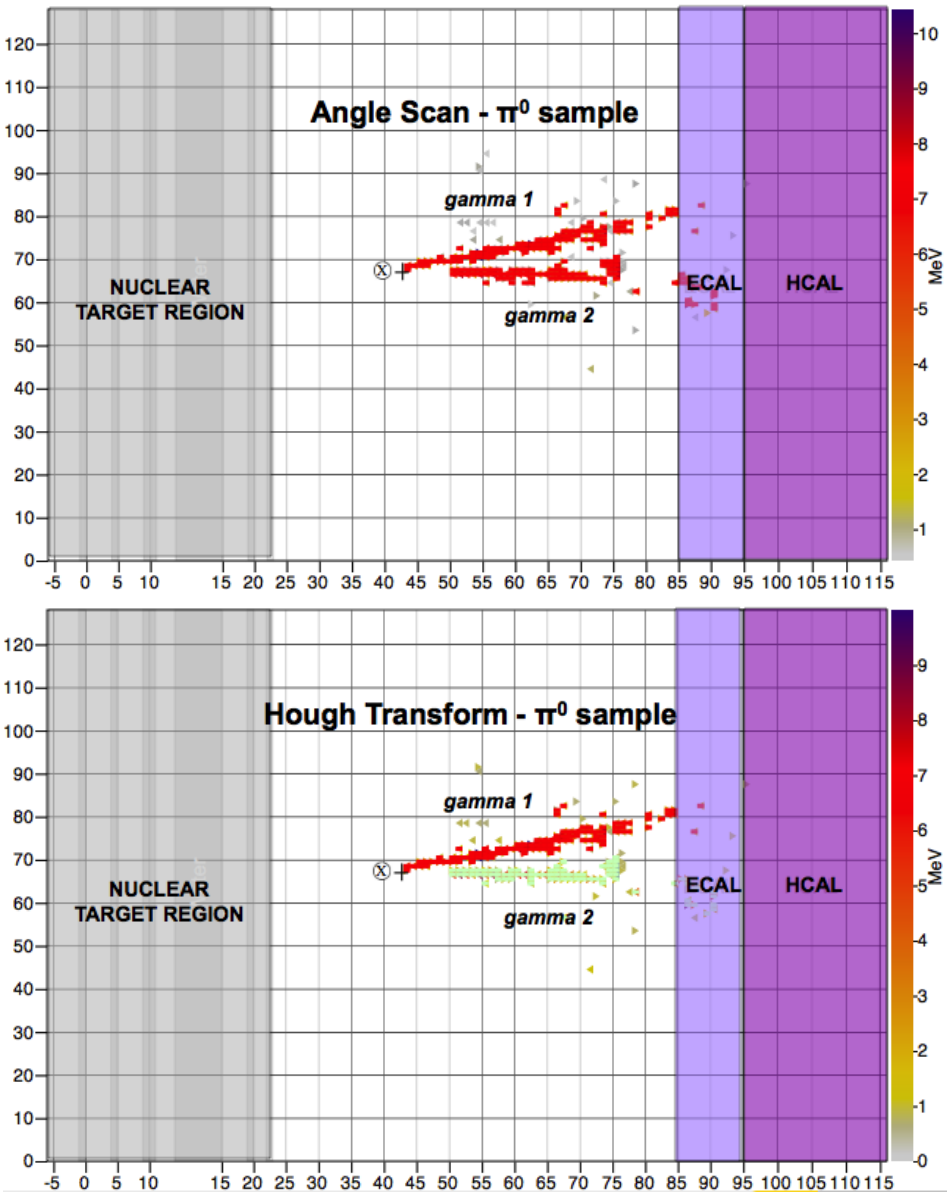

Figure 4.8: Top: Angle Scan applied to an event where the angle between two showers is small. Bottom: Hough Transform applied to a non trivial topology. Both gammas were sucessfully reconstructed.

k_{ECal} and k_{HCal}) for each sub-detector: Tracker, Electromagnetic Calorimeter (ECal) and Hadronic Calorimeter (HCal).

$$E_{reco} = \alpha(k_{Traker}E_{Tracker} + k_{ECal}E_{ECal} + k_{HCal}E_{HCal}), \tag{4.3}$$

here $E_{Tracker}$ is the energy deposited in the tracker, E_{ECal} and E_{HCal} are the energy deposited in the Electromagnetic Calorimeter and the Hadronic Calorimeter.

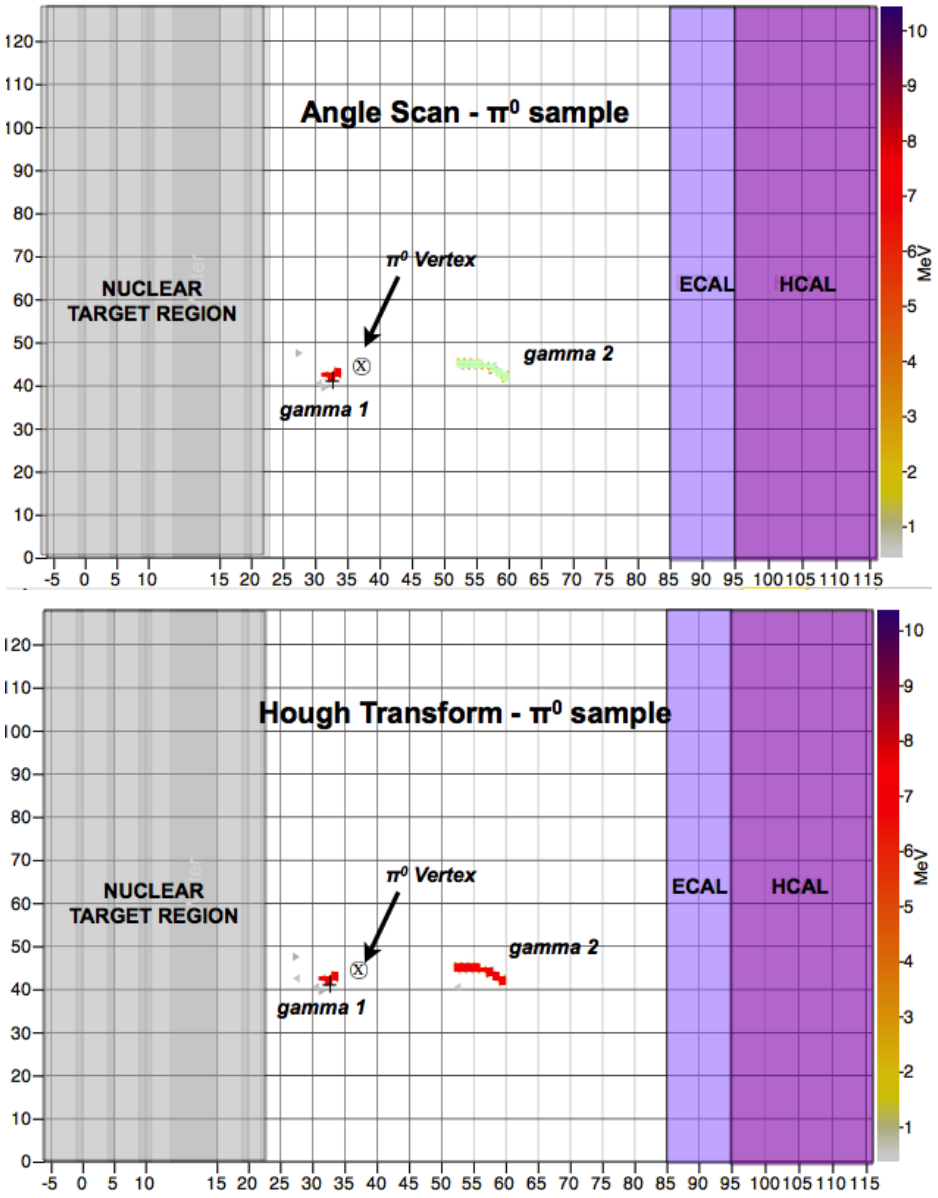

Figure 4.9: Top: Angle Scan applied to a particular π^0 event where there are not many hits to clearly define two lines. There are, however, two well identified cones starting at the π^0 vertex. Bottom: Hough Transform method failed because it was applied to a π^0 event with few points to define two lines.

Analysis are usually restricted to electromagnetic showers reconstructed inside the fiducial volume[6]. When an electromagnetic shower reaches the outside part of the detector we must include additional calibration constants for the Side Calorimeters and Outer Detector as in equation 4.4 in order to get the total energy deposited by the particle.

[6]Volume defined in the subsection.5.2

$$E_{reco} = \alpha(E^{reco}_{Tracker} + k_{ECal}E_{ECal} + k_{HCal}E_{HCal} + k_{OD}E_{OD}), \tag{4.4}$$

where $E^{reco}_{Tracker}$ is given by

$$E^{reco}_{Tracker} = k_{Traker}E^{InnerDetector}_{Tracker} + (2k_E - 1)E^{X-SideEcal}_{Tracker} + (4k_E - 1)E^{U,V-SideEcal}_{Tracker} \tag{4.5}$$

here $E^{InnerDetector}$ is the energy deposited by EM shower inside Inner Detector, $E^{X-SideEcal}$ is the energy deposited in the Side Calorimeters (around Inner Detector).

Table .4.1 summarizes the calibration constants. Calculation of the π^0 invariant mass gives an idea of the quality of the energy reconstruction (see a brief discussion in Section 4.7). These calibration constants are used in the analysis of $CC\pi^0$ inclusive and $CC\pi^0$ exclusive described in Chapter 5 and 6.

Sub-Detector	Calibration Constant
α	1.213
$k_{Tracker}$	1
k_{ECal}	2.28
k_{HCal}	10.56
k_{OD}	27.72

Table 4.1: Calibration Constants for the subdetectors: Tracker, Electromagnetic Calorimeter, Hadronic Calorimeter and the Outer Detector. Taken from [78]

In summary we must first reconstruct the energy of both decay gammas in order to reconstruct the π^0 energy.

$$E_{\pi^0} = E^{reco}_{\gamma_1} + E^{reco}_{\gamma_2} \tag{4.6}$$

The π^0 momentum is the vector sum of the gammas momenta ($\bar{P}_\gamma = E_\gamma \bar{v}_\gamma$, where $\bar{v}$ is vector direction of gamma) given by:

$$\bar{P}_{\pi^0} = E^{reco}_{\gamma_1}\bar{v}_{\gamma_1} + E^{reco}_{\gamma_2}\bar{v}_{\gamma_2} \tag{4.7}$$

4.5 EM shower direction

The direction of the particle that gives rise to a shower can be reconstructed by reconstructing the direction of the shower. Typically 90% of the secondary particles will be traveling

inside of a conical region. Reconstruction of all these particles gives the direction of the originating particle. Figure 4.10 depicts a shower. The direction of the particle that originates the shower is represented by the dotted line that is usually defined by the most energetic hits (darkest colors).

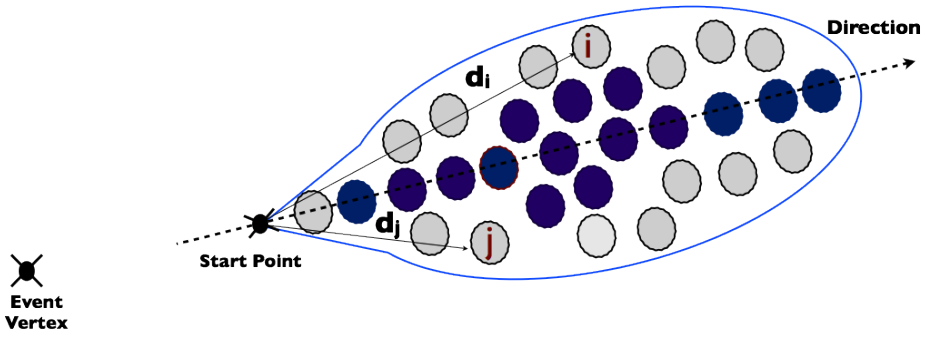

Figure 4.10: EM direction is calculated using every hit inside the blob object

The probability of a secondary particle to travel in the same direction of the originating particle quickly decreases with the distance from the start point. To calculate the shower direction we make a sum of each hit direction weighted by the hit energy and by the inverse of its distance to the start point. As equation 4.8 show for the X component of the direction.

$$Direction_X = \sum_i \frac{(HitPosition_X - StartPoint_X) \times EnergiaHit_i}{d_i} \tag{4.8}$$

4.6 Angle Scan vs Hough Transform

We must either decide which method is the better or combine them to get a higher reconstruction efficiency. For this purpose we apply our methods to a sample of gammas, get the right energy correction factors and then see how good is the calculated invariant mass when these methods are applied to a π^0 sample.

A quick comparison applied of the number of blobs in different samples tells about the behavior and tendency with respect to energy, vertex z position and angle. Photons and π^0 in our samples satisfy the following requirements:

- Energy: 0 - 2 (GeV).
- 200k events.

- Vertex position inside fiducial volume (Subsection 5.2).
- $-\pi < \theta < \pi$.
- $0 < \phi < \pi$.

Fig.4.11 shows the number of reconstructed photons by the Angle Scan and the Hough Transform method. Angle Scan reconstructs more gamma events with 1 blob (more entries reconstructed and bigger percent with 1blob).

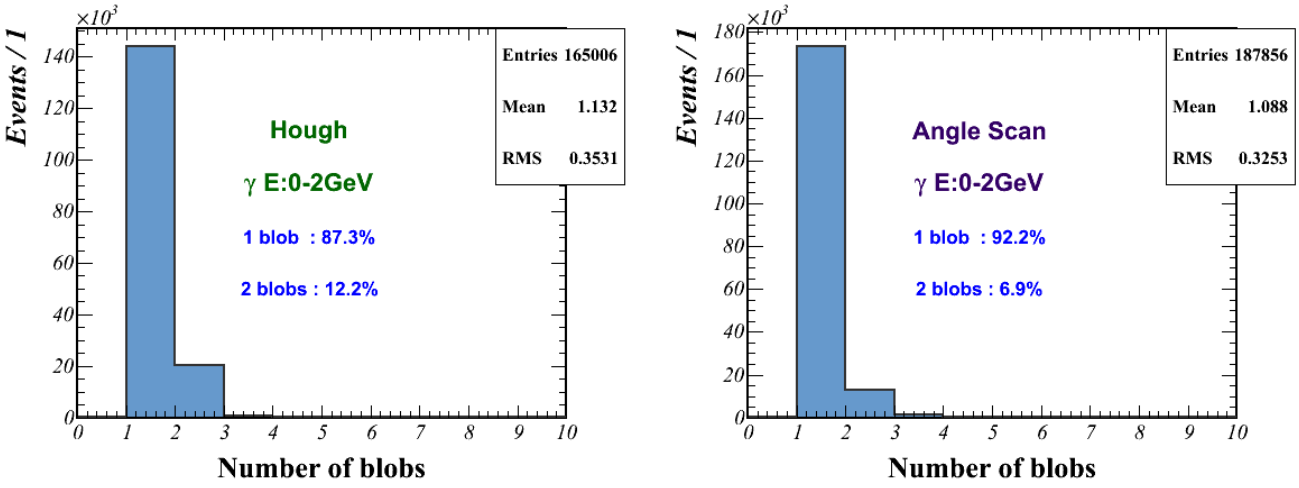

Figure 4.11: Number of blobs for gamma sample. Left: Hough Transform method (∼160 k events reconstructed). Right: Angle Scan method (∼ 180 k events reconstructed).

We do not see any strong evidence of a geometrical or energy dependence as illustrated by the plots in Fig.4.12.

A similar study is performed for a π^0 sample, where we should find two blobs. Angle Scan reconstructs more events with 2 blobs than Hough Transform as shown in figure 4.13. We see that the Angle Scan method has no strong evidence of a dependence with geometry. Figure 4.14 shown the dependence of the number of reconstructed blobs wit the energy and the z vertex. Angle Scan has a good efficiency for low energy π^0's (π^0 with energy less than $0.9GeV$). Beyond this point the Hough Transform becomes more and more efficient with 2 blobs.

4.6.1 Applying Angle Scan and Hough Transform to Photons

We apply both methods to a photon sample, then, in order to verify how good are those reconstructing photons. We need to evaluate them. We reconstruct the energy photon grouping

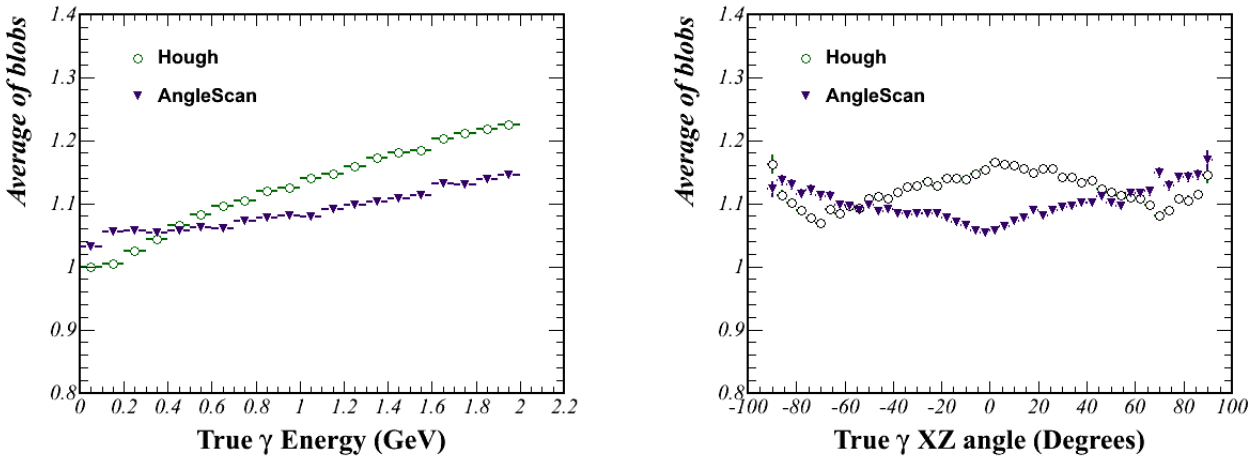

Figure 4.12: Left: number of blobs versus photon energy. Right: number of blobs versus XZ angle (angle between x component and z component direction)

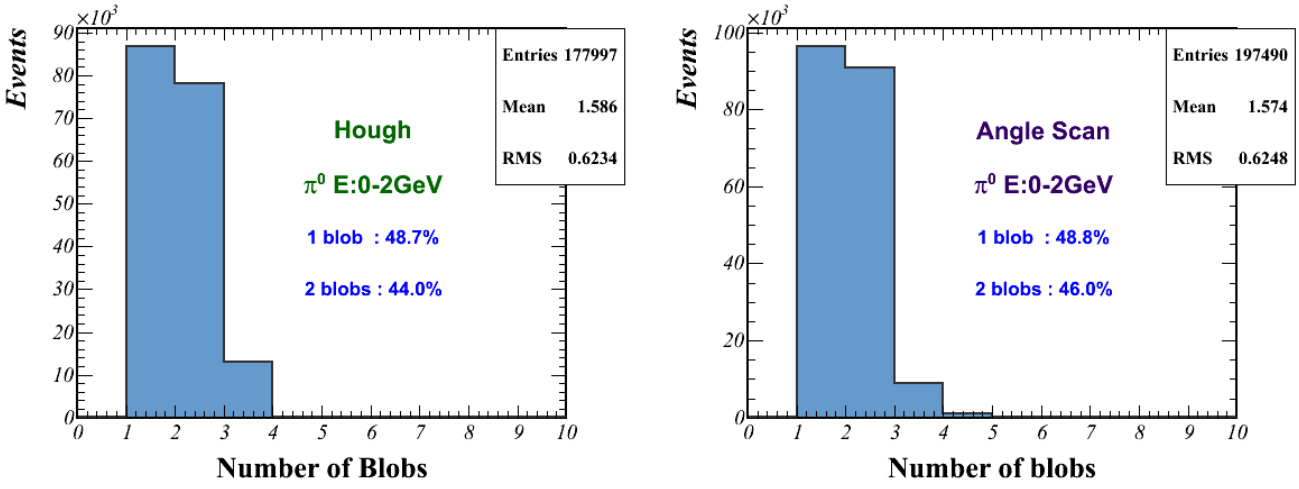

Figure 4.13: Number of blobs for a 200 k π^0 sample. Angle Scan reconstructs more events.

most of the clusters in the detector. Ideally those collected must be all of them, but in the development of a electromagnetic shower, not all particles travel in the same direction, which implies no all clusters are close enough to be reconstructed as the same object. In order to know the percentage of efficiency that our methods grouping clusters, we show the ratio between true and reconstructed energy and the residual for both reconstruction methods. Figures 4.15 and Fig.4.16 for Angle Scan, and for Hough Transform figures 4.17 and 4.18

All these plots have the second gaussian (one) with the center value shifted to the right, indicating that some events should have more energy than reconstructed. That happens for

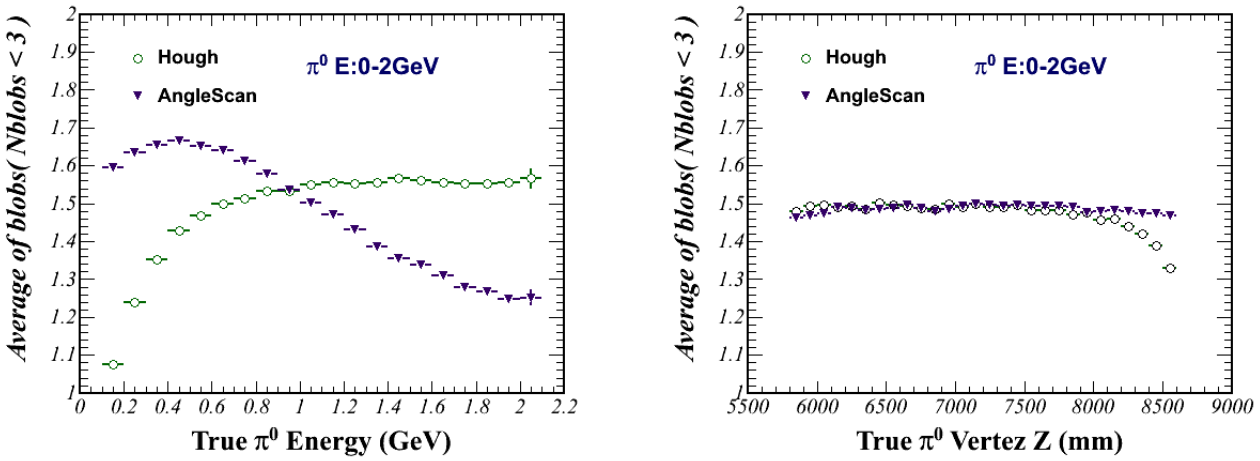

Figure 4.14: Left: number of blobs versus π^0 energy. Right: number of blobs versus z position of the vertex

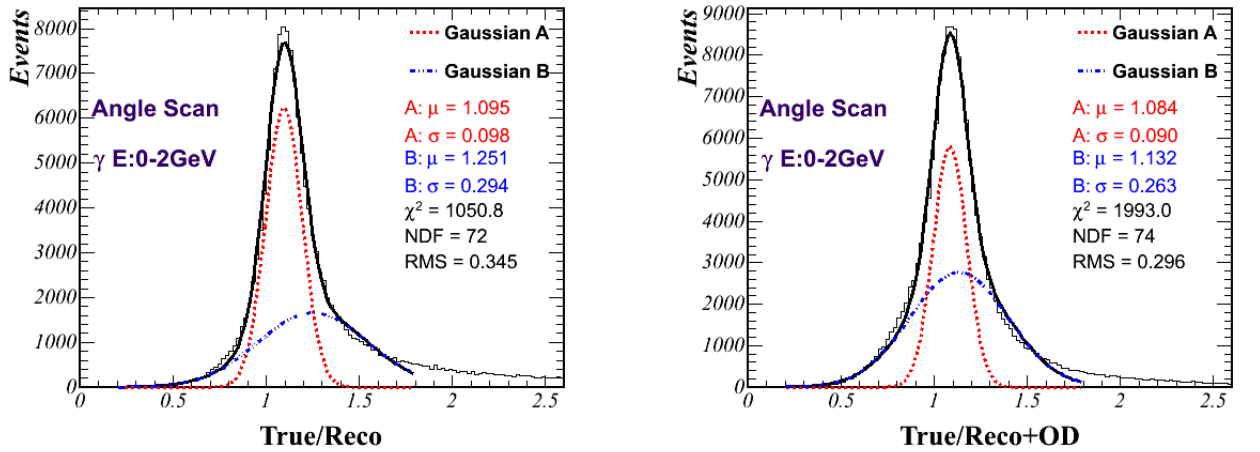

Figure 4.15: Ratio $E_\gamma^{true}/E_\gamma^{rec}$ for the Angle Scan method. Left: without the outer detector. Right: with the outer detector correction.

events that have a shower reaching the outer detector

Right plots in figures 4.15, 4.16, 4.17 and 4.18 show the ratio and residuals for the same sample when the Outer Detector is included in the reconstruction, the second gaussian is not longer shifted.

We reconstruct the momentum of a photon by multiplying its energy (Section 4.4) by its direction (Section 4.5).

Figures 4.19, 4.20 and 4.21 show the residual of the X, Y and Z component of the pho-

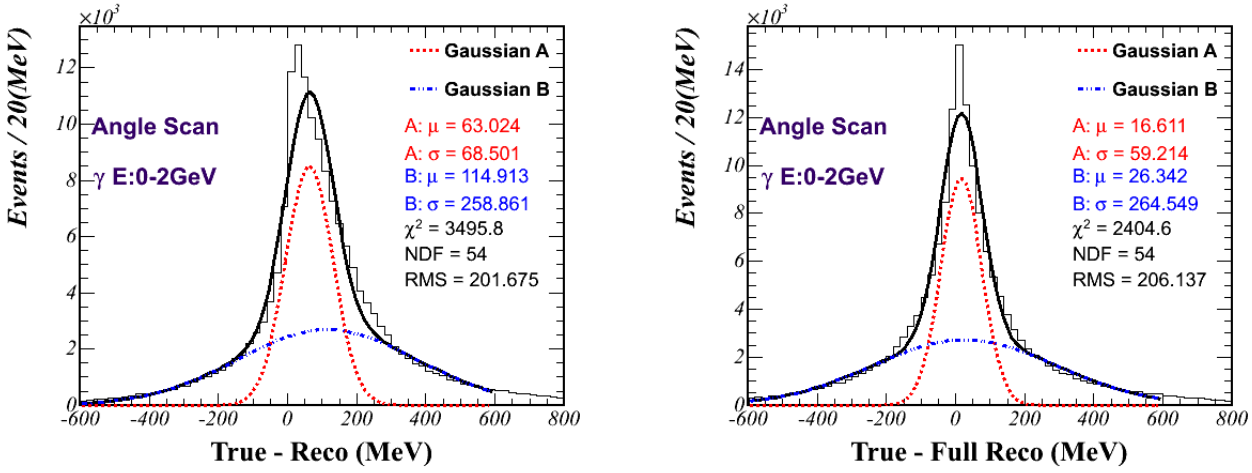

Figure 4.16: Residual (E_γ^{true} - E_γ^{rec}) for the Angle Scan method. Left: without the outer detector. Right: with the outer detector correction.

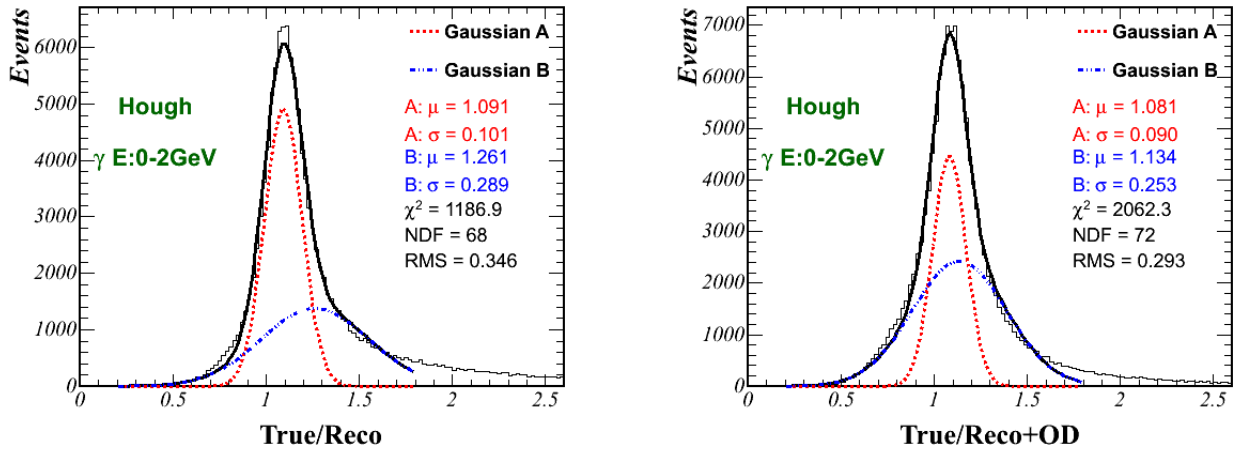

Figure 4.17: Ratio $E_\gamma^{true}/E_\gamma^{rec}$ for the Hough Transform method. Left: without the outer detector. Right: with the outer detector correction.

ton momentum reconstructed. Left hand side for Angle Scan and right hand side for Hough Transform.

The gamma momentum reconstruction is the final reconstruction step for a blob. First we reconstruct the energy (Section 4.4), then we must complement this reconstruction getting the direction (Section 4.5). Multiplying both variables we can get the momentum, we plot the residual of every momentum component on fig.4.19 for the X component, on 4.20 for the Y component and for the Z component on fig.4.21.

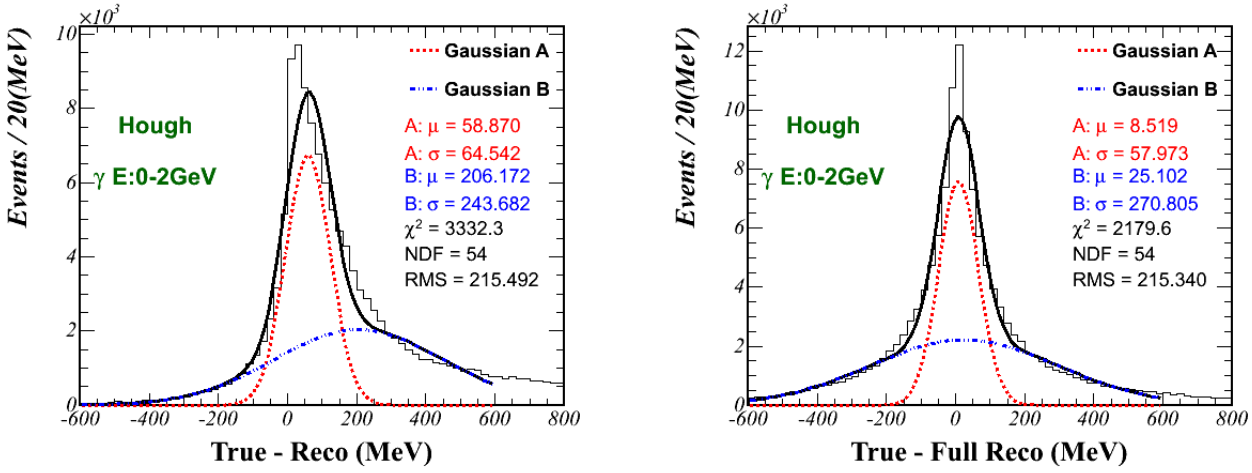

Figure 4.18: Residual (E_{γ}^{true} - E_{γ}^{rec}) for the Hough Transform method. Left: without the outer detector. Right: with the outer detector correction.

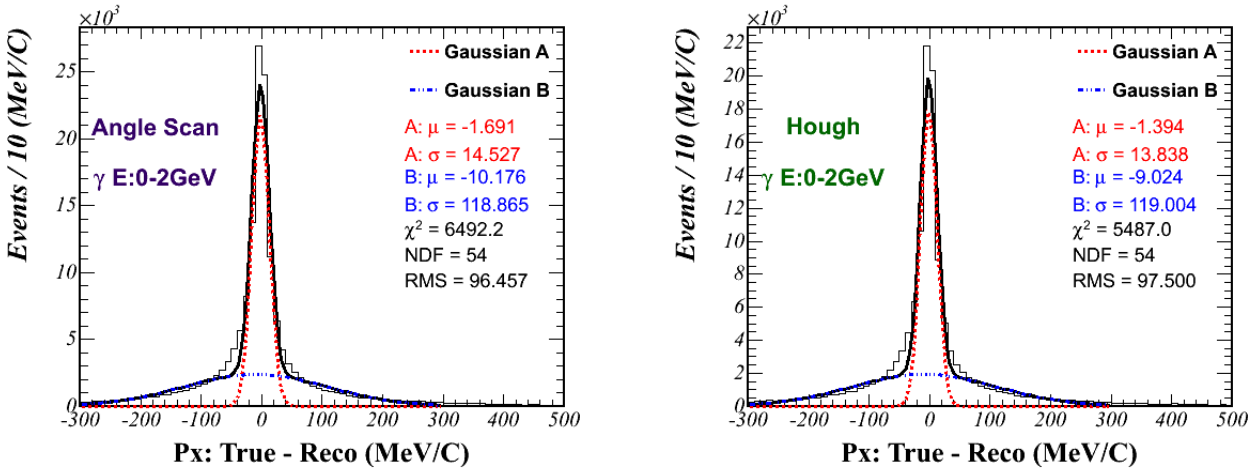

Figure 4.19: Left: Angle Scan, Residual X component of γ momentum. Right: Hough Transform, Residual X component of γ momentum.

4.6.2 Angle Scan and Hough Transform on π's

π^0's momentum reconstruction must be qualified for both methods. The incoming plots represent the residual of every momentum component, the equation 4.7 is used for the π^0's momentum reconstruction. Figures 4.22, 4.23 and 4.24 show the residual for the π^0's for each reconstruction method.

The Hough Transform has better efficiency for energies bigger than $0.9GeV$. It means high efficiency for big Pz component.

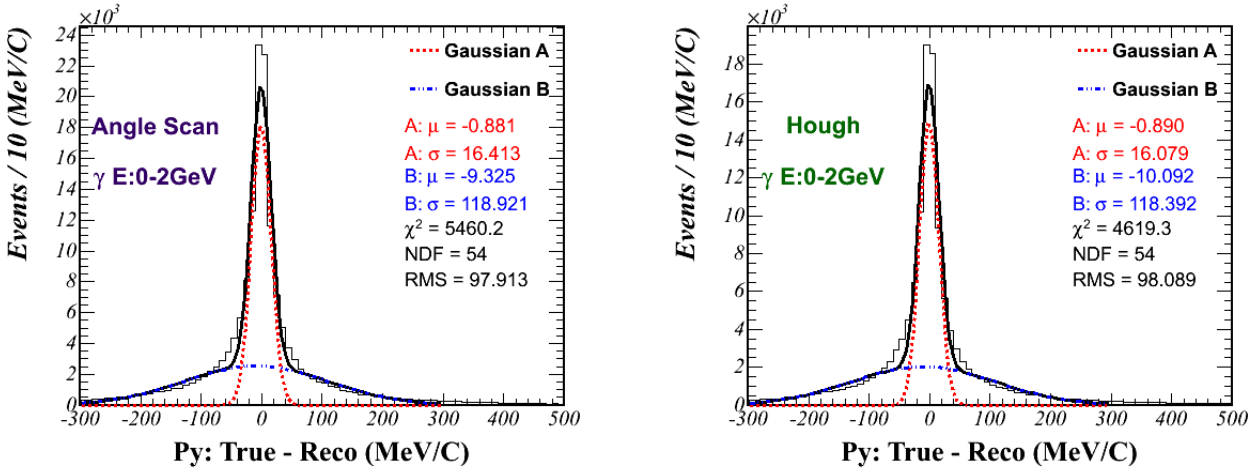

Figure 4.20: Left: Angle Scan, Residual Y component of γ momentum. Right: Hough Transform, Residual Y component of γ momentum.

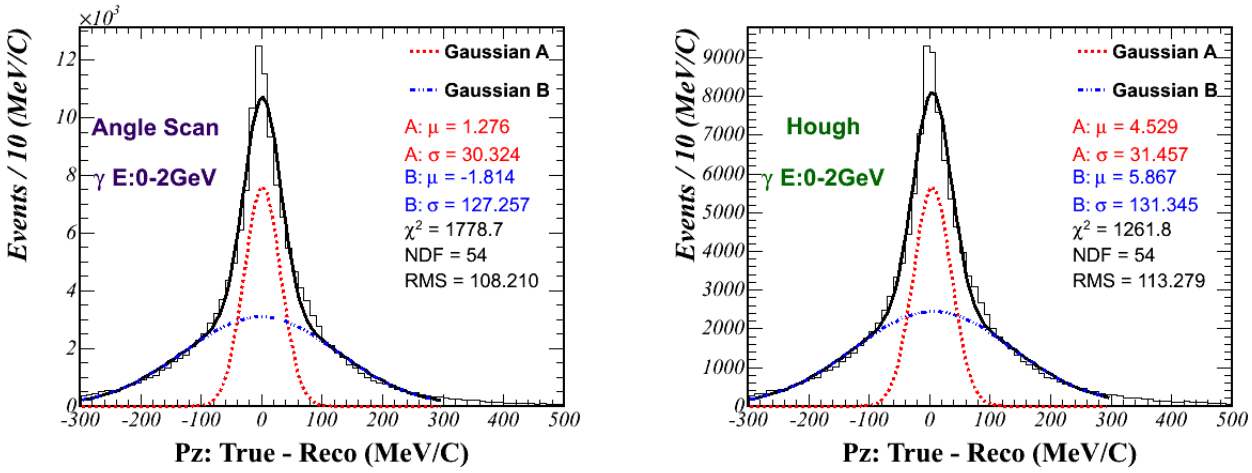

Figure 4.21: Left: Angle Scan, Residual Z component of γ momentum. Right: Hough Transform, Residual Z component of γ momentum.

4.6.3 Summary

After comparing residuals and ratios for gammas and π^0s, we can not strongly recommend any method over the other. Figure 4.14 shows that Hough Transform reconstructs more blobs for higher energy π^0.

For our $CC\pi^0$ reconstruction we apply both methods. If the energy of all clusters reconstructed by the MINERνA track algorithm is less than $900MeV$ we run Angle Scan otherwise, we run Hough Transform. If the Angle Scan fails (do not find 2 blobs) we run the Hough

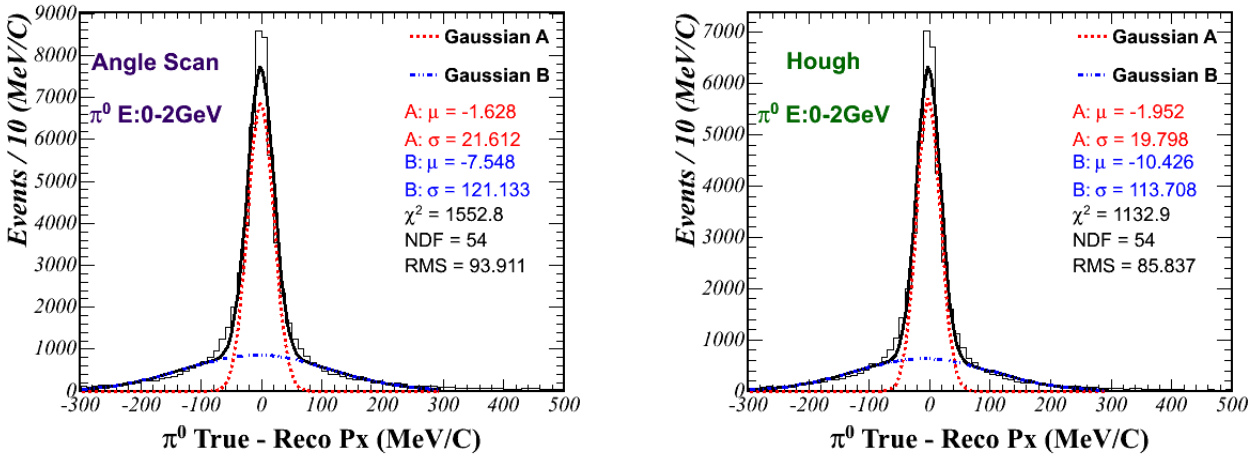

Figure 4.22: Left: Angle Scan, Residual X component of π^0 momentum. Right: Hough Transform, Residual X component of π^0 momentum.

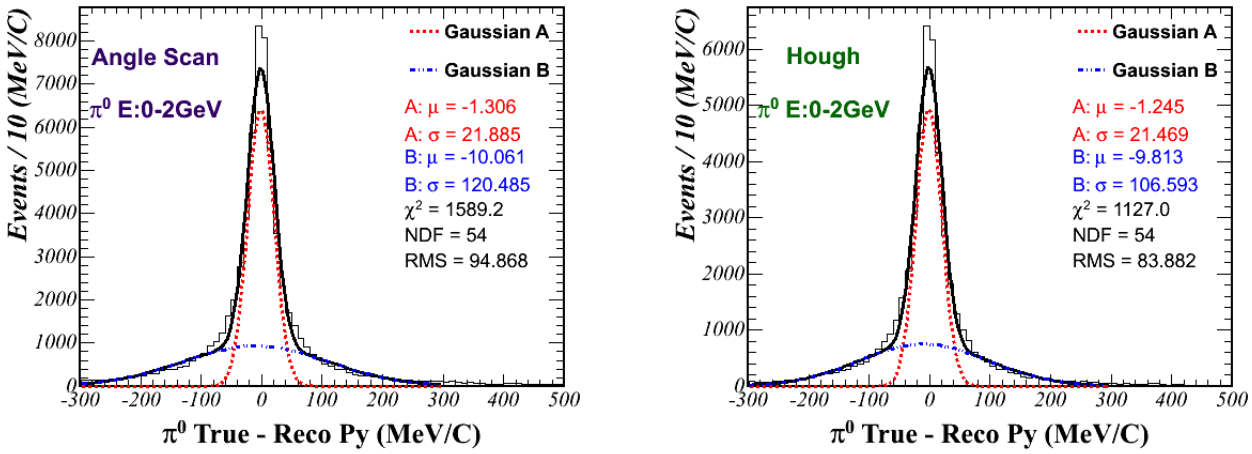

Figure 4.23: Left: Angle Scan, Residual Y component of π^0 momentum. Right: Hough Transform, Residual Y component of π^0 momentum

Transform method.

We summarize all residuals and ratios calculated from the comparison between reconstructed and True Monte Carlo. Table 4.2 summarizes the ratio and residual for each method.

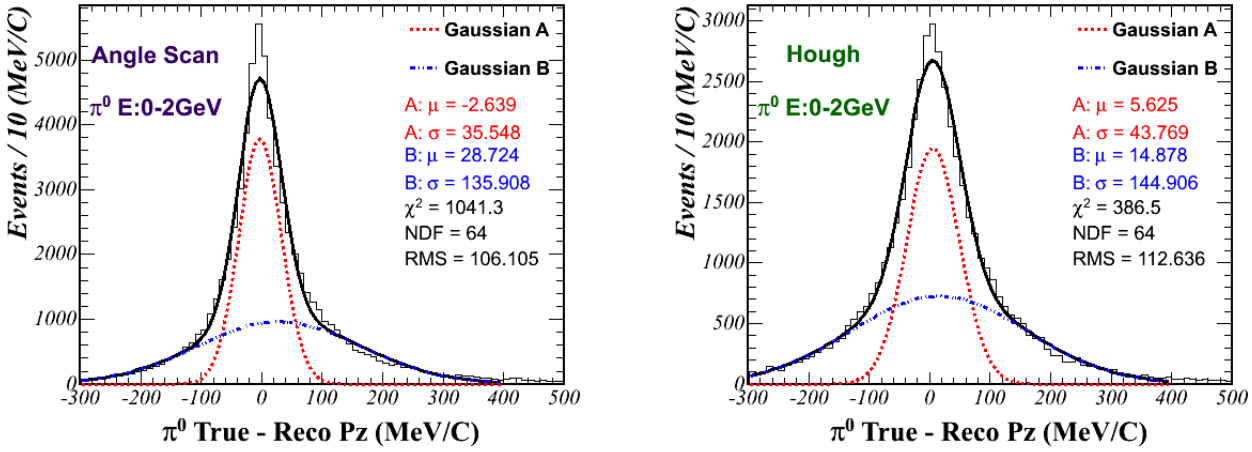

Figure 4.24: Left: Angle Scan, Residual Z component of π^0 momentum. Right: Hough Transform, Residual Z component of π^0 momentum

	Hough Transform	Angle Scan
γ Energy ratio	1.08	1.08
γ Energy residual	8.52 MeV	16.6MeV
γ Momentum residual P_x	-1.39 MeV	-1.69 MeV
γ Momentum residual P_y	-0.89 MeV	-0.88 MeV
γ Momentum residual P_z	4.53 MeV	1.28 MeV
π^0 Momentum residual P_x	-1.95 MeV	-1.63 MeV
π^0 Momentum residual P_y	-1.24 MeV	-1.31 MeV
π^0 Momentum residual P_z	5.62 MeV	-2.64 MeV

Table 4.2: Summary ratios and residual table for Angle Scan and Hough Transform methods, we defined Residual = True Monte Carlo - Reconstructed Monte Carlo, and Ratio = True / Reconstructed

4.7 π^0 Invariant Mass

If two photons are observed (reconstructed) in the detector with energies E_{γ_1} and E_{γ_2} and angle θ between them, how we must get the invariant mass. Since a photon has no mass, its energy and momentum are the same ($E_\gamma = P_\gamma$ and $q_\gamma^2 = m = 0$), so energy-momentum 4-vector conservation can be written as:

$$
\begin{aligned}
q_{\pi^0} &= q_{\gamma_1} + q_{\gamma_2} \\
q^2_{\pi^0} &= q^2_{\gamma_1} + q^2_{\gamma_2} + 2(q_{\gamma_1} \cdot q_{\gamma_1}) \\
M^2_{\pi^0} &= 2(E_{\gamma_1} E_{\gamma_2} - P_{\gamma_1} \cdot P_{\gamma_2})
\end{aligned}
\tag{4.9}
$$

The identification of neutral pions (and other neutral mesons) is usually based on the invariant mass analysis of photon pairs detected in an electromagnetic calorimeter Eq.4.10

$$
M_{\gamma_1\gamma_2} = \sqrt{2E_{\gamma_1}E_{\gamma_2}(1 - cos\theta_{\gamma_1\gamma_2})}
\tag{4.10}
$$

Figures 4.25 shows the π^0 invariant mass reconstructed by our two methods. The shape of the π^0 peak in the invariant mass spectrum reflects the energy and angular resolutions of the π^0 reconstruction.

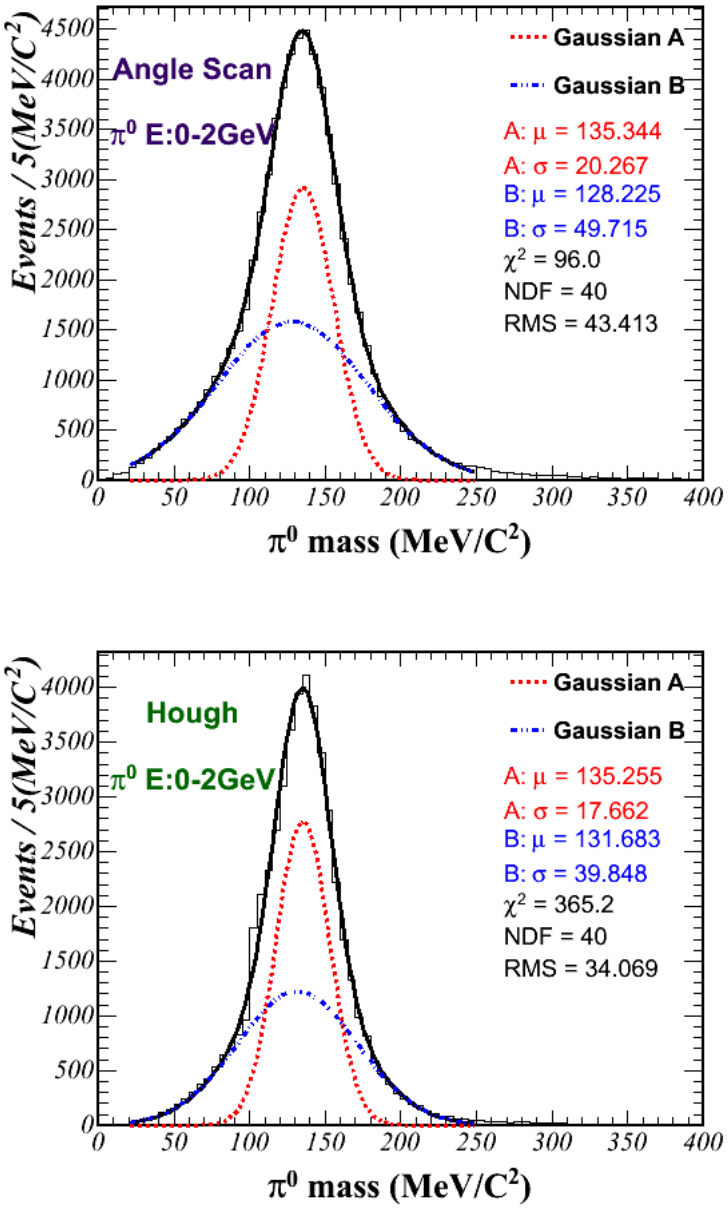

Figure 4.25: Top: π^0 invariant mass (Angle Scan method). Red Gaussian mean value equals to 135.34. Bottom: π^0 invariant mass (Hough Transform). Gaussian mean value equals 135.25.

Chapter 5

Simulation and Event Selection

5.1 Introduction

We must define which selection criteria we should apply to select our sample of $CC\pi^0$ inclusive and $CC\pi^0$ exclusive. The definition of our samples is strongly related to the final state particles as defined by our Monte Carlo. We do not reconstruct all final state particles from every reconstructed event. We mainly reconstruct antimuons and neutral pions. We compare our data and Monte Carlo for every reconstructed variable. We describe the main components of our simulation, like Beam simulation, neutrino interactions simulation, MINOS simulation. We emphasize the muon reconstruction and how MINOS near detector is fundamental to our analysis.

5.2 Fiducial Volume

The analysis makes the following requirements for the interaction vertex location:

- inside an hexagon centered at the detector z axis with apothem less than 850 mm.
- Z-component between 5990 mm and 8340 mm. This translates to a reconstructed vertex between modules 25 and 81, counting a total of 57 modules or 114 planes.

The superficial mass density of carbon in the tracker region is $\rho_C = 1.774 g/cm^2$ and the superficial mass density of all scintillator planes corresponds to $\rho_T = 1.811 g/cm^2$ in total. The area of the hexagon is:

$$A = a^2 \times N \times tan(\frac{180}{N}) = (85cm)^2 \times \frac{6}{\sqrt{3}} = 25028.1cm^2 \tag{5.1}$$

where a = 85 cm is the apothem and N = 6 is the number of sides of the hexagon. This leads to a fiducial mass of carbon given by:

$$A \times \rho_C \times 114 \times 1/1000 = 5.061 tons \tag{5.2}$$

and a total of:

$$A \times \rho_T \times 114 \times 1/1000 = 5.167 tons. \tag{5.3}$$

5.3 Muon Charge

MINERνA μ^+ and μ^- reconstruction consider tracks that can be matched to a MINOS track that provides information on the momentum. Muons that stop in our detector are not used. We consider muons that exit from one of our last five modules and can be matched to a reconstructed muon on MINOS. We use the momentum reconstructed by MINOS and the charge is defined by the track curvature as measured by MINOS.

$\mu-$ are associated to a negative track curvature:

$$\rho \equiv \frac{q}{p} < 0 \tag{5.4}$$

and μ^+ are identified by a positive track curvature:

$$\rho \equiv \frac{q}{p} > 0. \tag{5.5}$$

5.4 Our sample

We use data taken between October 2010 and February 2011 (see figure 5.1). This period is called MINERνA list 5. And correspond to 1.019×10^{20} protons on target (POT) have been analyzed. Monte Carlo sample corresponding to 2.579×10^{20} protons on target have been analyzed.

5.5 Simulation in MINERνA

Simulation involves several different Monte Carlo (MC) packages. We use the GENIE [79] package, version 2.6.2, to simulate neutrino interactions and final state interactions within the target nucleus. We use GEANT4 package to model several different systems. GEANT4 is a C++ based object oriented simulation package used to simulate the basic physical interactions of particles with matter [80]. GEANT4 is an integral part of the G4numi package that we

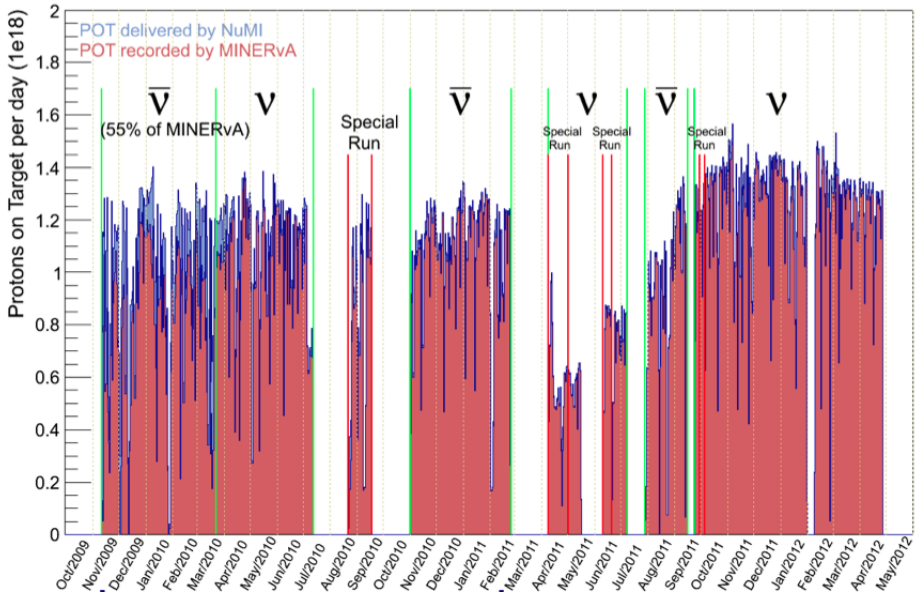

Figure 5.1: Total data collected by MINERνA at LE beam configuration. ν_μ LE 3.98×10^{20} POT, $\bar{\nu}_\mu$ LE 1.70×10^{20} POT and special runs 4.94×10^{19} POT

use to simulate the neutrino and anti-neutrino fluxes. G4numi uses GEANT4 version v9.2p03. We use Geant4 to simulate the behavior of the final state particles predicted by the GENIE simulation. This involves simulating the amount of energy deposited by a given particle in each step as well as modeling any multiple scattering or secondary interactions that may occur.

The second step of the simulation involves modeling the actual detector components. The energy deposits predicted by GEANT4 are converted into a prediction of the number of photons generated in the scintillator. This includes accounting for Birks Law that describes how the light yield from energy deposited in scintillator saturates for larger energy deposits [81]. The capture of light by the WLS fiber and its path to the PMT are also simulated. We model the quantum efficiency of the anode on the PMT, which converts a percentage of light from the WLS fiber into electrons that can be accelerated in each stage of the PMTs. A complete description about MINERνA simulation could be found in [82]

5.5.1 Simulation of the NuMI Beam

We simulate the NuMI Beam, predicting the spectrum of pions and kaons that produce the ν and $\bar{\nu}$ that are observed in the MINERνA detector [83]. These fluxes are produced with the FTFP and QGSP physics models of GEANT4 9.2p03 [80] to model hadron production and re-interactions within the target system. A multiplicative factor is applied to some events to correct for model's imprecisions.

Two exterior data sets are used to reweight the predicted pion and kaon distributions created by 120 GeV protons colliding with the NuMI target. For pions with $x_F < 0.5$, NA49 data [84] is used to reweight pion production cross-sections, where x_F is Feynman x defined [27].

$$x_F = \frac{2p_L}{\sqrt{s}} \tag{5.6}$$

where p_L is the longitudinal momentum, and s is the square of the center of mass energy. The Large Acceptance Hadron Detector for an Investigation of Pb-induced Reactions(NA49) at the CERN SPS, studied pion production from proton-carbon collisions for protons with momentum equal to 158 GeV/c. For $x_F > 0.5$, both data from NA49 and Barton, et al.[85] are used to reweight the sample. Production cross-sections for kaons are also reweighted using NA49 data, but only for $x_F < 0.2$. For all other events, no reweighting is applied. For regions of x_F where we apply reweighting, we do so based on values of x_F and p_T, where p_T is the transverse momentum. We compare a simulated cross section with the one measured in the Barton and NA49 data as a function of x_F and p_T. We then reweight events based upon the differences of the cross section in data and simulation. We show reweighted flux plots using this method on figures 5.2 and 5.3.

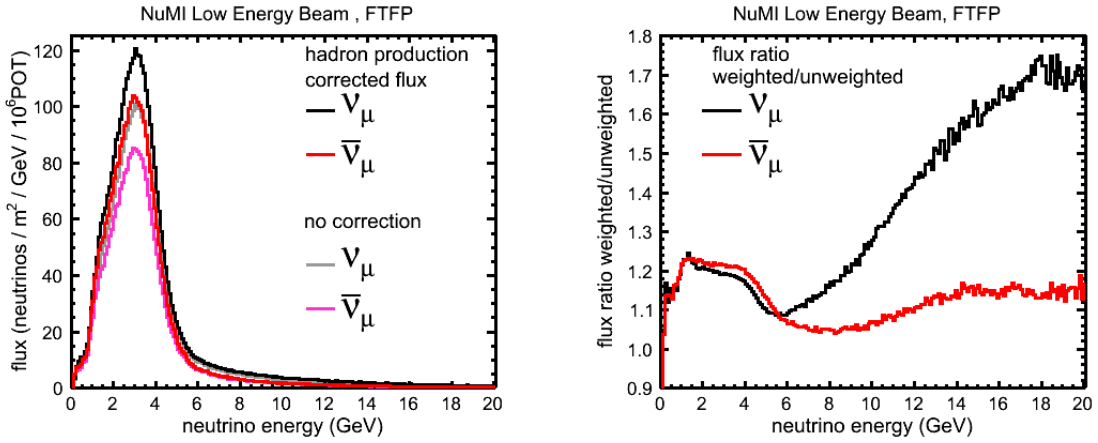

Figure 5.2: Overlay and ratio plots of the simulated flux before and after the central value reweighting procedure has been applied for **FTFP**. The label ν_μ refers to the distribution of ν_μ's in the FHC beam while the label $\bar{\nu}_\mu$ refers to $\bar{\nu}_\mu$'s in the RHC beam. Plot Courtesy of M. Kordosky

This re-weighting scheme cannot be applied for all simulated neutrino interactions. For these cases, we use the hadron models to simulate the flux. We use the resulting spread of predictions in the "1000 universes" method described in section 6.2. In all cases, we simulate the in flight decay of pions and kaons to muons, neutrinos, and anti-neutrinos.

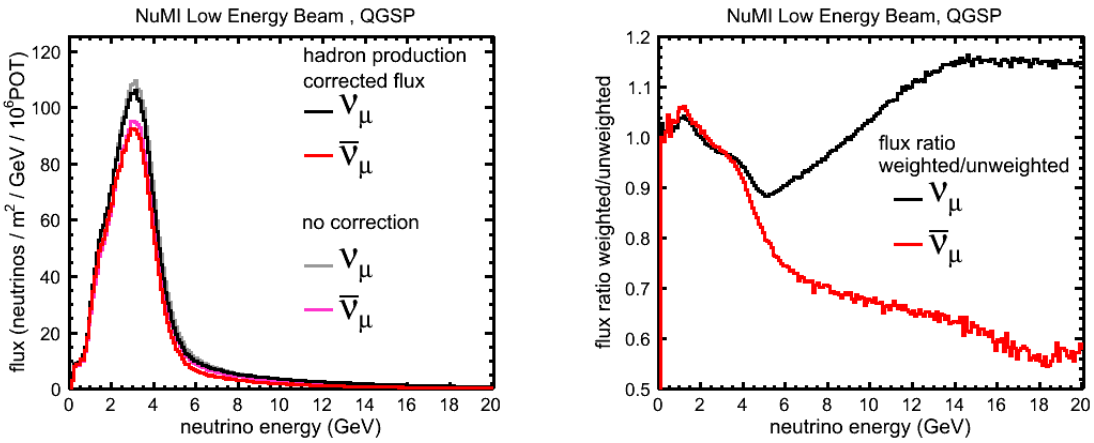

Figure 5.3: Overlay and ratio plots of the simulated flux before and after the central value reweighting procedure has been applied for **QGSP**. The label ν_μ refers to the distribution of ν_μ in the FHC beam while the label $\bar{\nu}_\mu$ refers to $\bar{\nu}_\mu$'s in the RHC beam. Plot Courtesy of M. Kordosky

5.5.2 The GENIE Simulation

GENIE is a C++ and ROOT [86] based simulation package created for modeling neutrino interactions in matter[1]. Various interaction models are used for predicting the cross-section for different types of processes.

- **Quasi-Elastic Scattering:** Quasi-elastic scattering ($\nu_\mu + n \rightarrow \mu + p$) is modeled using an implementation of the Llewellyn-Smith model [34].
- **Elastic Neutral Current Scattering:** Elastic neutral current processes are computed according to the model described by Ahrens et al [87].
- **Baryon Resonance Production:** The production of baryon resonances in neutral and charged current channels is included with the Rein-Sehgal model [88]. This model employs the Feynman- Kislinger-Ravndal [89] model of baryon resonances.
- **Coherent Neutrino-Nucleus Scattering:** Coherent scattering results in the production of forward going pions in both charged current and neutral current channels. Coherent neutrino-nucleus interactions are modeled according to the Rein-Sehgal model [90].

[1] We use GENIE version 2.6.2 in this thesis

- **Non-Resonance Inelastic Scattering:** Deep (and not-so-deep) inelastic scattering (DIS) is calculated in an effective leading order model using the modifications suggested by Bodek and Yang[91] to describe scattering at low Q^2.
- **Neutrino-Electron Elastic Scattering:** The cross sections for all ν_e scattering channels other than Inverse Muon Decay is computed according to [92].

We generate events using the GENIE simulation by acquiring an energy and neutrino flavor from the beam simulation. Using a random number seed, we then generate a particular interaction based upon that random number seed and the predicted likelihood for the different interactions.

5.5.3 MINOS simulation

We need to simulate Muons passing through the MINERνA and MINOS Detector. This is done by passing the position, type, and the four-momentum of that muon to the MINOS simulation. The MINOS simulation uses GEANT3 to model the MINOS detector and the magnetic field present within that detector. This simulation runs separately and independently from the MINERνA simulation as well as the MINERνA software framework.

5.6 Processing Data in MINERνA

The same high level processing steps are employed for data and the simulation. Several steps of processing occur.

5.6.1 Matching MINOS and MINERνA

One of the earliest stages of high level processing is combining MINOS and MINERνA detector information. This includes associating MINERνA gates and MINOS snarls with each other. A MINOS snarl is similar to a MINERνA gate. In the case of data, gates and snarls are matched using GPS timing information. In the case of the simulation, a given MINERνA gate and MINOS snarl are known to be associated a priori. For a given MINOS snarl, we run the full MINOS reconstruction prior to gate and snarl matching. This reconstruction includes a MINOS track finding algorithm, which uses a Kalman Filter and accounts for multiple scattering and deflection due to the magnetic field.

5.6.2 Forming Time Slices

Given the fine timing resolution of MINERνA and the timing calibrations that we apply, most neutrino interactions have a narrow time profile. Since multiple interactions can occur within the detector, separating interactions by their time offers an effective way of disentangling interactions that would otherwise overlap in space. To do this, hit times are sorted using a Heap Sort [93].

Once hits are ordered, a sweep start finding hits concentrations over time. If at least two hits with minimal charge associated with them are located within a particular window, the hits are grouped into a time slice. The hits are then added to this segment of time if they occur near the initial hits in the time slice.

The time slice is then used as the basic unit in processing for the remainder of reconstruction. On figure 5.4 we can see a MINERνA gate. The top represents the hit time distribution, and we represent 3 different time slices and the complete event.

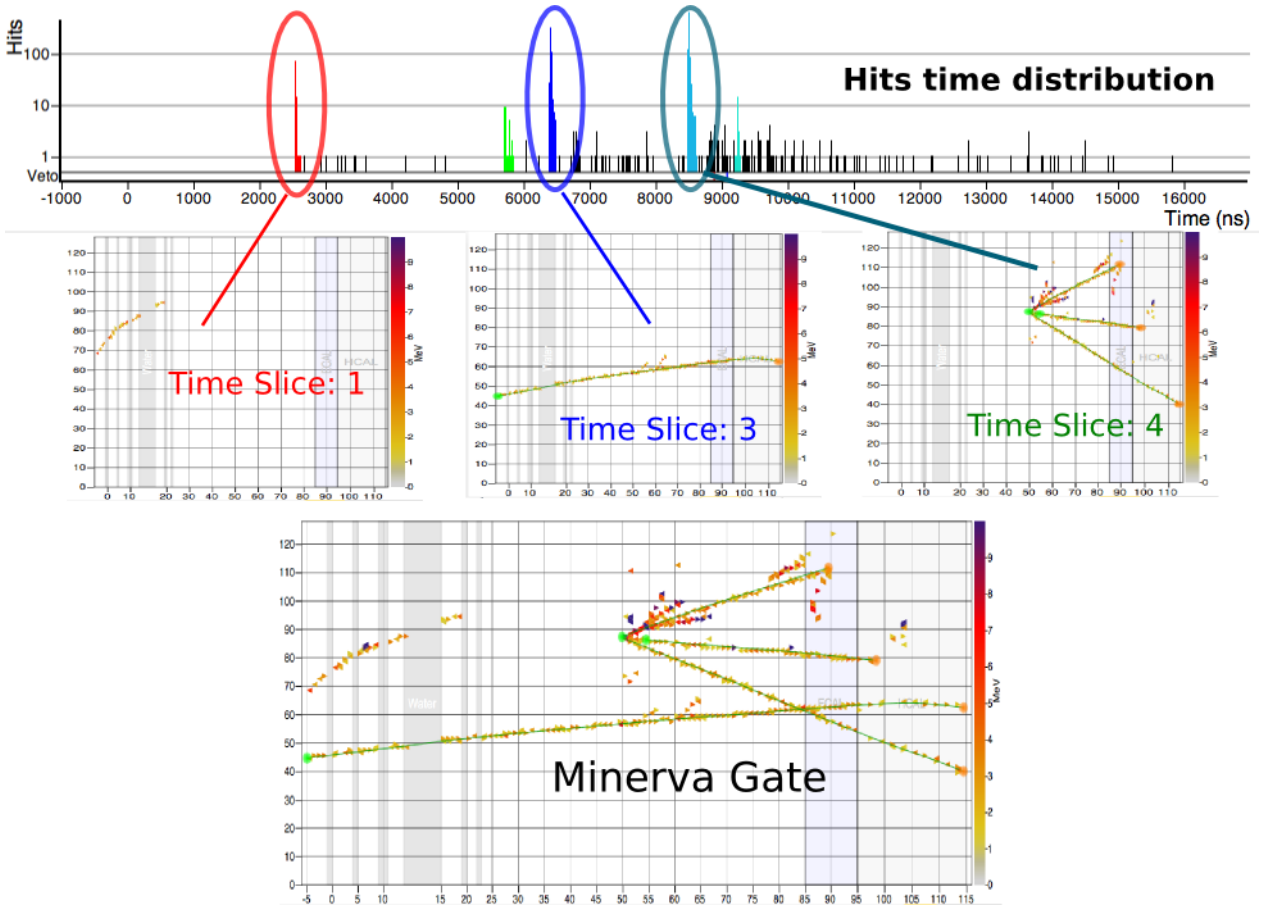

Figure 5.4: Event display showing single time slices and all hits deposited in our detector during a MINERνA gate $\sim 16ns$

5.6.3 Clustering

To form clusters, we look for hits adjacent to each other within a plane within a given time interval(time slice). Any space between hits leads to a new cluster group, where a space is a strip that does not register a hit. An isolated strip with a hit and without neighbors which recorded a hit is promoted to a cluster.

An illustration of clusters being formed from strips is shown in figure 5.5

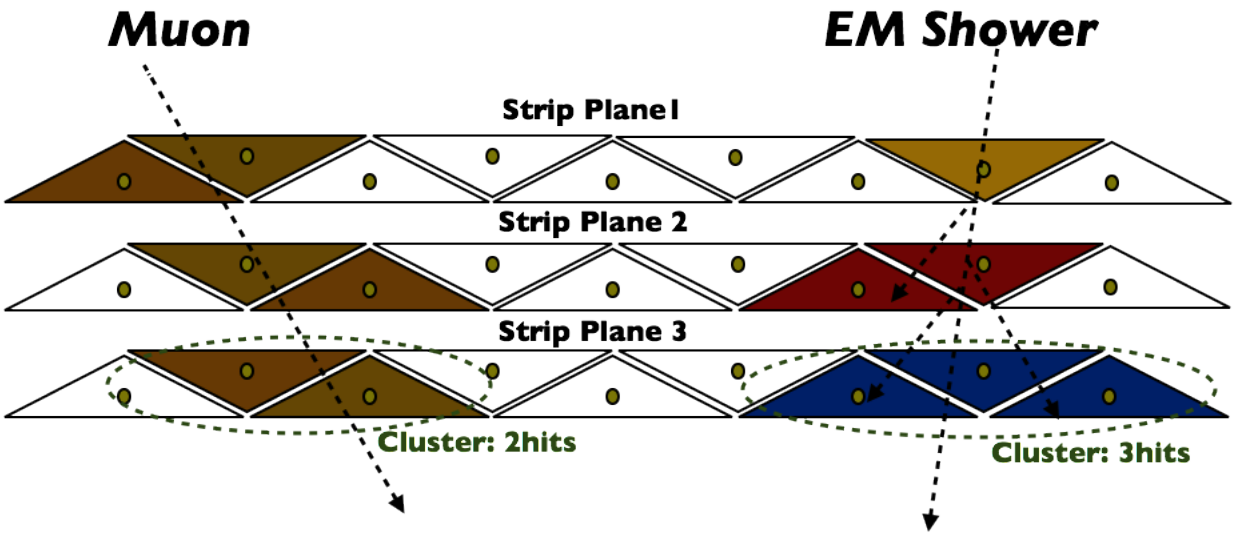

Figure 5.5: Clustering example. Adjacent hits within a strip plane create a cluster

The cluster position is calculated using weighting all entries by their energy. The time of the energetic hit is considered to be the time of the cluster.

We classify the resulting clusters by their composition as:

- **Low activity clusters:** Clusters with less than 1 MeV are considered low activity clusters.
- **Trackable clusters:** Total cluster energy must be less than < 12 MeV and bigger than 1 MeV. The hits, must have either one or two hits with hit energy ≥ 0.5 MeV, and be directly adjacent to each other.
- **Heavy ionizing clusters:** Total cluster Energy ≥ 1 MeV, four or less hits. Must have one, two, or three hits each with hit energy ≥ 0.5 MeV, and they must all be directly adjacent to each other and not qualify as a trackable cluster.
- **Superclusters:** Any cluster with more than 1 MeV in energy that does not meet the criteria for either trackable or heavy ionizing clusters is classified as a supercluster

- **Cross-talk clusters:** A cluster is identified as a cross-talk cluster by inspecting the PMT pixels associated with hits within that cluster.

5.6.4 Tracking

Photons and charged particles usually deposit energy in each plane. We identify these deposits and use them to reconstruct the path of the particles. In MINERνA we refer to the resulting reconstructed object as a track.

The muon is one of the easiest particles to find. Removing the activity associated with a muon generally improves the overall success rate of finding other tracks and the vertex of the muon track is usually the neutrino interaction vertex. After finding the muon we search for other tracks using the same tracking procedure we use to find the muon.

The steps followed to find tracks are:

1. **Making Track Seeds and Track Candidates:** The basic step in the tracking process is making two dimensional track seeds(Track seeds per view X, U and V). To make these seeds, we sort trackable and heavy ionizing clusters by their location along the Z-axis. Track seeds are then found by looking for clusters within planes with the same view for three clusters that are in a line. We fit the three clusters (enforcing a minimum $\chi 2$ value). Only tracks seeds that pass the cut are considered in the next step. Then, we merge track seeds into track candidates. We initiate this in the downstream end of the detector and work upstream. The result is two dimensional track candidates each composed of clusters in a single view. We then attempt to merge recently formed track candidates comparing the slope and slope intercepts. If the two are similar enough, we combine them into a single track candidate.

2. **Kalman Filter:** We use a Kalman filter implementation that incorporates multiple scattering to fit a track using a Kalman filter [94]. The Kalman filter is a recursive method that takes input data to make a statistically optimized prediction assuming a linear system which is then used as an input for the next iteration of the filter. The multiple scattering calculation incorporates material information for the region of the detector the track is traversing as well as the mass of the particle. For the first round of tracking where we search for a muon track, we use the mass of the muon in calculating multiple scattering.

3. **Track Cleanup:** After the above step, we inspect each track to determine whether the object should be divided into two parts. Looser standards regarding gaps along a track

are initially used since some activity related to the track may be part of a supercluster and thus not available for forming a track. If no activity is found to fill the empty spaces along a track, we call them gaps. If this gap is too large, we split the track into two separate pieces, considering that it is caused by interactions of separated particles.

4. **Applying the Tracking Algorithm** As mentioned above, after reconstructing the muon track we search for hadronic particles. The track we consider most likely to be the muon is saved and all other tracks deleted. We then use the muon track as an anchor to find hadronic particles with the same vertex. We take the remaining trackable and high ionizing clusters and repeat the above tracking algorithm with the requirement that tracks must have a common vertex with the muon. A Kalman filter fit is done to the track and vertex system. Any tracks that do not have a vertex consistent with the muon track are deleted. Track cleanup is performed on the newly created tracks splitting them if large gaps exist within the track. We repeat this anchor-based tracking using the ends of all tracks as potential new vertices. We use the same tracking and anchoring method used for the muon track. After this search for secondary vertices, we search for tracks not associated with the reconstructed muon track. All remaining trackable and high ionizing clusters are used. The same track procedure is used, with a final cleanup step of splitting newly found tracks if appropriate.

5.6.5 Attenuation Correction

The size of the signal observed in a strip, given a specific energy deposit by a particle depends on the position along the strip where the particle interacted. The reason for this position dependence is the attenuation of light within the fiber WLS. For one single hit within a strip, the attenuation correction can not be performed because there is no way to know where along of the strip the hit was produced. However, once the tracks have been created, we know the three-dimensional position of the clusters that make up the track. In the early stages of processing, cluster energy is calibrated as if every cluster is in the center of the strip. For clusters that have three dimension information available, calculating and applying a correction differs from where the hit occurs in the middle of the strip in the longitudinal direction.

5.6.6 Incorporating MINOS Reconstruction

We attempt to match MINERνA tracks that have a cluster in at least one of the last five modules in the detector to tracks in MINOS. The resulting object is referred as a prong. To qualify as a match, the MINOS track must start within the first four planes of MINOS. We only consider matching MINOS and MINERνA tracks if they are within $200ns$ of each other.

We project the MINOS track across the two meters separating the two detectors to the plane that contains the last cluster on a MINERνA track, and, we project the MINERνA track to the plane that contains the vertex of the MINOS track. In MINERνA , we compare the position of the last cluster on a track with the projection of the MINOS track. We refer to the distance between these two points as the match residual. We also look at the analogous quantity in MINOS, If both match residuals are less than $40cm$, we consider them to be matching tracks.

If multiple potential matches exist, we take the match with the smallest match residual. We find that tracks matched to a MINOS track are almost exclusively muons giving a high level of confidence to our particle identification for such tracks.

5.6.7 Muon Energy Reconstruction

A MINOS track has a charge associated with it which is found by examining the direction of curvature in the MINOS magnetic field. We use the energy found by MINOS reconstruction. Energy can be found in one of two ways in MINOS. In one case, range of the track is used to estimate its initial energy. The curvature of the track in the magnetic field is also used to make an energy measurement. We use range or curvature for energy reconstruction depending upon where the track begins or ends. This includes whether the track passes into region containing non- instrumented planes, in which case we use curvature for reconstruction. If the track is contained within a particular volume that is fully instrumented, we use range for the momentum measurement. In all other cases, we use the result of the curvature measurement.

To find the energy of a muon in MINERνA, we must account for the energy lost by that muon as it travels in the MINERνA detector. To account for this energy loss, we use the Bethe-Bloch formula which gives the energy loss per distance travelled of charged particles,

$$-\frac{dE}{dx} = Kz^2\frac{Z}{A}\left[\frac{1}{2}ln\frac{2m_ec^2\beta^2\gamma^2T_{max}}{I^2} - \beta^2 - \frac{\delta(\beta\gamma)}{2}\right] \tag{5.7}$$

where K is a constant, z is the magnitude of the charge of the incident particle, A is the atomic mass, Z the atomic number, I is the mean excitation energy, m_e is the mass of the electron, $\delta(\beta\gamma)$ is a density effect correction to ionization energy loss, c is the speed of light, and we use the relativistic variables β and γ. T_{max} is the maximum amount of energy that can be imparted to an electron, given by

$$T_{max} = \frac{2m_ec^2\beta^2\gamma^2}{1 + \frac{2\gamma m_e}{M} + \frac{m_e^2}{M^2}} \tag{5.8}$$

where M is the mass of the particle for which T_{max} is being calculated. To apply this formula, we increment every step along a track assessing the amount and types of material along it.

5.6.8 Blob Reconstruction

Blobs are objects to define or store any group of clusters and are constructed to capture different types of topologies. We use blob objects to contain or reconstruct electromagnetic showers. In this thesis we reconstruct gammas, see Chapter 4 for full description. We also use the blob object to contain the activity around the event vertex, (Subsection 5.7.2). The blob energy is going to be a fundamental key to distinguish our $CC\pi^0$ inclusive and $CC\pi^0$ exclusive samples. All the energy deposited in our detector and not reconstructed by any method above described, is stored as another blob object called dispersed blob.

5.7 Event Selection and Reconstruction

This measurement has being performed on the active region of the MINERvA detector, particular attention must be paid to how the sample is defined. Our final-state interactions (FSI) are the key to split our different samples, considering we are selecting anti-neutrinos, our main signal or sample is dominated when the final state particles are 1 anti-muon and 1 π^0 have been produced.

According to our Monte Carlo, the final state particles distribute our events into four categories (figure 5.6), the first one is events where the particles in the final-state are 1 μ^+, 1 π^0 and 1 n. The second group is events that didn't belong to first group and contains 1 μ^+ and at least 1 π^0. The third group is events that contain π^0 coming from interaction in the detector. And the fourth group is events that there are no π^0's, most of them mis-reconstructed.

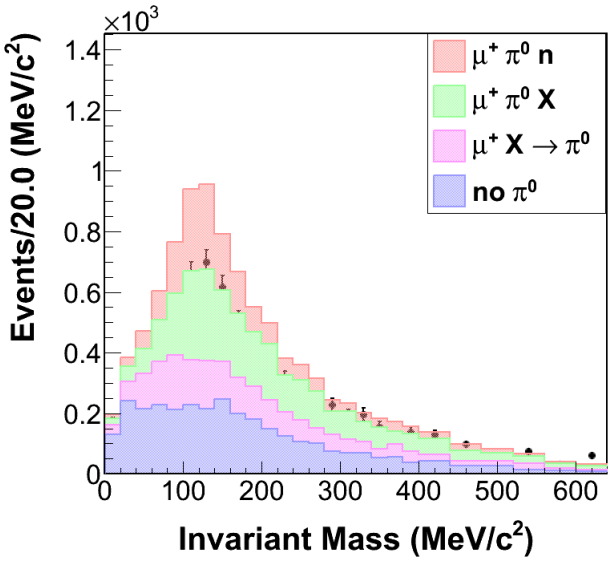

Figure 5.6: Stack Invariant mass version showing the 4 categories of our sample

Event Selection for Anti neutrino interactions:

- The basic criteria for selecting $\bar{\nu}$ events are MINERνA muon tracks, where the event vertex must be inside the "fiducial volume".
- We require a MINOS-matched track with positive curvature and a successful energy reconstruction, to select anti-muons.
- Hits to be reconstructed, must be within $25ns$ respect to vertex time.
- Muon vertex must be inside "fiducial volume".
- Showers must be reconstructed by Hough Transform if energy is bigger than 900 MeV or Angle Scan fails. Usually Hough Transform works for energetic π^0 and Angle scan for low energy π^0.
- 2 EM showers + Energy in Target Region $<$ 20 MeV.

We are trying to reconstruct π^0 in the final states. Our goal is to identify a neutral pion among other particles. We can think of cases where the topology is the simplest one and very complicated as it is the case of π^0 production in deep inelastic scattering. Our philosophy is to reconstruct events with simple topology where two photons decaying from π^0 are well defined and with no other particle overlapping them.

Following these concepts, we divided our signal in two categories, the first group there is μ^+, π^0 and any other particle(s) as final state particles ($CC\pi^0$ inclusive described in 5.7.3), and the second group where there are only these 3 final state particles μ^+, π^0 and n ($CC\pi^0$ exclusive described in 5.7.4).

We must split our data into the same categories described above but, using kinematic variables cuts. The first one is the invariant mass (description in Subsection 5.7.1) and the second one will be the energy around the vertex of interaction (description in Subsection 5.7.2).

5.7.1 Invariant Mass

The observables needed for the invariant mass analysis are two photon energies (E_{γ_1}, E_{γ_2}) and the opening angle $\theta_{\gamma\gamma}$ between them (equation 4.10), this invariant mass must be equivalent to the π^0 mass ($134.9MeV/c^2$) so we can assume the gammas are coming from the π^0. If the invariant mass is not close to the π^0 mass we may have fake electromagnetic showers or a wrong combination of gammas.

We plot the Invariant mass with the simple selection of 1 reconstructed anti-muon and 2 reconstructed γ's figures 5.7 and 5.8, we can observe the size of the sample that contains signal events and no signal events that passed our reconstruction and selection, called background. This Background has not the same invariant mass peak, at least for the group of No π^0's, the invariant mass for this group is kind of flat.

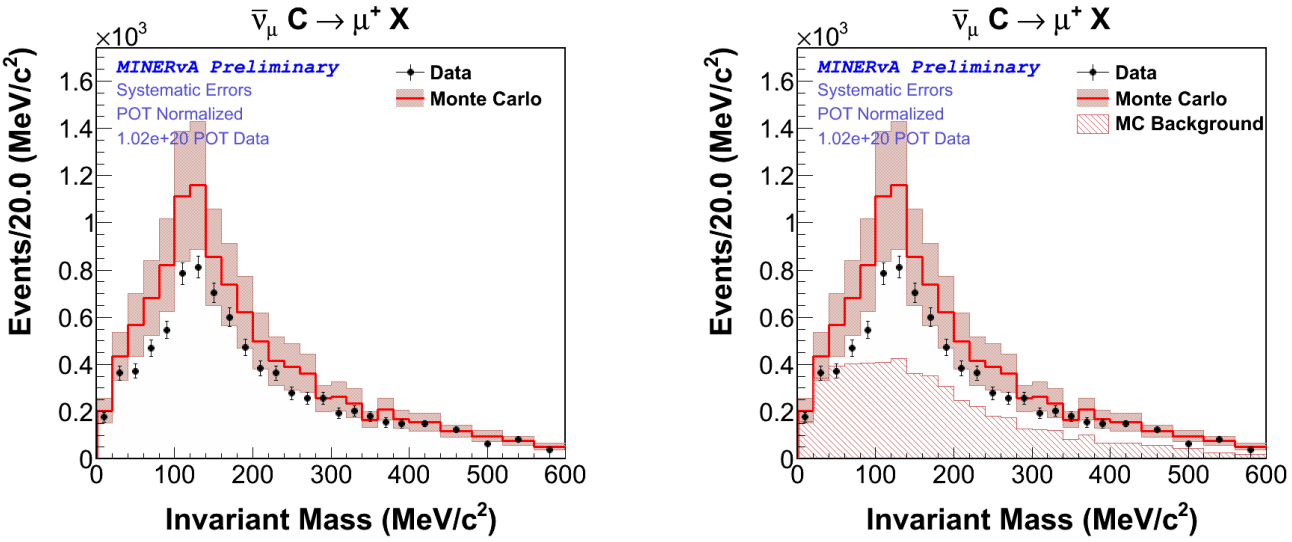

Figure 5.7: Left: invariant mass data and Monte Carlo comparisons. Right: invariant mass including background (background are events with π^0 coming from interaction in the detector and misreconstructed π^0 from events with no real π^0).

5.7.2 Energy Vertex

Energy vertex is the energy contained within a radius of 90 mm around the center in the event vertex . The event vertex, is well defined by the upstream position of the anti-muon trajectory. This variable provide us a strong evidence of extra activity coming from the ν-interaction.This variable is important to reduce the background for $CC\pi^0$ production.

Figures 5.9 and 5.10 show the distribution of the vertex energy where we observe huge peak around $0MeV$. Most of them correspond to the final state particles $\mu^+ n\pi^0$.

Each graph in this thesis has the same types of presentation:

- comparison between Monte Carlo and data.
- comparison between Monte Carlo and data including Monte Carlo background.
- ratio between Monte Carlo and data.

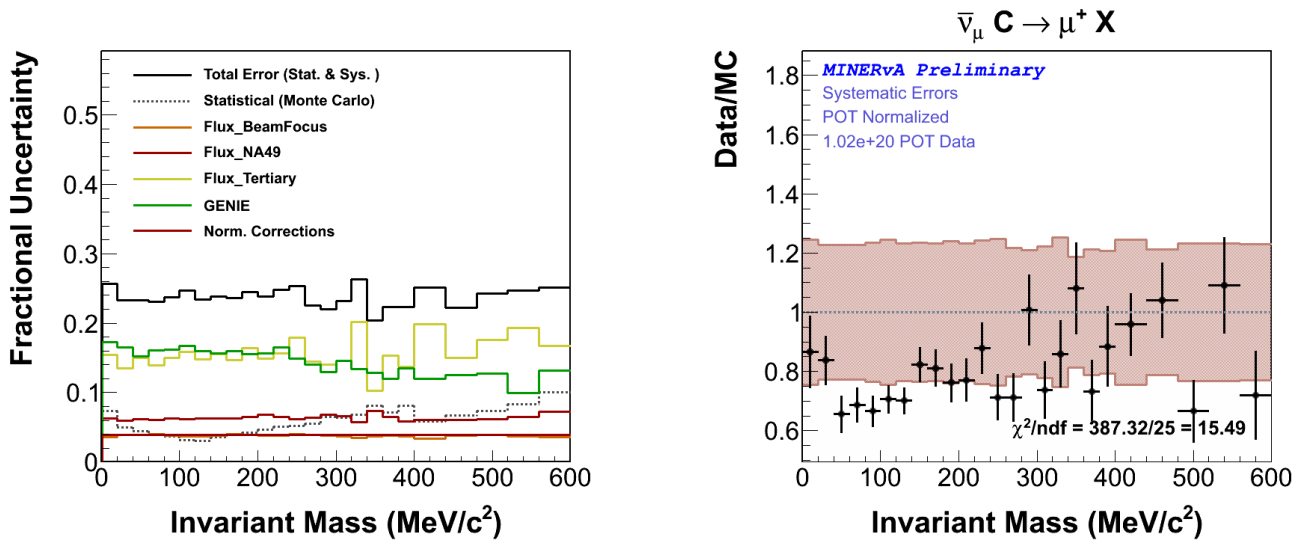

Figure 5.8: Left: Error summary plot for the invariant mass, where Y axis is fractional uncertainty. Right: Ratio between data and reconstructed Monte Carlo (sidebands are the systematic errors.

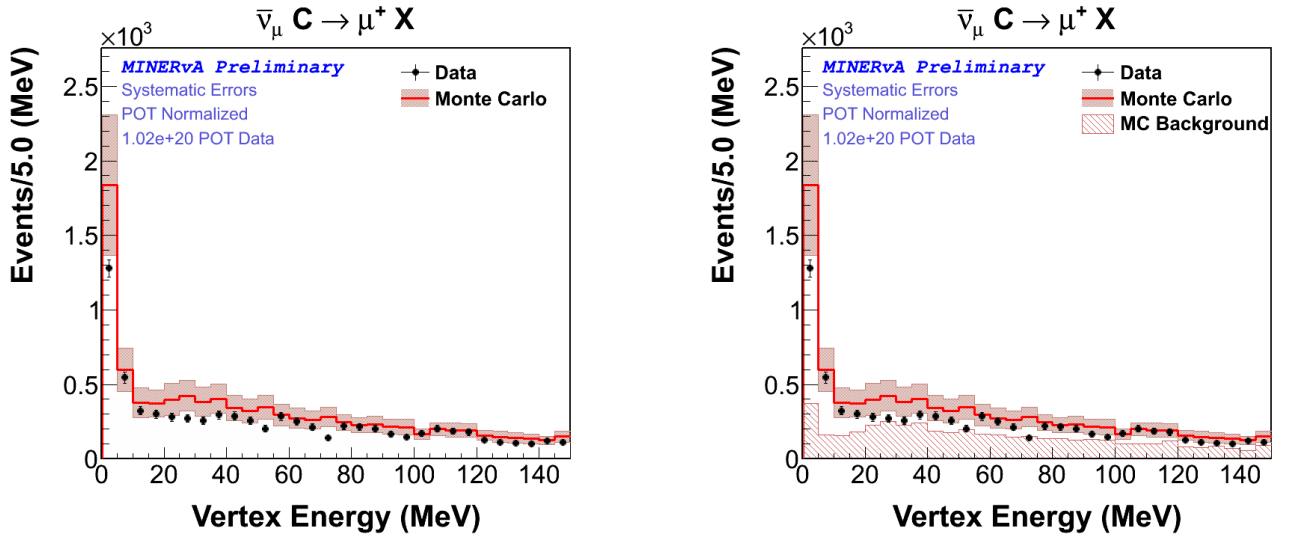

Figure 5.9: Left: Vertex Energy distribution, Data and Monte Carlo comparisons. Right: Vertex Energy plot including background, where Monte Carlo background are events with π^0 coming from interaction in the detector and events with mis-reconstruction, no π^0's

- systematic errors.
- stack plots.

It is not practical to show all these graphics in this thesis. They can be found in internet public area [95]. We include plots with both relative and absolute normalization.

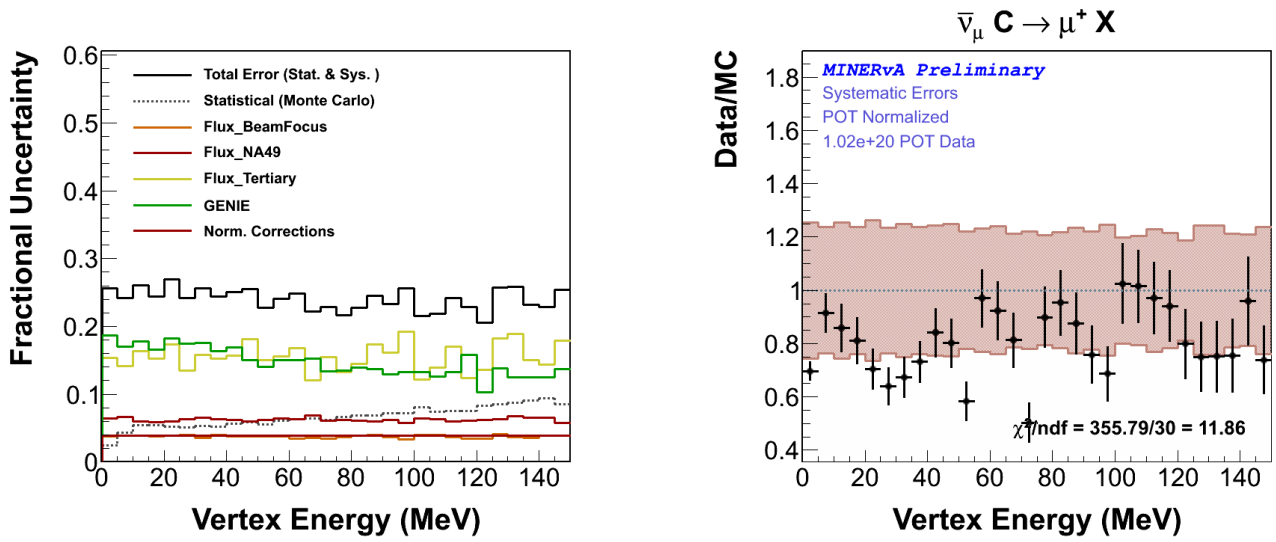

Figure 5.10: Left: Error summary plot for the vertex energy distribution, where Y axis is fractional uncertainty. Right: ratio between reconstructed data and Monte Carlo with absolute normalization (sidebands are the systematic errors).

5.7.3 CCπ^0 inclusive

We must, include all events containing one anti-muon, one π^0 and additional particles. Using our kinematic variables we make cuts on the invariant mass between 70 and 200MeV/c^2 as shown in figure 5.11 and on the vertex energy below 80 MeV as shown in figure 5.12 ensuring a sample with the purity greater than 62% on average.

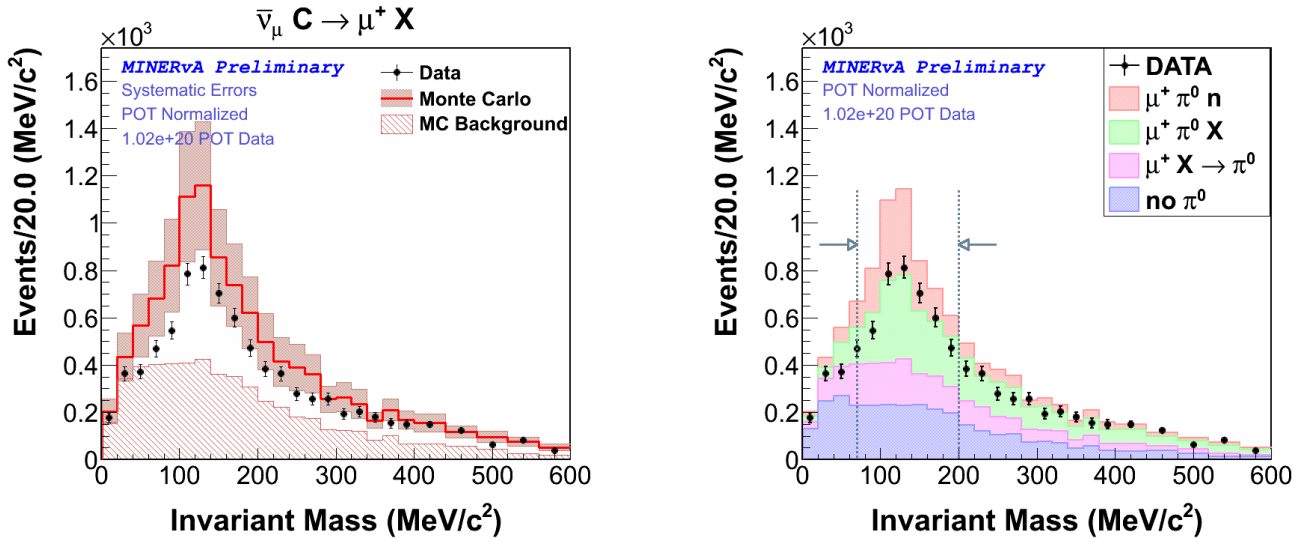

Figure 5.11: Invariant mass plot with stack histograms including our different categories, $CC\pi^0$ inclusive contains events with $\mu^+ n\pi^0$ (pink) and $\mu^+\pi^0 X$ (green) in the final state.

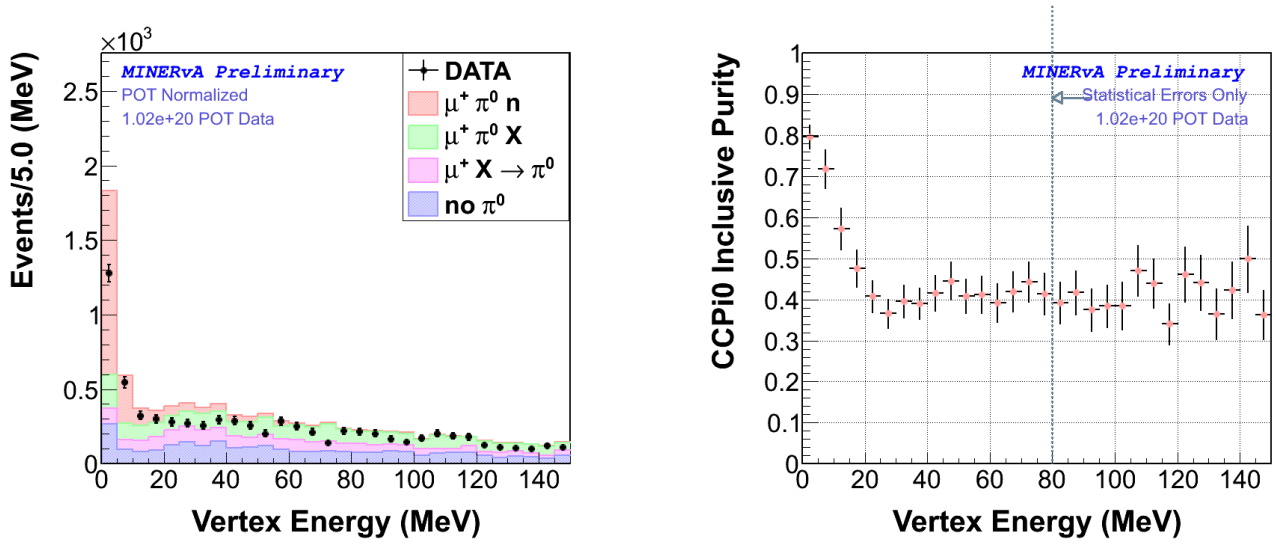

Figure 5.12: Left: Vertex Energy including our categories. Right: $CC\pi^0$ inclusive purity versus vertex energy dependence. We define a cut at vertex energy equals to $80MeV$

Table 5.1 shows the efficiency of $\sim 3\%$ and purity around 62% for $CC\pi^0$ inclusive. Several factors contribute for such poor efficiency mainly the requirement of a muon match with the MINOS near detector, that has an efficiency-acceptance around 50%.

Our algorithms attempt to reconstruct π^0 that well defined by the decay photons. In interactions with multiple particles in the final state such as $\mu^+\pi^0 X$ (table 5.1). The efficiency is only 1.7% and purity of 24%. In the case of a single final state, like $\mu^+ n\pi^0$, the efficiency is higher. Additional factors contribute to the poor efficiency, the combination of directions and energy of photons produced, the first photon can overlap with the second photon in one of the views of the detector, or one of them does not have enough energy to leave a trace in the detector, or the probability that one of the photons travel in a parallel direction to the anti-muon, and finally problems due to reconstruction algorithms, as they are not totally perfect.

5.7.4 $CC\pi^0$ exclusive

We demand that the final state particles must contain one anti-muon, one neutron and one π^0. This selection is made using information from the Monte Carlo, and cuts in kinematics variables. To isolate exclusive events we demand a vertex energy below $20MeV$, as ensuring at least a purity of 20% shown in figure 5.13. Background is greatly reduced as show in left plot in the figure 5.14. After this cut over vertex energy finally our $CC\pi^0$ exclusive sample is restricted to invariant mass region among 40 and $240MeV/c^2$ as shown in the right figure 5.14.

CCπ^0 INCLUSIVE			
FINAL STATES	EVENTS	PURITY	EFFICIENCY
$CC\pi^0$ inclusive	1775	62.5 %	3.2 %
$\mu^+\pi^0 n$	1087	38.3 %	6.9 %
$\mu^+\pi^0 X$	688	24.2 %	1.7 %
$\mu^+ X \rightarrow \pi^0$	502	17.7 %	1.7 %
no π^0	537	18.9 %	0.4 %

Table 5.1: Efficiency and Purity for $CC\pi^0$ inclusive with 70.0 MeV/c^2 <mass< 200.0 MeV/c^2

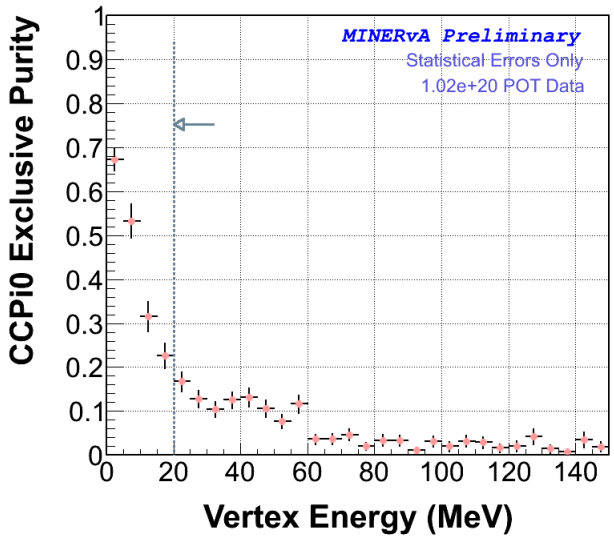

Figure 5.13: $CC\pi^0$ exclusive versus vertex energy

With these cuts we achieve an efficiency of 6.4% with purity of $\sim$ 63% as shown in table 5.2. The purity of every background component averages 10%. MINERνA can use the vertex energy to reduce the background. This variable tells us if there is a strong evidence of additional particles coming from the interaction. Other experiments can mis-reconstruct or mis-label inclusive events as simple ν-Induced Charged-Current π^0 production.

Figure 5.15 illustrates vertex energy helps to identify exclusive events. The top event display shows an event with two photons (red and green) and a vertex activity with more than $40MeV$. The vertex is inside the active region and is defined by the upstream position of the anti-muon (long track). The bottom event display shows an event with a long track (an anti muon) and two photons (red and green) and no energy around the vertex.

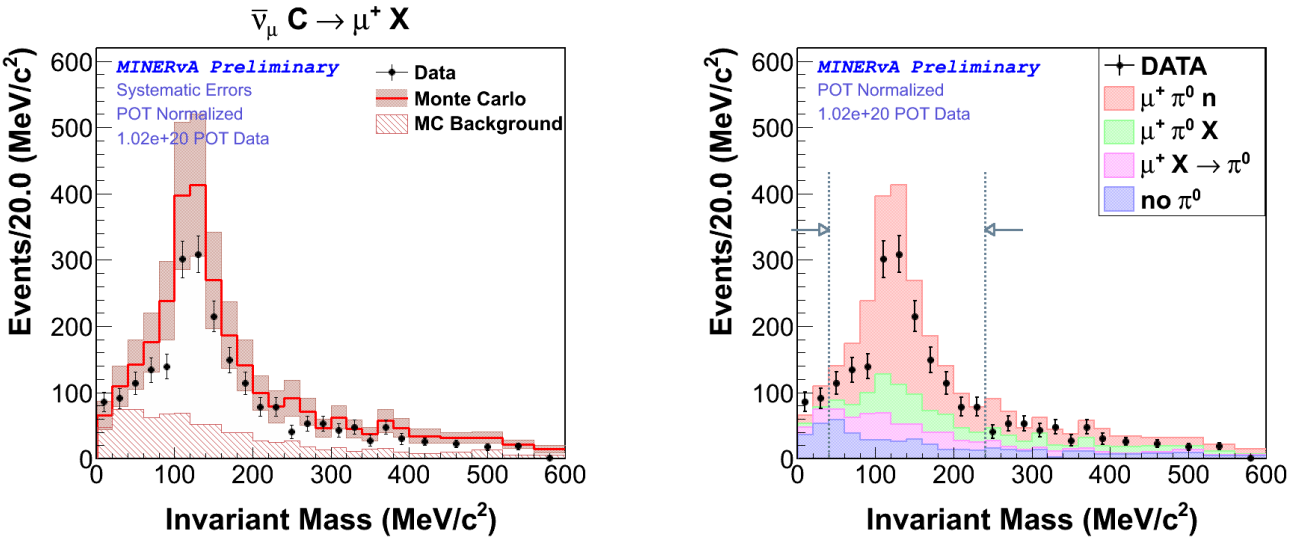

Figure 5.14: Left: invariant mass including Monte Carlo, its background and data. Right: invariant mass stack histograms including our different categories. $CC\pi^0$ exclusive contains events with $\mu^+ n\pi^0$ (pink) in the final state.

CCπ^0 EXCLUSIVE			
FINAL STATES	EVENTS	PURITY	EFFICIENCY
$\mu^+\pi^0 n$	1004	63.3 %	6.4 %
$\mu^+\pi^0 X$	223	14.1 %	0.6 %
$\mu^+ X \rightarrow \pi^0$	173	10.9 %	0.6 %
no π^0	183	11.5 %	0.1 %

Table 5.2: Efficiency and purity for $CC\pi^0$ exclusive with 40.0 MeV/c^2 <mass< 240.0 MeV/c^2 and E_{vertex}< 20 MeV

5.8 Reconstructed Variables

In this section we describe some important variables and compare the shape of the distributions of reconstructed data with reconstructed Monte Carlo. Plots are relative normalized.

A complete reconstruction of our events requires several key variables related to the muon (such as direction and energy) and to the $\pi 0$ (such as the energy of the photons and the angle between their directions).

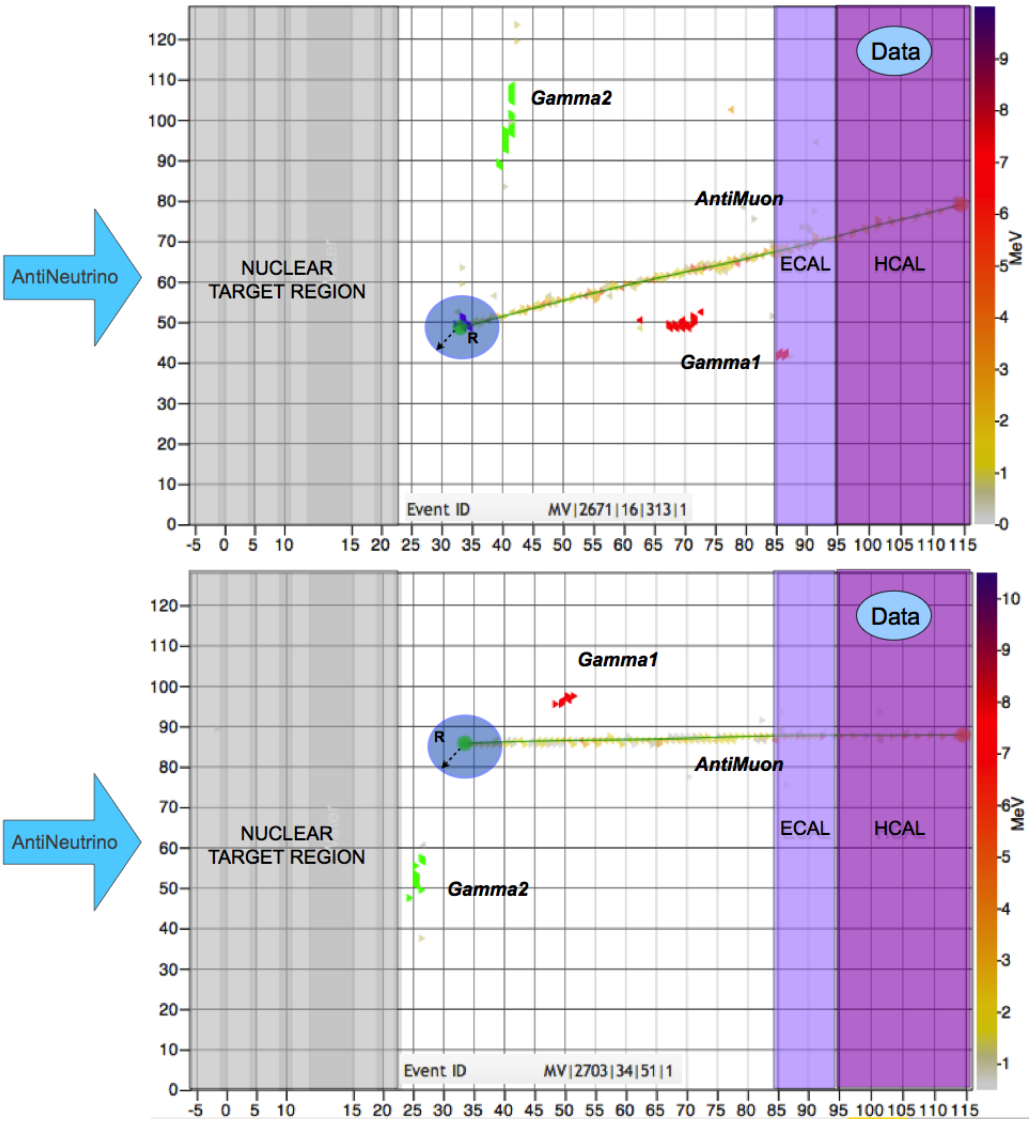

Figure 5.15: Top:Event display showing $CC\pi^0$ inclusive candidate from data. The red photon is the energetic one, the second photon (less energetic) is shown in green. The long track is the anti-muon and the dark hits inside the circle around the vertex account for the vertex energy. In this event we have $E_{vertex} = 128.37$ MeV, $M = 139.47$ MeV/c^2, $E_{\gamma_1} = 132.05$ MeV, $E\gamma_2 = 127.40$ MeV. Bottom: Event display showing $CC\pi^0$ exclusive candidate from data. $E_{vertex} = 0$ MeV (there is no activity around the vertex), $M = 130.88$ MeV/c^2, $E_{\gamma_1} = 164.32$ MeV and $E_{\gamma_2} = 155.12$ MeV.

5.8.1 Kinematics Distribution for $CC\pi^0$ inclusive

As a check of our reconstruction methods we compare data and Monte Carlo distributions for every reconstructed variable.

The same algorithms are used for $CC\pi^0$ inclusive and for $CC\pi^0$ exclusive. The goal is to identify and reconstruct a single π^0. It is important to see how the reconstructed energy of the energetic γ (γ_1) compares for data and Monte Carlo[2]. Figure 5.16 shows that our algorithm reconstructs the energetic γ with a mean energy of $\sim 200MeV$.

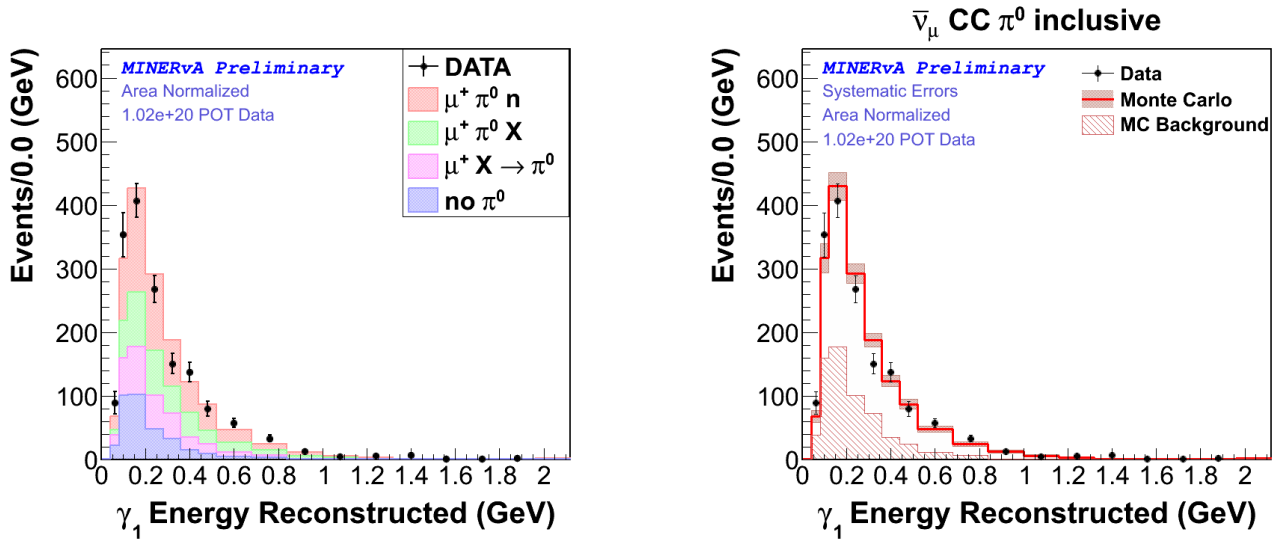

Figure 5.16: Left: γ_1 energy distribution, data and Monte Carlo. Stack plot includes all our categories. Right: γ_1 energy distribution, data and Monte Carlo (Monte Carlo background included).

Figure 5.17 shows the distribution of $(E_{\gamma_1} - E_{\gamma_2})$ / $(E_{\gamma_1} + E_{\gamma_2})$ that quantifies the asymmetry between the photons coming from the π^0 decay. Only a small percentage of events has one of the photons getting most of the energy of the π^0.

Figure 5.18 show the π^0 momentum distribution. It peaks around $\sim 300MeV$ and decreases fast as the momentum increases. Very few events are reconstructed with energetic π^0.

Figure 5.19 shows the distribution of the opening angle between gammas. Most π^0 are reconstructed when opening angle is small.

MiniBooNE experiment reported an observation of more events than predicted by Monte Carlo when $cos\theta_{\pi^0}$ is close to one[3]. Our distribution of $cos\theta_{\pi^0}$, as shown in figure 5.20, does not show this effect. One should notice that MiniBooNE uses the NUANCE Monte Carlo while we use GENIE. The effect is not observed even when we weight $cos\theta_{\pi 0}$ by the π^0 energy as we shown in figure 5.21.

When we are reconstructing the long tracks in order to find muons, leptons are used to indirectly determine whether there was an charged current interaction of a neutrino in the detector. This track must be originated in the center of the detector, and head into MINOS

[2]See section 4.4 for a detailed description of how we reconstruct the energy of a given electromagnetic shower.
[3]$cos\theta_{\pi 0}$ is the angle between the direction of π^0 and the direction of the interacting neutrino.

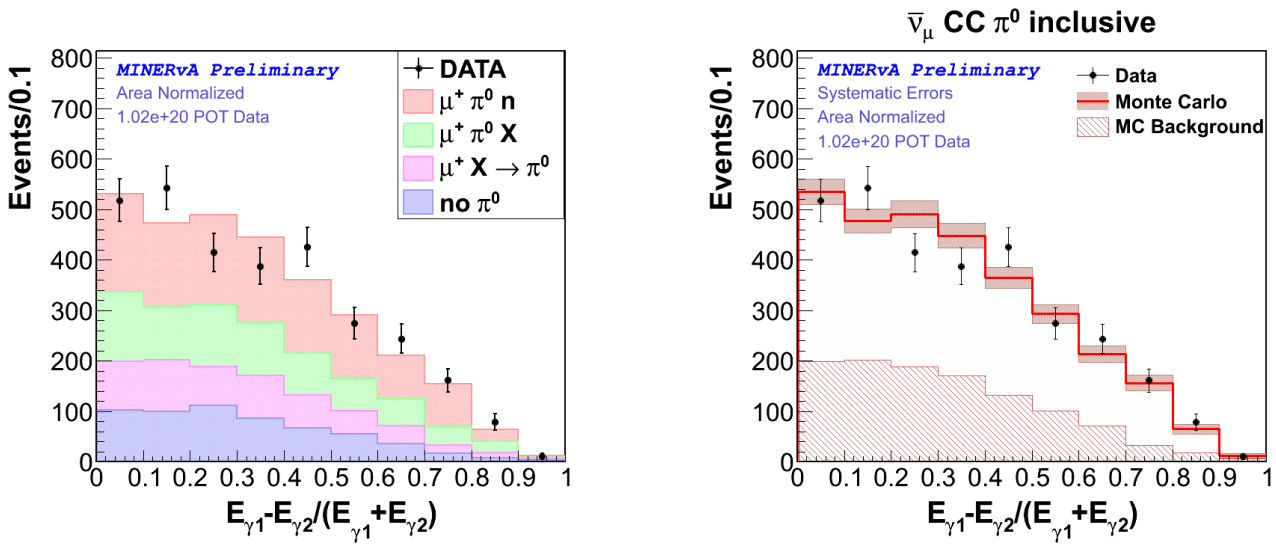

Figure 5.17: Left: $(E_{\gamma_1} - E_{\gamma_2})$ / $(E_{\gamma_1} + E_{\gamma_2})$, data and Monte Carlo. Right: $(E_{\gamma_1} - E_{\gamma_2})$ / $(E_{\gamma_1} + E_{\gamma_2})$, data and Monte Carlo. Monte Carlo Background for $CC\pi^0$ inclusive is included.

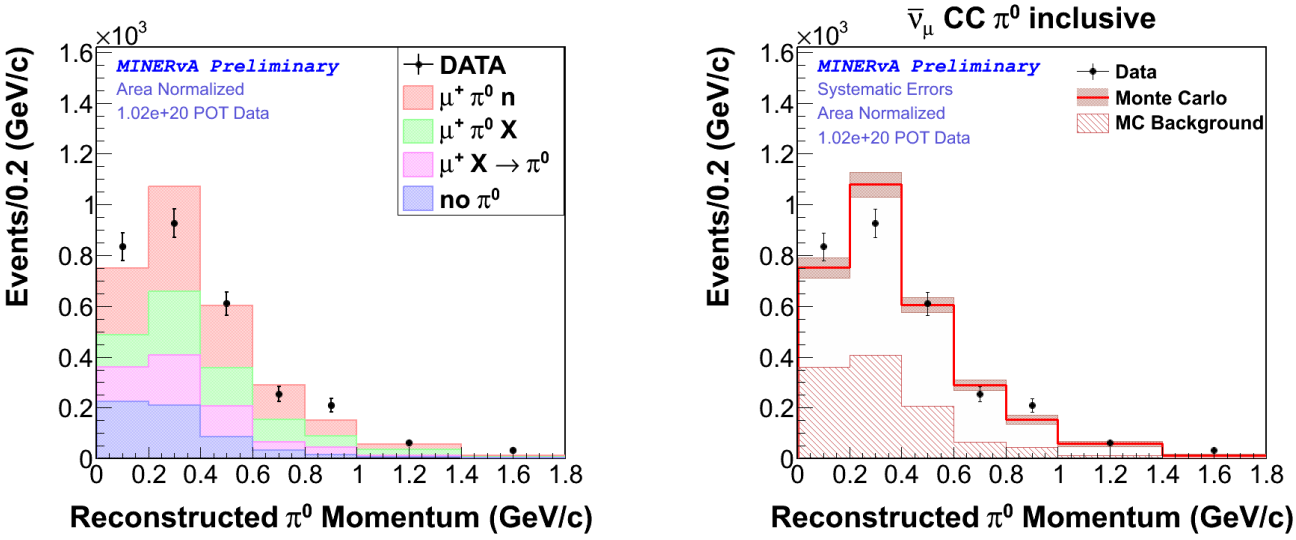

Figure 5.18: Left: reconstructed π^0 momentum. Data and Monte Carlo stack plot for $CC\pi^0$ inclusive. Right: reconstructed π^0 momentum including Monte Carlo background.

detector to complete the reconstruction of the muon energy. It is important showing the relationship between Data and Monte Carlo, the energy and direction of the muon.

Muon momentum is very important for the reconstruction of any charged current neutrino interaction. Usually a big percentage of the neutrino energy is carried by the muon. Figure

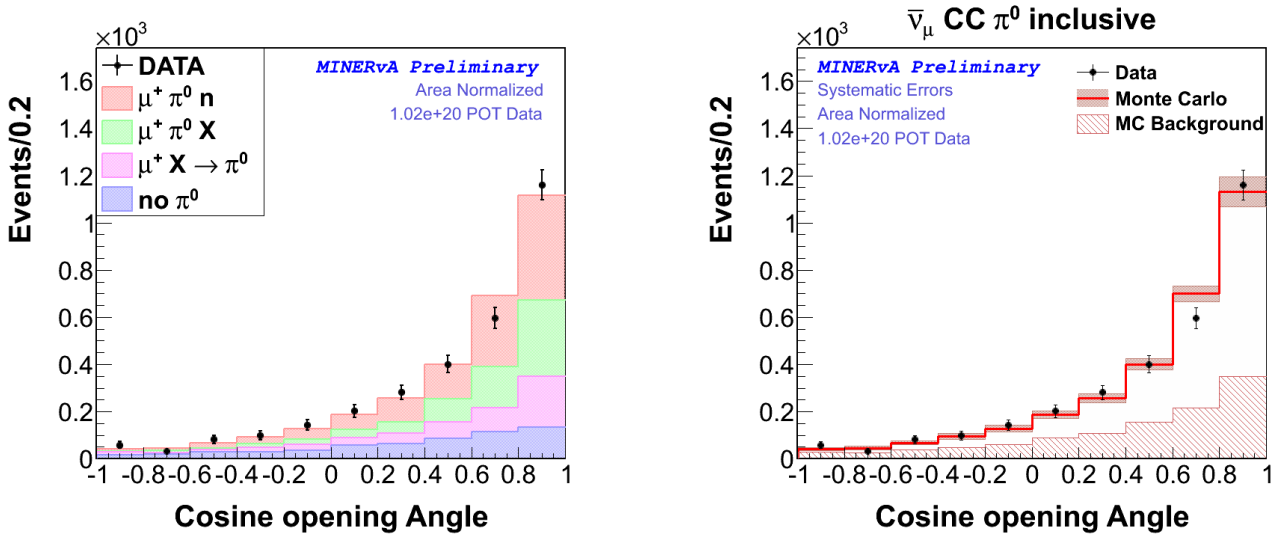

Figure 5.19: Left:Cosine of opening angle between gammas, data and Monte Carlo, stack plot for $CC\pi^0$ inclusive. Right: Cosine of opening angle between gammas including Monte Carlo background.

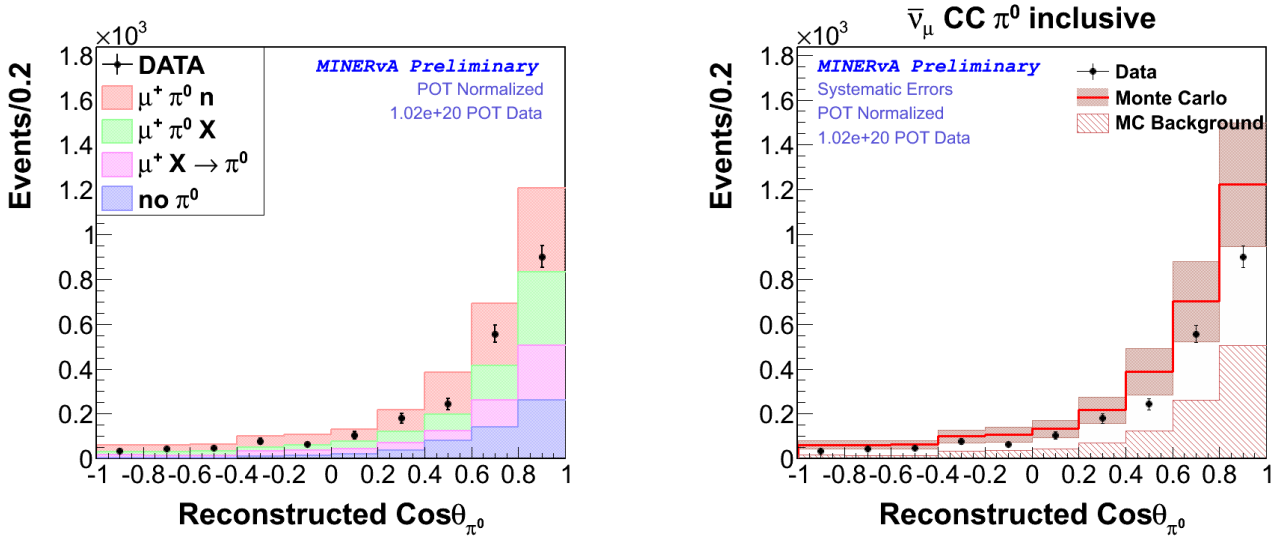

Figure 5.20: Left: cosine opening angle between π^0 and $\bar{\nu}_\mu$ direction, data and Monte Carlo, stack plot for $CC\pi^0$ inclusive. Right: cosine opening angle between π^0 and $\bar{\nu}_\mu$ direction including Monte Carlo Background. Both plots are absolute normalized to compensate for the difference between the number of entries in data and Monte Carlo.

5.22 shows the muon momentum distribution. We demand the muon energy above $1.5GeV$[4].

θ_μ and ϕ_μ are important variables for the reconstruction of Q^2 and the neutrino energy. Figures 5.23 and 5.24 show the distribution of these variables.

[4]energetic muons are able to reach the Minos Detector and have good acceptance

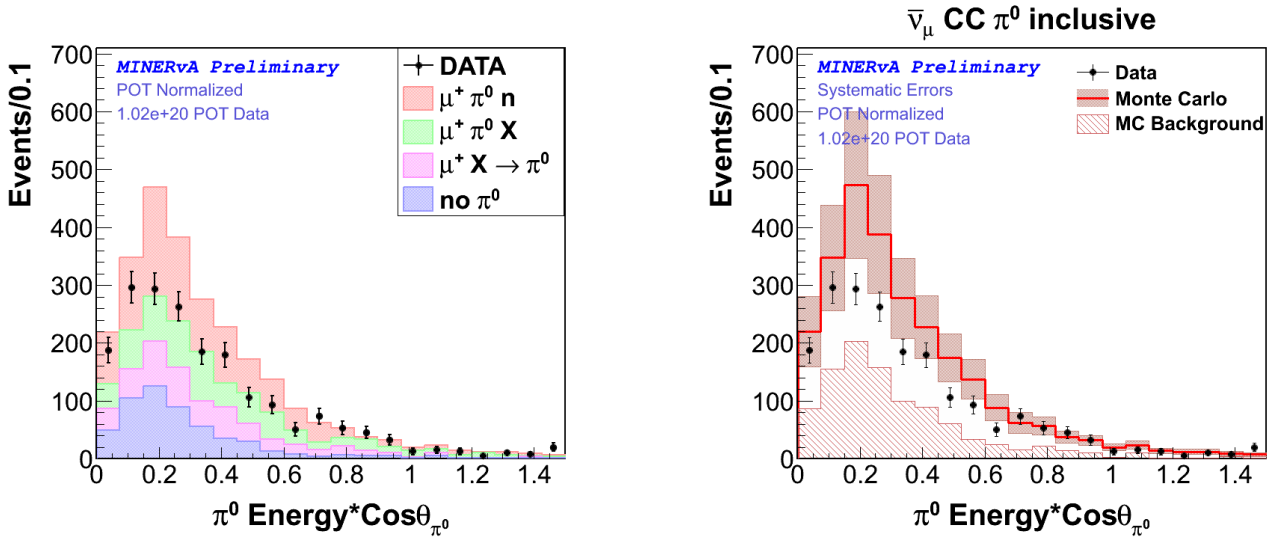

Figure 5.21: Left: $E_{\pi^0} \times cos\pi^0$, data and Monte Carlo, stack plot. Right: $E_{\pi^0} \times cos\pi^0$ including Monte Carlo Background for $CC\pi^0$ inclusive. Both plots are absolute normalized to compensate for the difference between the number entries in data and Monte Carlo.

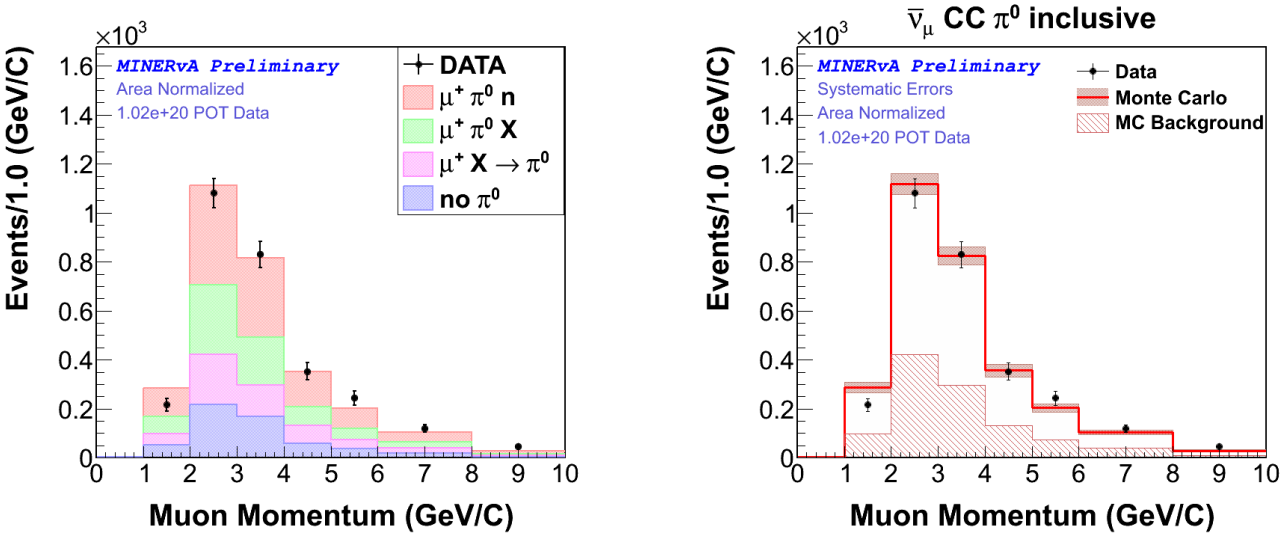

Figure 5.22: Left: muon momentum distribution, data and Monte Carlo, stack plot for $CC\pi^0$ inclusive. Rigth: Muon momentum distribution including Monte Carlo Background

$E_{\bar{\nu}_\mu}$ is calculated using the approximation given by equation 2.32

Q^2 is calculated using the neutrino energy and the muon energy-direction reconstructed, expressed on equation2.34. Figure 5.26 shows the Q^2 distribution.

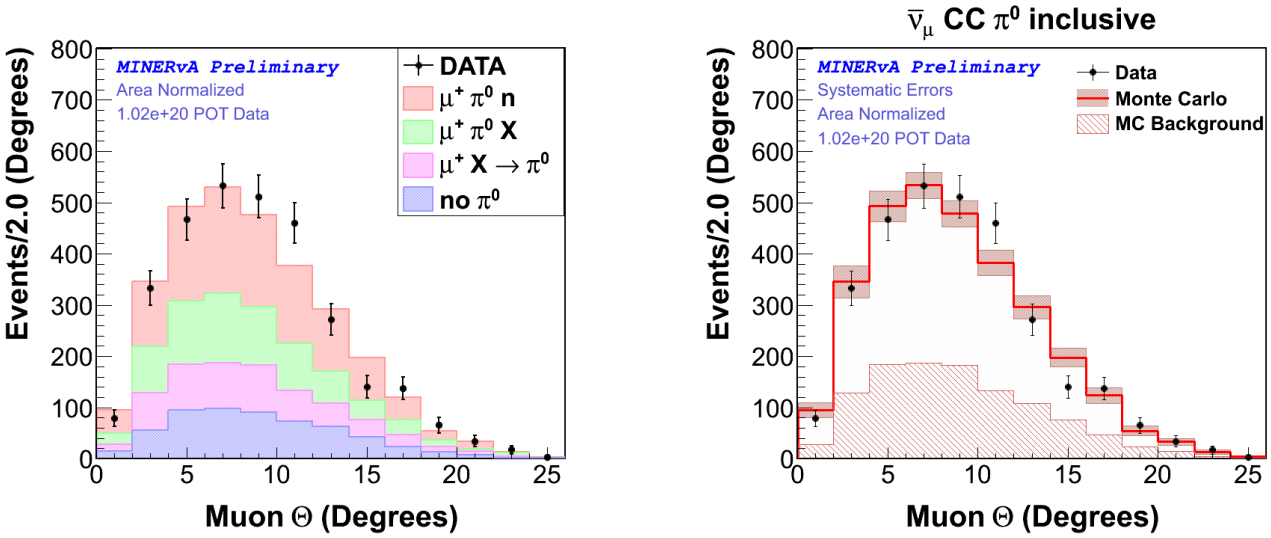

Figure 5.23: Left: θ angle of the muon direction, data and Monte Carlo, stack plot. Right: θ angle of the muon direction including Monte Carlo background for $CC\pi^0$ inclusive.

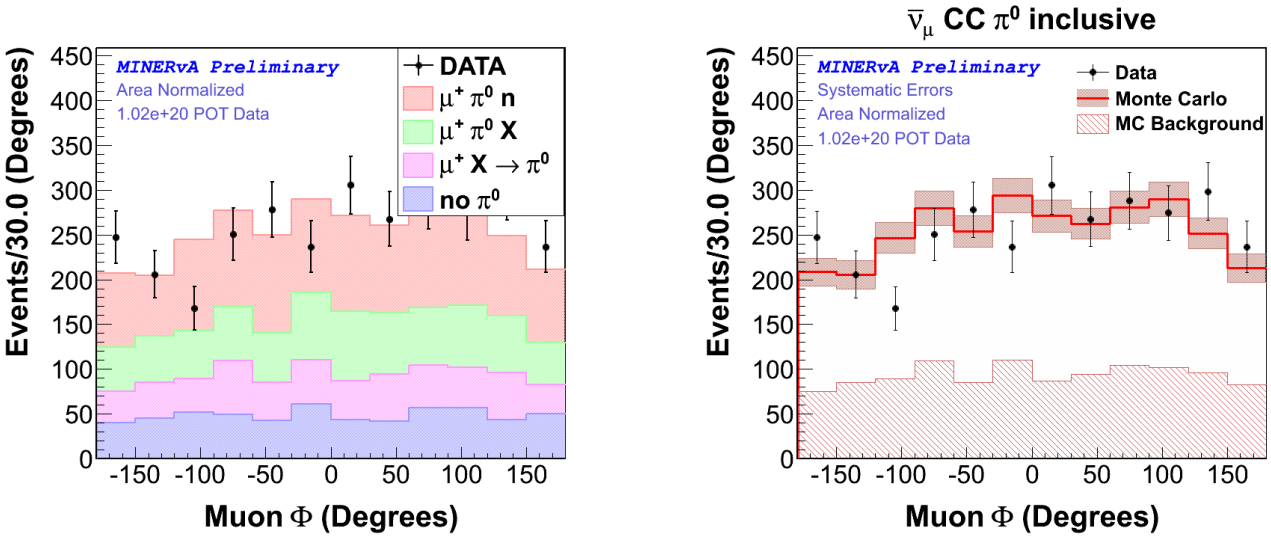

Figure 5.24: Left: ϕ angle of the muon direction, data and Monte Carlo, stack plot. Right: ϕ angle of the muon direction including Monte Carlo background for $CC\pi^0$ inclusive

5.8.2 Kinematics Distribution for $CC\pi^0$ exclusive

We are using the same set of plots showed on the previous subsection. $CC\pi^0$ exclusive has less statistics than $CC\pi^0$ inclusive[5], our distributions show bigger statistical fluctuations.

Gamma energy distribution for the energetic gamma is shown on figure 5.27.

[5]the cross-section for exclusive is small with respect to inclusive π^0 production

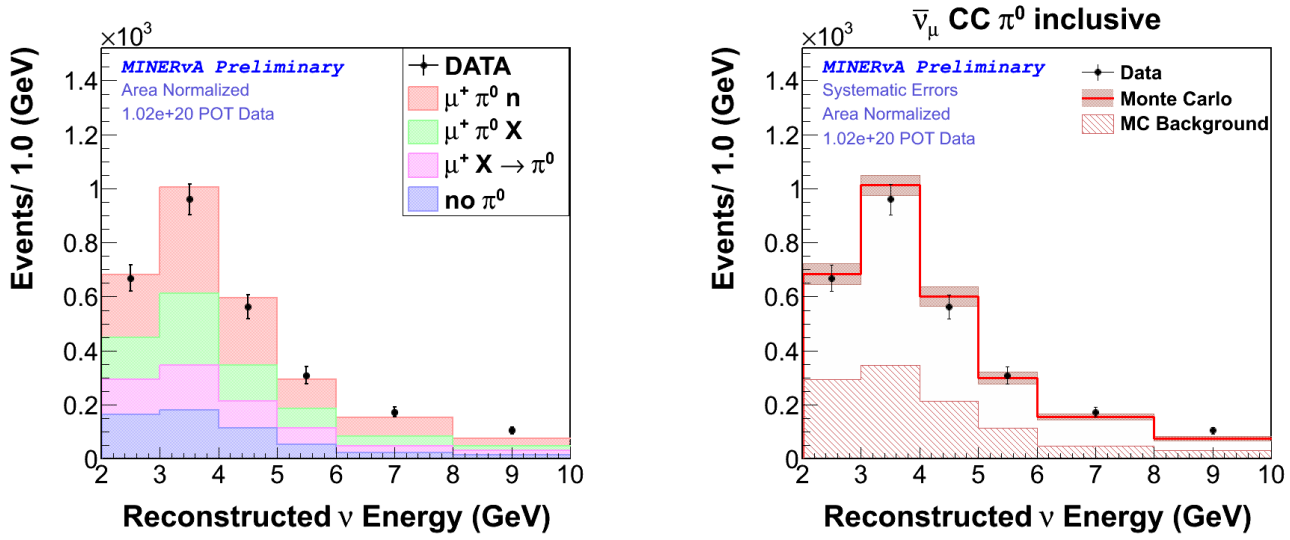

Figure 5.25: Left: $E_{\bar{\nu}_\mu}$ for $CC\pi^0$ inclusive, data and Monte Carlo, relative normalize, stack plot. Right: $E_{\bar{\nu}_\mu}$i for $CC\pi^0$ inclusive including Monte Carlo background.

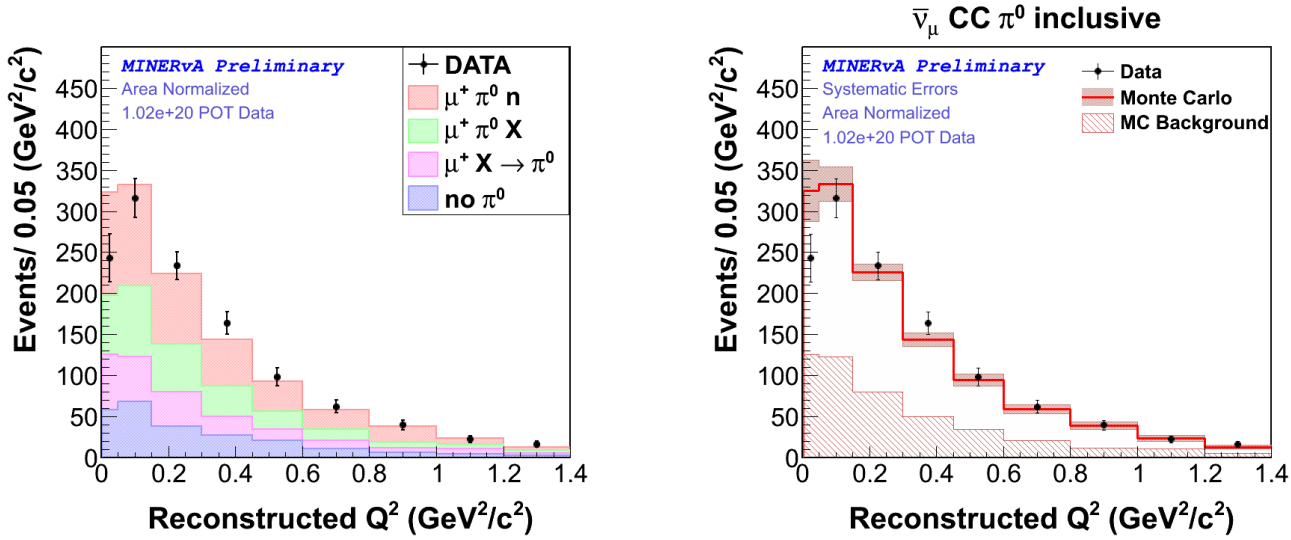

Figure 5.26: Left: Q^2 for $CC\pi^0$ inclusive, data and Monte Carlo, relative normalize, stack plot. Right: Q^2 for $CC\pi^0$ inclusive, including Monte Carlo Background

Figure 5.28 shows the asymmetry between the two decay gammas.This plot is showing in average, how the π^0 energy is distributed between the gammas.

For $CC\pi^0$ exclusive the π^0 momentum shows high purity of the signal defined by the final state particles $\mu^+ n\pi^0$. The reconstructed rate events are, again, low for events where the reconstructed π^0 momentum is bigger than $1GeV$, as shown in figure 5.29

Figure 5.30 shows the cosine of the opening angle between γ_1 and γ_2. A high percentage of events reconstructed have a small opening angle.

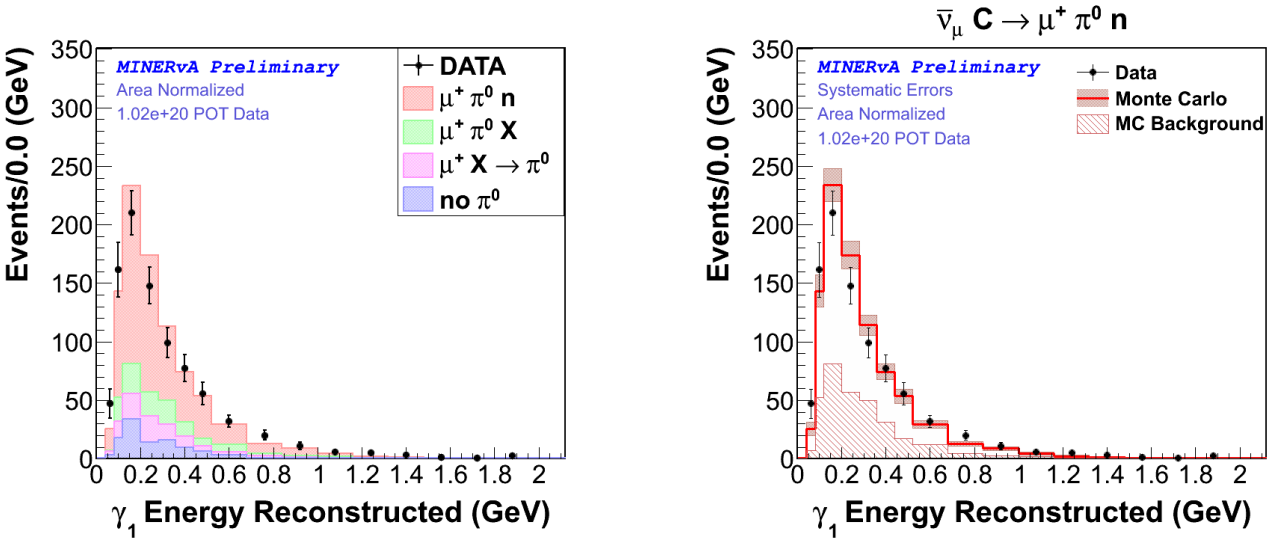

Figure 5.27: Left: E_{γ_1}, data and Monte Carlo, stack plot including our categories. Right: E_{γ_1}, data and Monte Carlo including Monte Carlo background

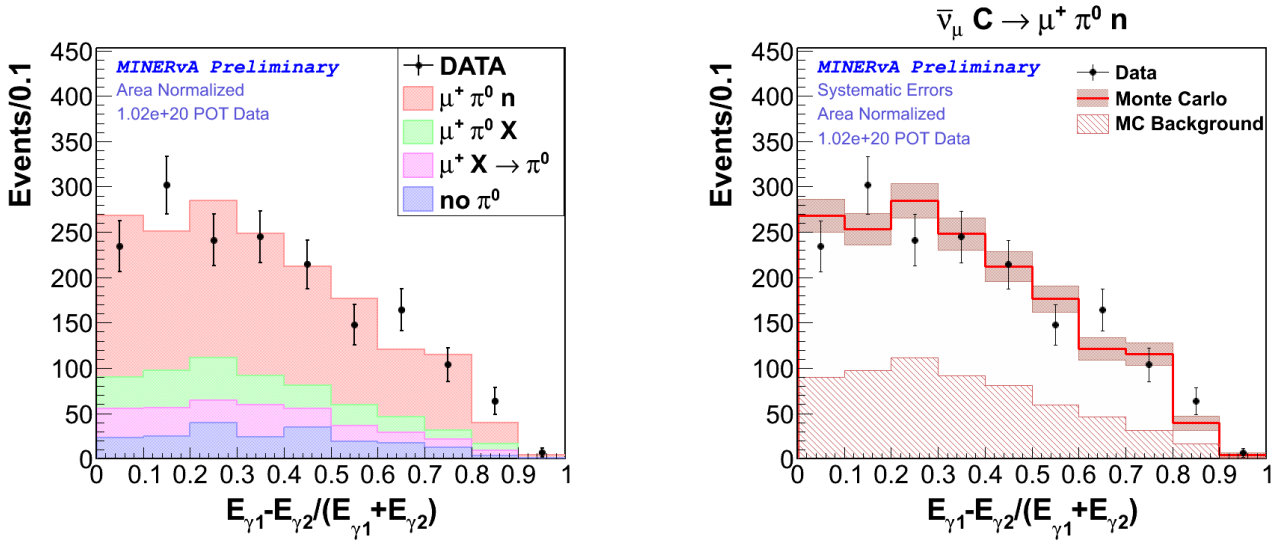

Figure 5.28: Left: $(E_{\gamma_1} - E_{\gamma_2})$ / $(E_{\gamma_1} + E_{\gamma_2})$, data and Monte Carlo. Right: $(E_{\gamma_1} - E_{\gamma_2})$ / $(E_{\gamma_1} + E_{\gamma_2})$, data and Monte Carlo. including Monte Carlo Background for $CC\pi^0$ exclusive.

The excess production for a small θ_{π^0} reported by MiniBooNE [56], is not observed even when the $\cos\theta_{\pi^0}$ is weighted by the π^0 energy, as we can see in figures 5.31 and 5.32.

Figures 5.33, 5.34 and 5.35 show the distribution of the muon momentum, θ and ϕ.

Our reconstructed neutrino energy distribution include cut over $2GeV$, because we already have applied a cut on muon energy distribution above $1.5GeV$. We follow the same assumption given in Section 2.6.5.

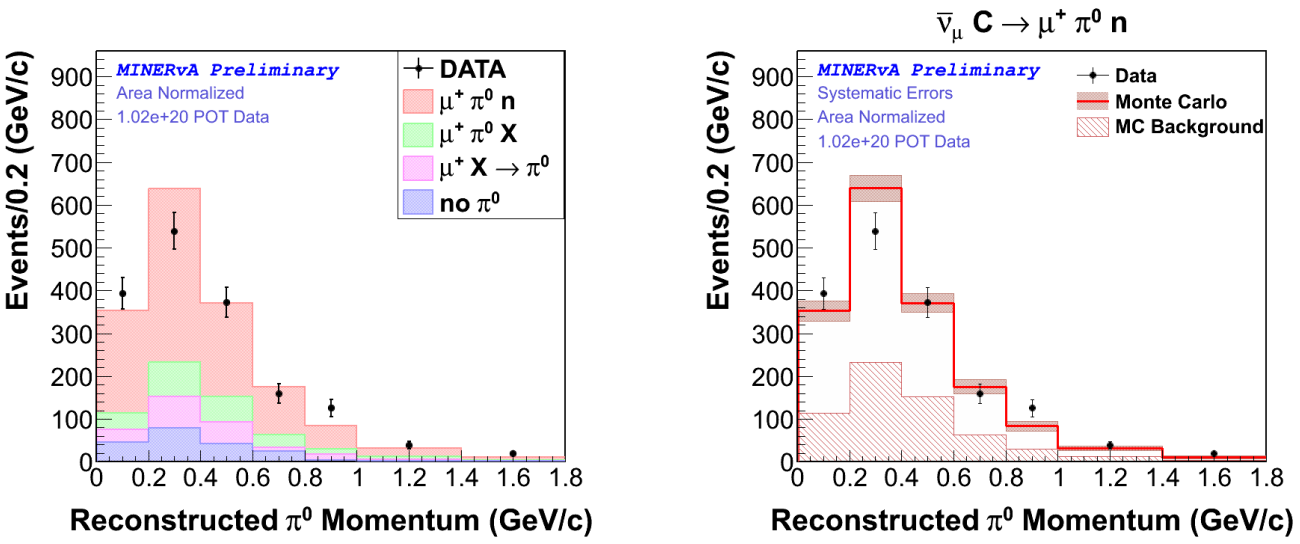

Figure 5.29: Left: reconstructed π^0 momentum, data and Monte Carlo, stack plot for $CC\pi^0$ exclusive. Right: reconstructed π^0 momentum including Monte Carlo Background.

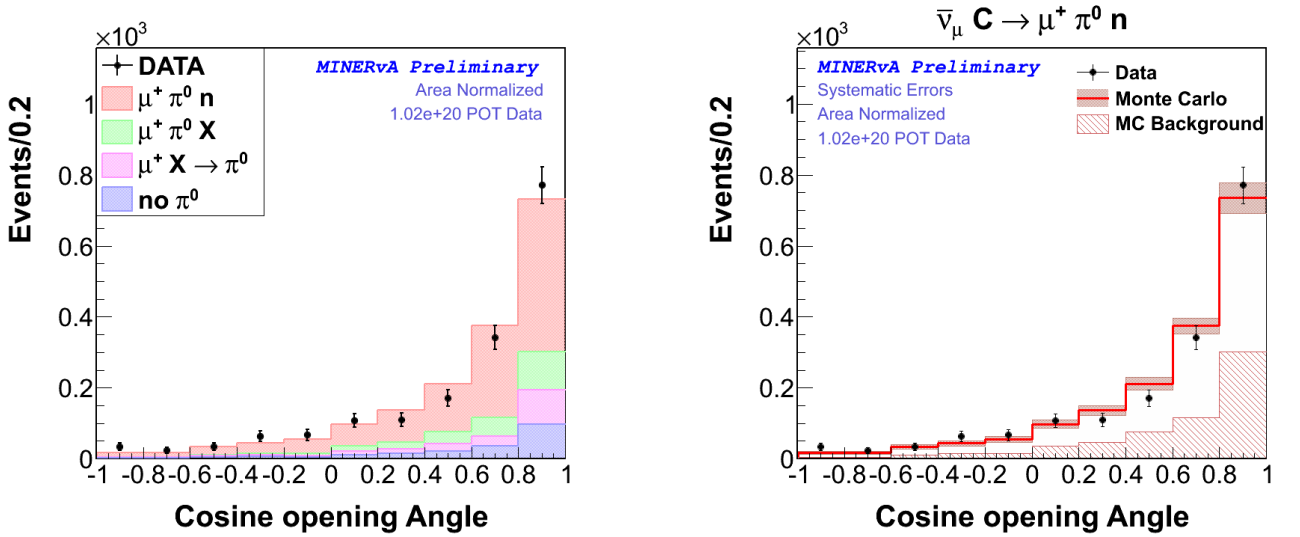

Figure 5.30: Left:Cosine of opening angle between γ_1 and γ_2, data and Monte Carlo, stack plot for $CC\pi^0$ exclusive. Right: Cosine of opening angle between γ_1 and γ_2 including Monte Carlo background.

Equation 2.34 is used for the calculation of Q^2 whose distribution is shown in figure 5.37.

5.8.3 Summary

This chapter shows that we are able to reconstruct π^0 events in MINERνA with good agreement between Data and Monte Carlo. All distributions in this chapter represent every

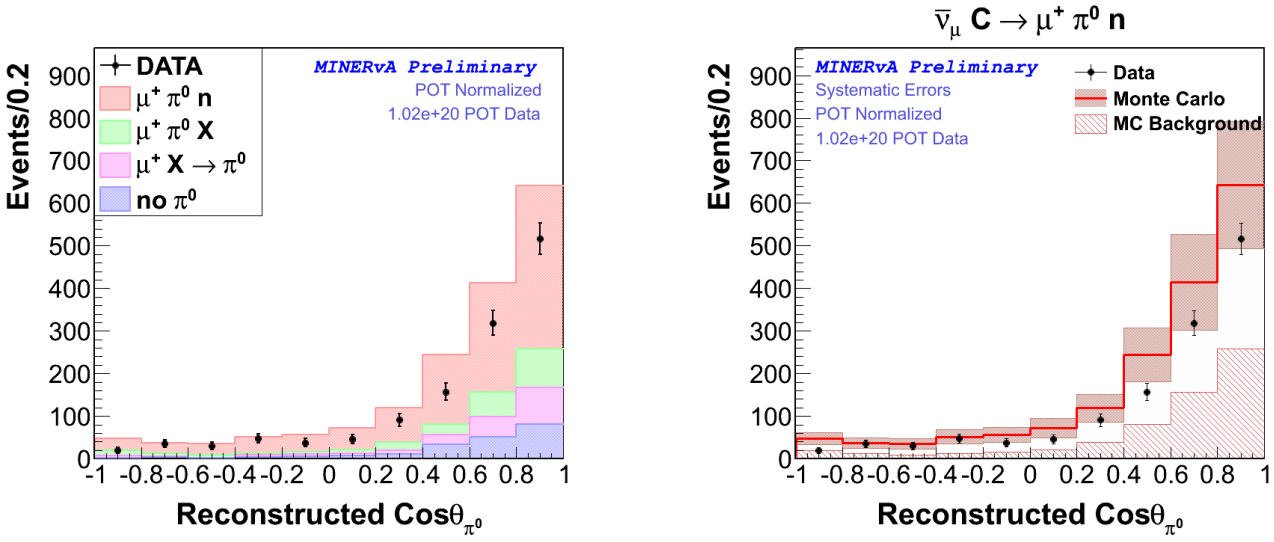

Figure 5.31: Left: Cosine opening angle between π^0 and $\bar{\nu}_\mu$ direction, data and Monte Carlo, stack plot for $CC\pi^0$ exclusive. Right: Cosine opening angle between π^0 and $\bar{\nu}_\mu$ direction , including Monte Carlo background.

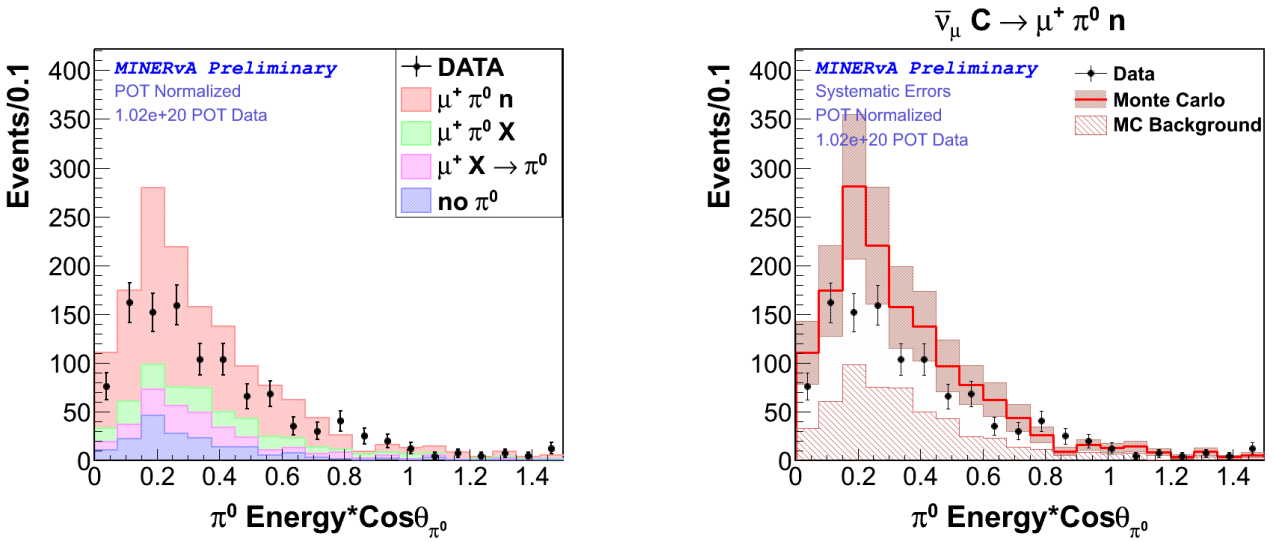

Figure 5.32: Left: $E_{\pi^0} \times cos\pi^0$, data and Monte Carlo, stack plot. Right: $E_{\pi^0} \times cos\pi^0$ including Monte Carlo Background for $CC\pi^0$ exclusive.

step in our reconstruction: muon energy, muon direction, π^0 momentum, Q^2 and Neutrino Energy.

These plots were shape compared, showing good agreement between Data and Monte Carlo. In the next chapter we use our reconstructed sample to calculate the cross section for $CC\pi^0$ inclusive and $CC\pi^0$ exclusive.

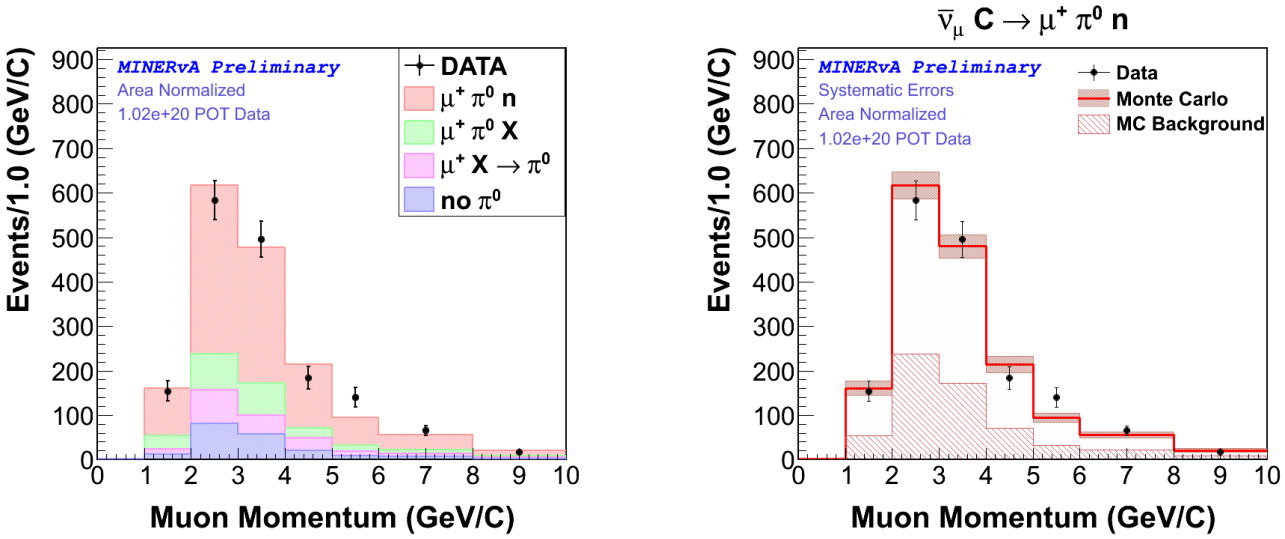

Figure 5.33: Left: muon momentum , data and Monte Carlo, stack plot for $CC\pi^0$ exclusive. Right: muon momentum including Monte Carlo background.

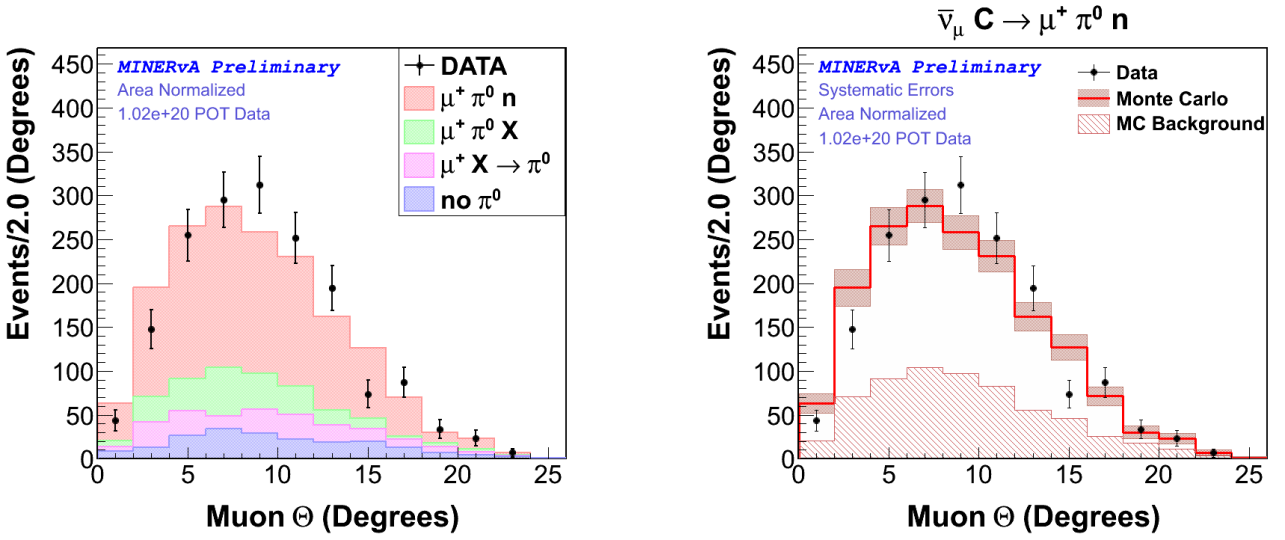

Figure 5.34: Left: θ angle of the muon direction, data and Monte Carlo, stack plot. Right: θ angle of the muon direction including Monte Carlo Background for $CC\pi^0$ exclusive

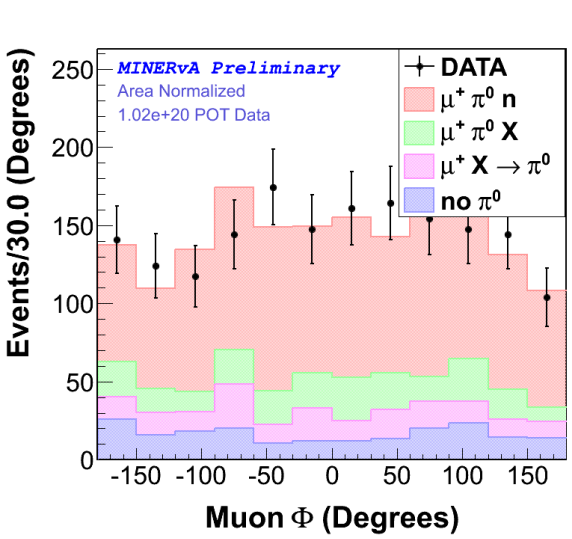

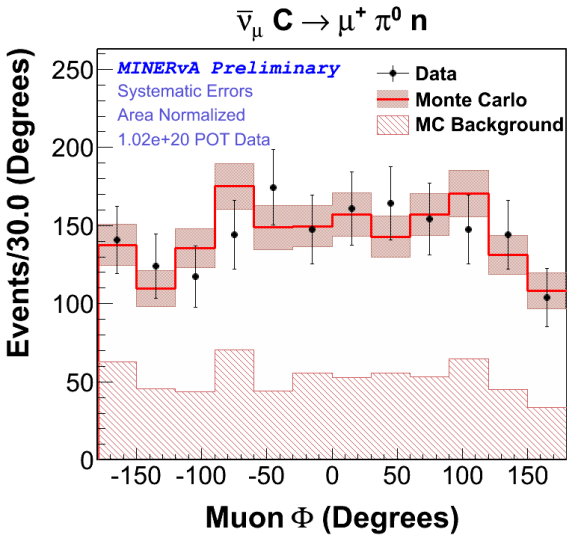

Figure 5.35: Left: ϕ angle of the muon direction, data and Monte Carlo, stack plot. Right: ϕ angle of the muon direction including Monte Carlo background for $CC\pi^0$ exclusive.

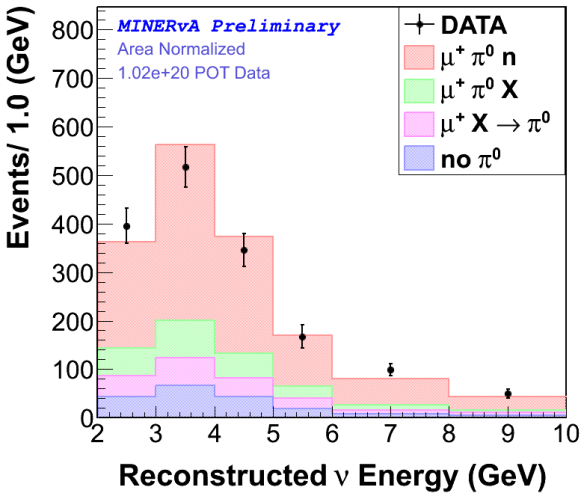

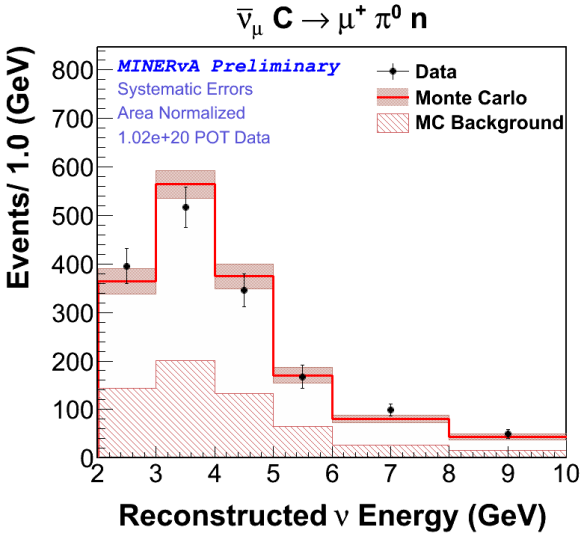

Figure 5.36: Left: $E_{\bar{\nu}_\mu}$ for $CC\pi^0$ inclusive, data and Monte Carlo, relative normalize, stack plot. Right: $E_{\bar{\nu}_\mu}$ for $CC\pi^0$ exclusive including Monte Carlo background.

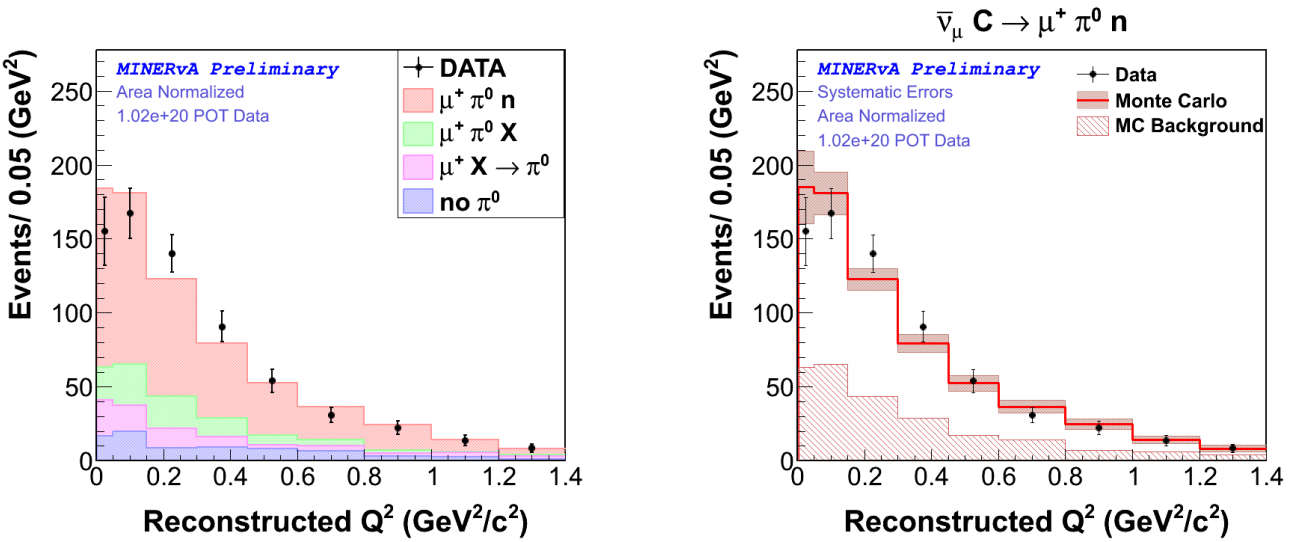

Figure 5.37: Left: Q^2 for $CC\pi^0$ inclusive, data and Monte Carlo, relative normalize, stack plot. Right: Q^2 for $CC\pi^0$ exclusive including Monte Carlo background.

Chapter 6

Measuring the Differential Cross Sections for $CC\pi^0$

6.1 Introduction

The reconstruction of observable cross section for $CC\pi^0$ inclusive and $CC\pi^0$ exclusive samples was done in several steps.

- **Background subtraction**: our reconstructed sample is contaminated by non-signal events (background) and does not fully contain all signal events.
- **Unfolding**: the reconstructed variables usually are deviated from their true value. We need to redo this effect, it means "unfold" our signal events.
- **Efficiency correction**: the efficiency is used to recover the signal event rate from our reconstructed candidates.

Cross section is calculated as

$$\frac{\partial\sigma}{\partial x}\Big|_i = \frac{\sum_j U_{ij}(N_j - B_j)}{n\phi_i\epsilon_i\Delta x_i} \tag{6.1}$$

where x is the variable of interest, i labels a bin of the measurement, Δx_i is the bin width, N_j is the number of events in bin j, B_j is the expected background in bin j, U_{ij} is a matrix element that unfolds out detector effects, ϵ_i is the bin efficiency, ϕ_i is the predicted neutrino flux, and n is the number of interaction targets.

For the single differential cross-section measurements the flux factor, ϕ_i, is constant and equals the total flux. For the total cross-section measurement as a function of neutrino energy

the flux factor is per energy bin. A cross-section is naturally a function of every degree of freedom associated with the interaction, constrained by conservation of energy, momentum, and angular momentum.

6.1.1 Background Subtraction

The first step towards estimating the number of interactions is to subtract the expected background from the measured event rate. To estimate the background we assume that our Monte Carlo background predictions are correct. Our Monte Carlo sample is not of the same size of our data sample, therefore, we must extract the fraction of the background, scale it to data using the ratio of their Proton On Targets (POT). When background fraction is measured in Monte Carlo this fraction is subtracted from data according to,

$$N_j^{bg-sub} = N_j - \frac{POT^{Data}}{POT^{MC}} B_j^{MC} \tag{6.2}$$

For $CC\pi^0$ exclusive sample, Monte Carlo predicts a purity 63% after all analysis cuts, and Monte Carlo predicts a $CC\pi^0$ inclusive sample that is 62% pure observable $CC\pi^0$. The contribution of the background interactions to the candidate rate appears in figure 6.1. For $CC\pi^0$ inclusive our background is coming from the π^0 production in the detector and mis-reconstruction of the π^0 (usually occurs in the presence of pions). For $CC\pi^0$ exclusive, our background comes from the same background as to $CC\pi^0$ inclusive and from events with final state particles like μ^+ π^0 X.

6.1.2 Unfolding

After the background has been subtracted the event rate must be corrected. Numerous detector effects coupled with imperfect reconstruction have the tendency to scatter reconstructed kinematics around their true value or even bias them away. This phenomenon is known as smearing. The inverse process is called Unfolding.

Bayesian probability that a given true event of some variable A and bin i (A_i^{true}), comes from a reconstructed event of the same variable but different bin j (A_j^{meas}), is given by

$$P(A_i^{true}|A_j^{meas}) = \frac{P(A_j^{meas}|A_i^{true})P(A_i^{true})}{\sum_{l=1}^{n_{A^{true}}} P(A_j^{meas}|A_l^{true})P(A_l^{true})} \tag{6.3}$$

The expected number of events to be assigned to each i true variable due to the measured of number events that can be calculated as:

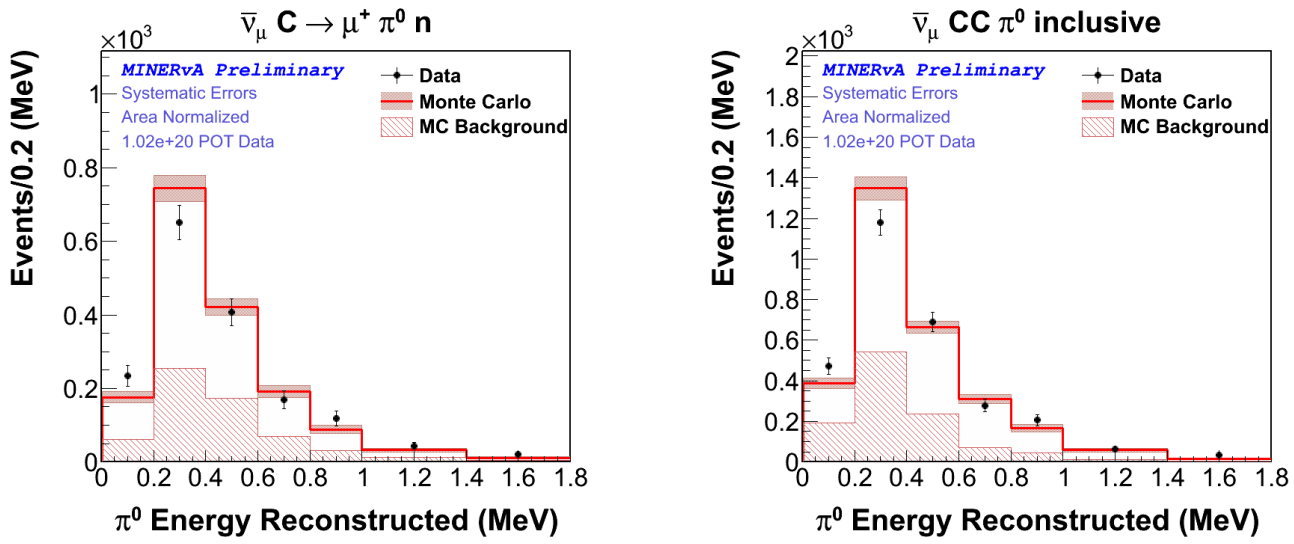

Figure 6.1: Left: Reconstructed E_{π^0}, data and Monte Carlo, relative normalized for $CC\pi^0$ exclusive. Right: Reconstructed E_{π^0} reconstructed for $CC\pi^0$ inclusive, data and Monte Carlo relative normalized.

$$\hat{n}(A_i^{true}) = \sum_{j=1}^{n_{A^{meas}}} n(A_j^{meas}) P(A_i^{true}|A_j^{meas}), \tag{6.4}$$

where $n_{A^{meas}}$ correspond to number of bins.

The unfolding method constructs a unfolding matrix from the Monte Carlo (Migration matrixU_{ij}) that maps reconstructed quantities to their predicted values. The chosen method utilizes the Iterative Bayes algorithm [96] that runs iteratively several times until χ^2 from $\hat{n}^{t+1}(A^{obs})$ and $\hat{n}^t(A^{obs})$ is small enough. $\hat{n}^{t+1}(A^{obs})$ comes from,

$$\hat{n}^{t+1}(A_i^{obs}) = \sum_{j=1}^{n_{A^{meas}}} n(A_j^{meas}) P^t(A_i^{true}|A_j^{meas}), \tag{6.5}$$

and $P^t(A_i^{true}|A_j^{meas})$ comes from,

$$P^t(A_i^{true}|A_j^{meas}) = \frac{P(A_j^{meas}|A_i^{true}) P^t(A_i^{true})}{\sum_{l=1}^{n_{A^{true}}} P(A_j^{meas}|A_l^{true}) P^t(A_l^{true})}, \tag{6.6}$$

where $P(A_j^{meas}|A_i^{true})$ represents the migration matrix elements. For the first iteration, t = 0, the probability $P^0(A_i^{true})$ is chosen from the best knowledge of the process under study,

$$P^0(A_i^{true}) = \frac{\hat{n}^0(A_i)}{N_{obs}}, \tag{6.7}$$

In case of total ignorance $P^0(A_i^{true})$ will be a uniform distribution: $(1/N_{meas})$. Figure 6.2 represents a migration matrix of the neutrino energy distribution for $CC\pi^0$ exclusive sample that associates the reconstructed Monte Carlo to the True Monte Carlo.

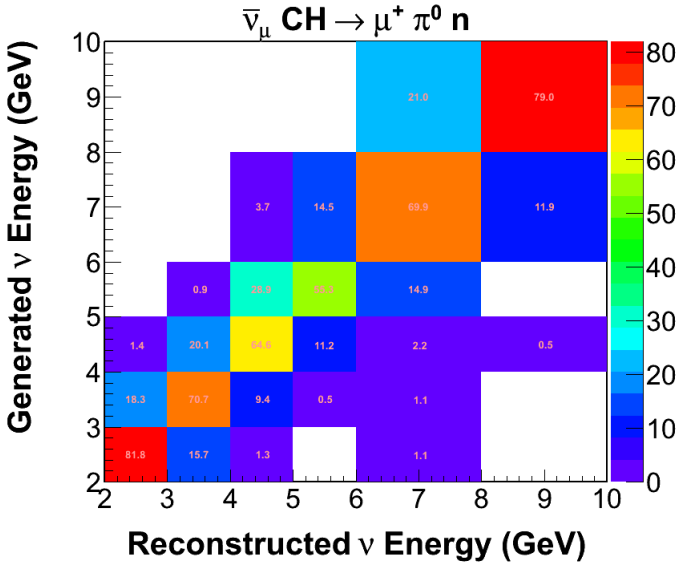

Figure 6.2: Migration matrix used to unfold the neutrino energy distribution for $CC\pi^0$ exclusive sample

6.1.3 Efficiency Correction

The unfolded distributions are efficiency corrected in a bin by bin basis. Efficiencies are estimated as the ratio between True Monte Carlo signal events (after reconstruction cuts and restricted to the fiducial volume) and the generated distribution of signal events (without cuts but restricted to the fiducial volume).

Let's $A_i^{reco}(true)$ be the number of events in bin i as selected by reconstructed Monte Carlo but with variable A True Monte Carlo information stored. To select an event we ask for a reconstruct muon with charge equal to 1. Then we ask for two reconstructed blobs and we store the associated True Monte Carlo π^0 energy (not the reconstructed π^0 energy). $A_i^{(true)}$ is all events generated that correspond to the bin i. Efficiency correction is given by,

$$N_j^{obs} = \sum_i U_{ji}(N_i - B_i) \times \frac{1}{\epsilon_i}, \qquad \epsilon_i = \frac{A_i^{reco}(true)}{A_i^(True)}, \tag{6.8}$$

The overall efficiency for selecting observable $CC\pi^0$ inclusive interactions is 3% and the purity is 62%. For $CC\pi^0$ exclusive interactions the efficiency is 6% and the purity is 64%. The bulk of events is lost by the muon selection and π^0 reconstruction when the topology is not

simple. The cuts to reduce the background and preserve well-reconstructed events account for the remainder.

Figure 6.3 shows the muon energy efficiency and energy purity for the $CC\pi^0$ exclusive sample.

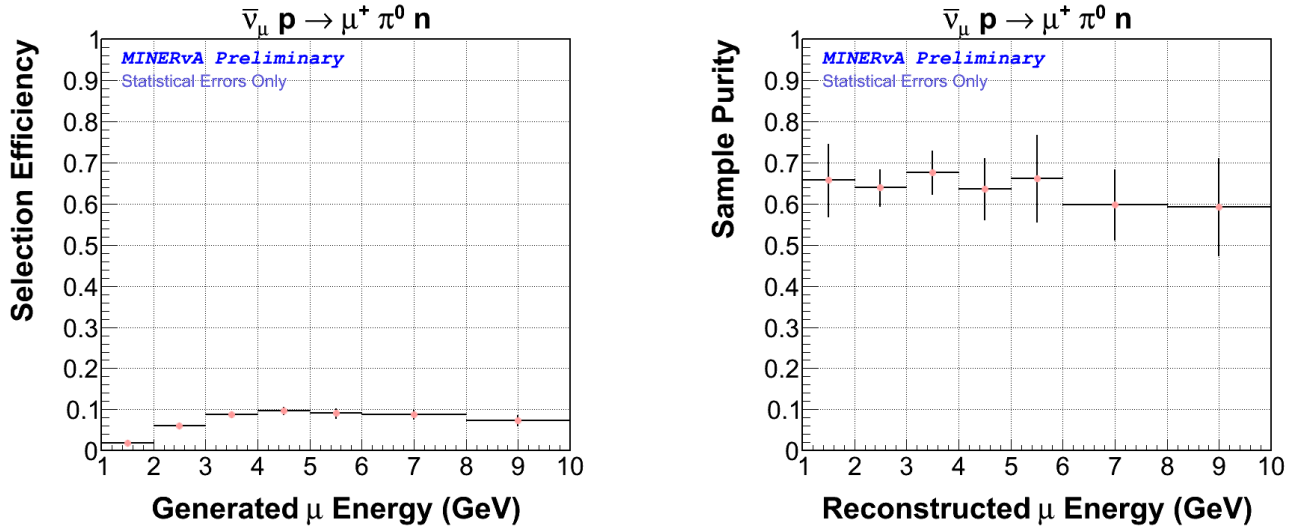

Figure 6.3: Left: E_{μ^+} efficiency for $CC\pi^0$ exclusive sample. Right: E_{μ^+} purity for $CC\pi^0$ exclusive sample.

6.1.4 Number of Targets

The number of interaction targets is calculated in the fiducial volume. The target is a type of polystyrene scintillator with other elements present in the amounts listed in table 6.1 [97]. These elements are contained in the optical fiber, epoxy, and light sealing materials used in construction of each plane.

Element	Atoms / cm^2 / plane
C	8.89×10^{22}
H	9.03×10^{22}
O	0.24×10^{22}
Ti	1.76×10^{20}
Al	1.11×10^{20}
Si	1.29×10^{20}
Cl	1.89×10^{20}

Table 6.1: Number of atoms per centimeter squared per plane in the MINERνA fiducial volume.

8.89×10^{22} carbon atoms per cm^2 per plane, times the area of hexagon (85 cm apothem) and 57 planes in our fiducial volume corresponds to 1.26825×10^{29} C atoms.

6.2 Systematic Uncertainties

Systematic uncertainties play a key role in our cross section measurements and are different from statistical uncertainties. Systematic Uncertainties are due to uncertainties in the apparatus or model and correlated with previous measurements. The systematics errors used in this dissertation are the errors coming from our event generator (GENIE) and our reconstructions.

In MINERνA we apply event weights (Vertical Errors) to deal with this errors. A comprehensive description about how to apply systematic uncertainties from the neutrino interaction model is found in [98]. Our current event weights are obtained by simultaneously varying all internal model parameters in our Monte Carlo. The parameter values are drawn randomly based on an estimate of the 1σ uncertainty for each parameter. Every draw is referred to as a universe and the event weight is assigned to the diagonal of the covariance matrix [99]. In the standard software configuration MINERνA generates 1000 universes for each event.

The normalization corrections from our reconstructions are described in [100]. In our analysis we apply the following correction factor:

- Track reconstruction efficiency: 4.5%
- Minos muon acceptance: 2.5%
- Minos rate effect: 2.8%
- Mass assay: 1.4%

Comparison of data and Monte Carlo includes signal and background events, so the uncertainty on those distributions is also coming from background and signal events. Figure 6.4 shows the reconstructed event and uncertainties distribution as a function of the muon energy for data and Monte Carlo.

In order to measure $CC\pi^0$ inclusive and $CC\pi^0$ exclusive cross sections we must subtract the background from our sample as described in subsection 6.1.1 as,

$$N^{CV}_{signal} = N^{sel}_{Data} - B_{CV} \tag{6.9}$$

where N^{CV} and B_{CV} represents central value of signal and background.

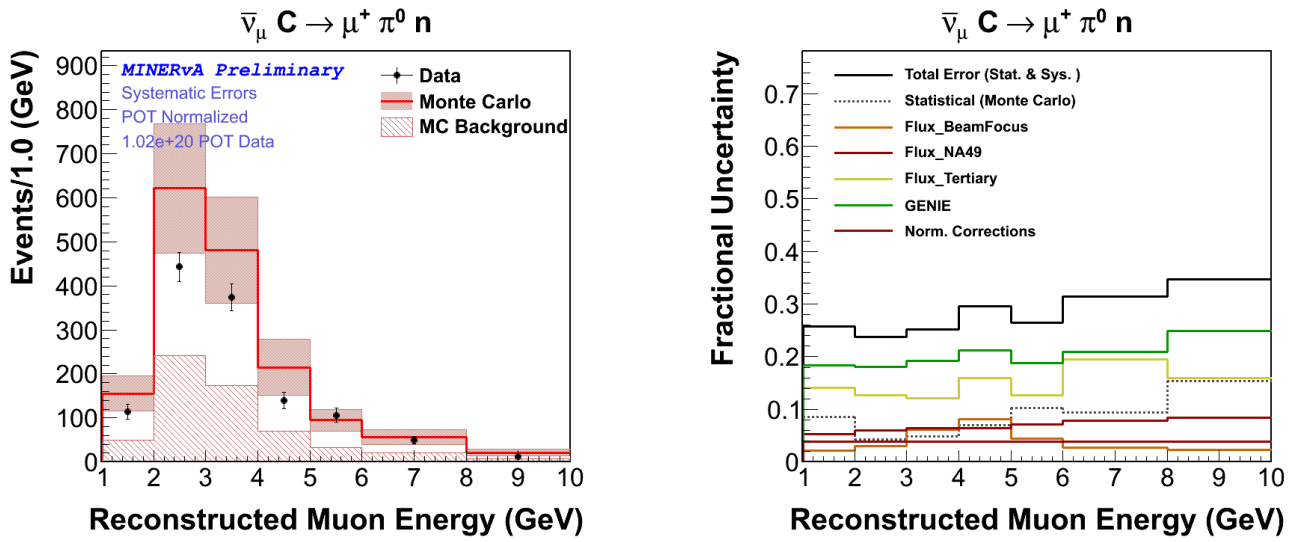

Figure 6.4: Left: Data and Monte Carlo comparison of $CC\pi^0$ exclusive events, absolute normalized. Right: Fractional error as a function of the muon energy, $CC\pi^0$ exclusive sample.The large uncertainties come from the cross section model (GENIE).

After background subtraction, we still need to calculate the errors from the measured signal events (data). For that, we build many different possible signal event distributions N^j_{signal} (in order to associate to our systematics errors) by subtracting different MC background universe from our single data distribution,

$$N^j_{signal} = N^{sel}_{Data} - B^j \tag{6.10}$$

6.3 Cross Sections

Having a comprehensive $CC\pi^0$ event reconstruction allows for detailed measurements of $CC\pi^0$ interaction cross-sections. The cross-section is dependent only on the neutrino energy. It is measured relative to the incident neutrino direction. Each cross section, whether total or differential, is a flux-averaged cross section. The mean energy of $\bar{\nu}_\mu$ in the Anti Neutrino beam is $\sim 3GeV$ and we assume C atoms as the interaction targets.

The measurements presented in this doctoral thesis are the most comprehensive measurements of $\bar{\nu}$ $CC\pi^0$ interactions to date. The total $CC\pi^0$ cross-section is measured as a function of the neutrino energy and Q^2 for $CC\pi^0$ inclusive and $CC\pi^0$ exclusive. For $CC\pi^0$ exclusive we also calculate the cross-section as a function of $cos\pi^0$ and of the π^0 momentum. Before this analysis there was no measurement of $\bar{\nu}$ $CC\pi^0$. Figure 6.6 shows how the background

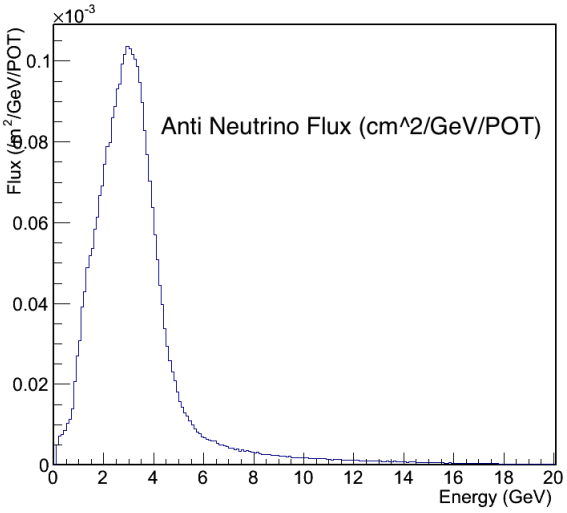

Figure 6.5: Anti Neutrino flux used for cross sections calculations[83]

subtraction is applied to our Neutrino Energy sample from $CC\pi^0$ exclusive.

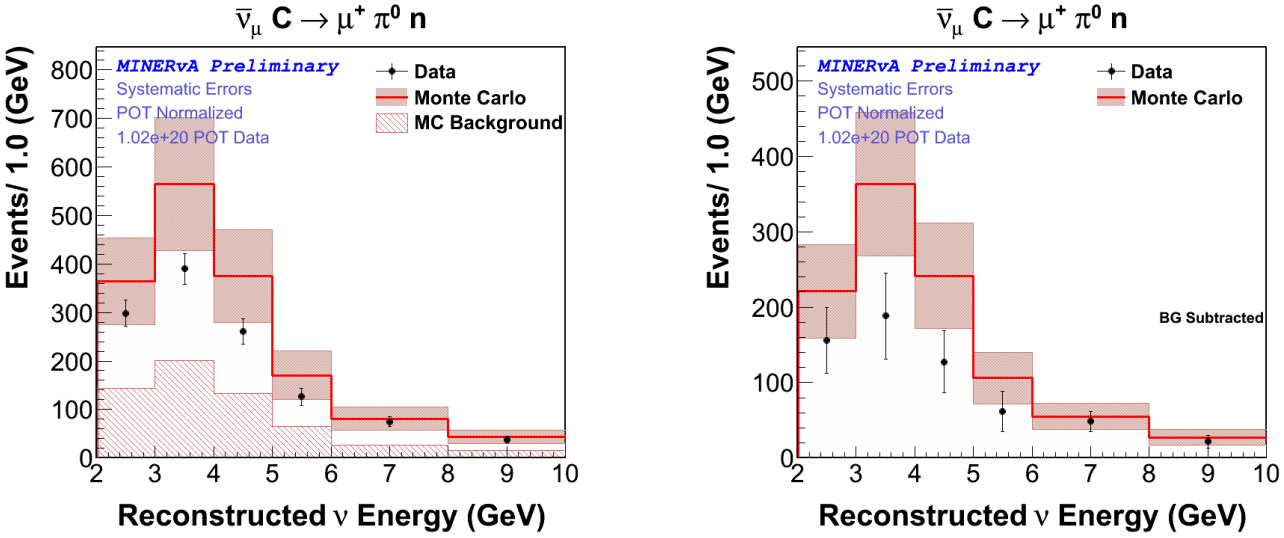

Figure 6.6: Left: $E_{\bar{\nu}_\mu}$ for $CC\pi^0$ inclusive including Monte Carlo background, absolute normalized. Right: $E_{\bar{\nu}_\mu}$ for $CC\pi^0$ inclusive after background subtraction.

In order to isolate our signal events from the selected events, we subtract the background and unfold the distribution to retrieve our generated sample. We then correct by the efficiency. Figure 6.7 shows the last two steps.

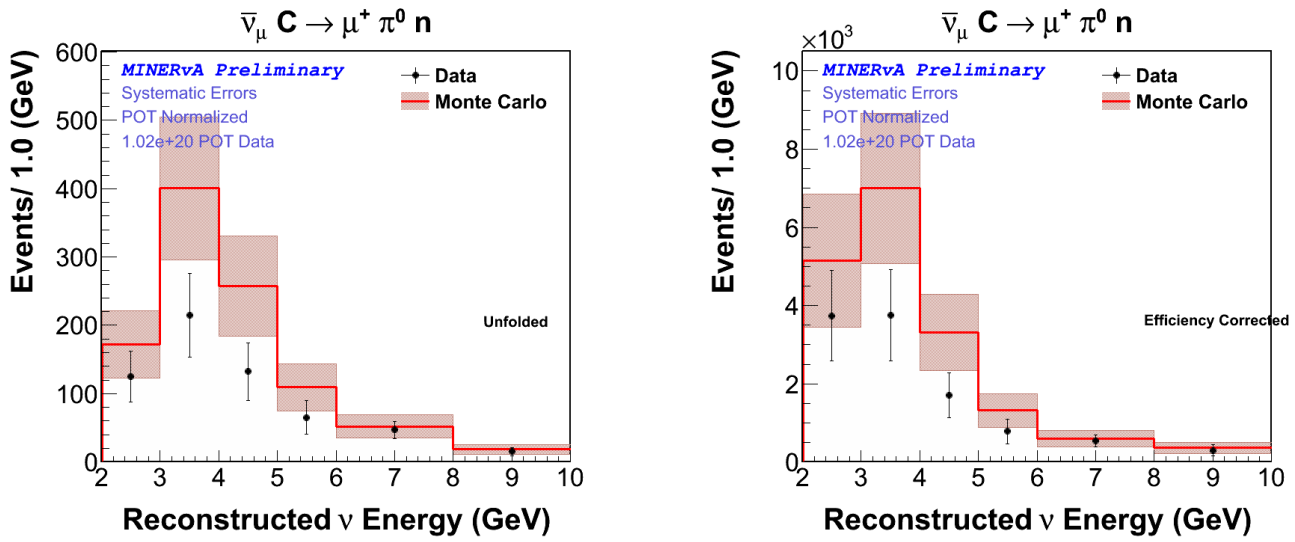

Figure 6.7: Left: $E_{\bar{\nu}_\mu}$ for $CC\pi^0$ inclusive unfolded, absolute normalized. Right: $E_{\bar{\nu}_\mu}$ for $CC\pi^0$ inclusive after efficiency correction.

We can then compare our reconstructed (observed) Monte Carlo and our generated Monte Carlo as in figure 6.8. We are then ready to use the distribution to measure the cross section, taking the targets and the anti neutrino flux into account. The matching between generated and observed sample tells us that we are using the right tools to calculate the cross-section measurements.

6.3.1 $CC\pi^0$ inclusive cross sections

Plots in figure 6.9 show the calculated total cross section as a function of Q^2 and of the neutrino energy. These Cross Sections are important for the understanding of the π^0 production in neutrino interactions. We still need to improve our understanding about the errors coming from the flux and the systematic errors resulting from the π^0 reconstruction.

6.3.2 $CC\pi^0$ exclusive cross sections

Our $CC\pi^0$ exclusive event selection has a purity good enough to be guaranty that out selection contains π^0 events. In figure 6.10 we plot the differential Cross Section a as function of $cos\theta^0_\pi$ and as function of π^0 momentum. The total Cross Section as function of the neutrino energy and the differential Cross Section as function of Q^2 is shown in figure 6.11.

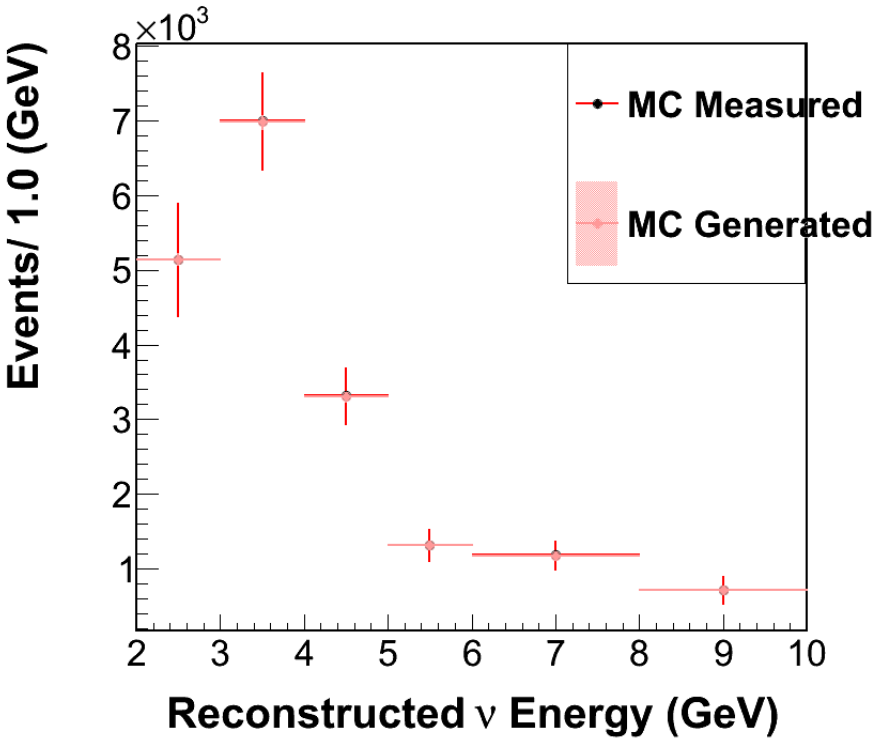

Figure 6.8: Generated and observed samples

6.3.3 Cross Sections Ratio for $CC\pi^0$ production

We can perform a test our Monte Carlo models, calculating the ratio of the cross sections for $CC\pi^0$ inclusive and $CC\pi^0$ exclusive data and Monte Carlo. Figure 6.12 we show the ratio for total cross sections. We see a big difference around 2 GeV suggesting that we may be overestimating the $CC\pi^0$ exclusive for that energy in data respect to Monte Carlo.

Our second test is calculate the same ratio, but now for the differential cross section as function of Q^2, again there is difference with Q^2. Figure 6.13 show both plots for Monte Carlo and Data. There is, again, a difference for Q^2 around 0.05 GeV^2/c^2.

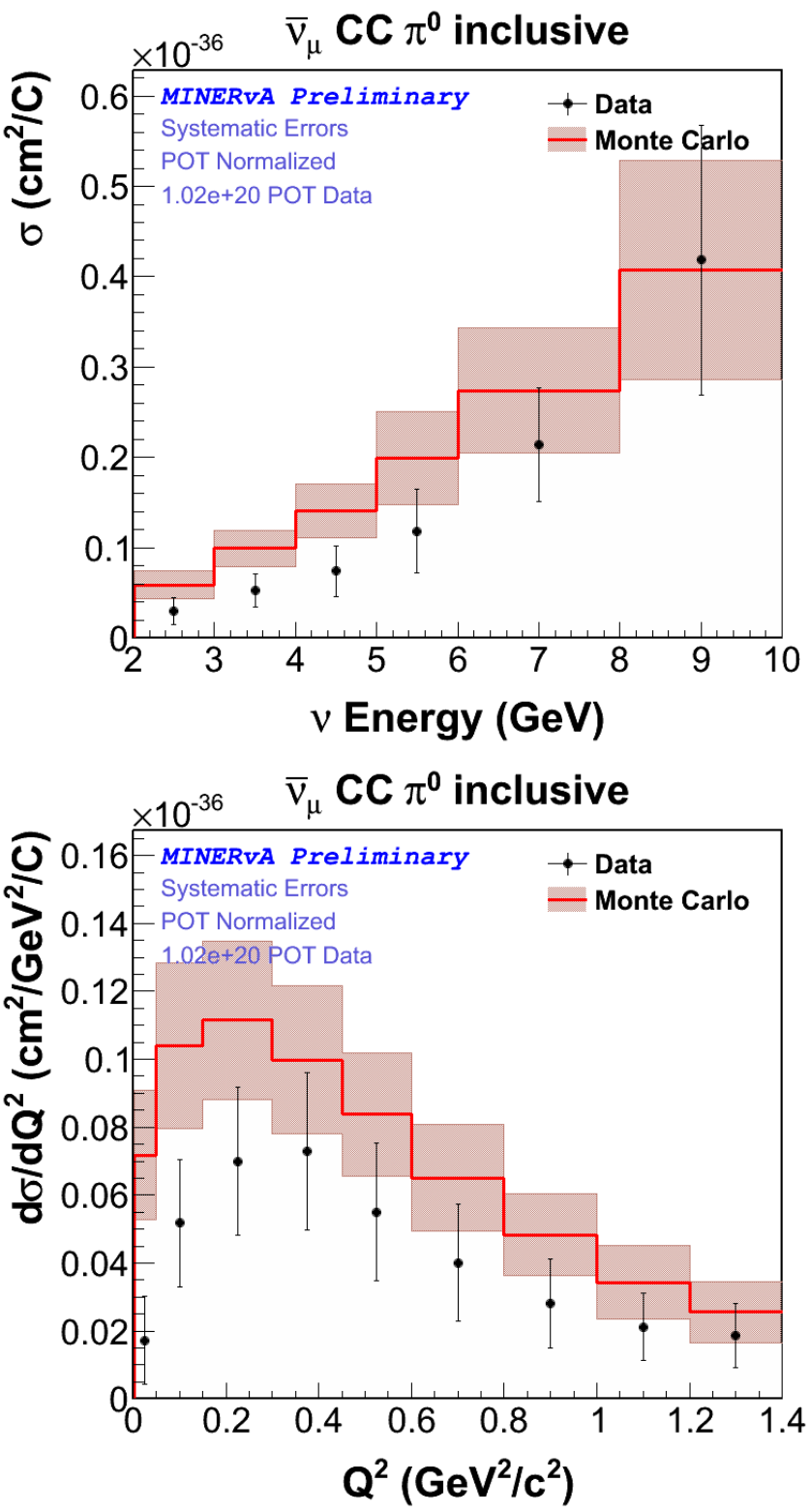

Figure 6.9: Top: Total observable cross-section as a function of neutrino energy for $CC\pi^0$ inclusive. Bottom: $CC\pi^0$ inclusive differential cross section as a function of Q^2.

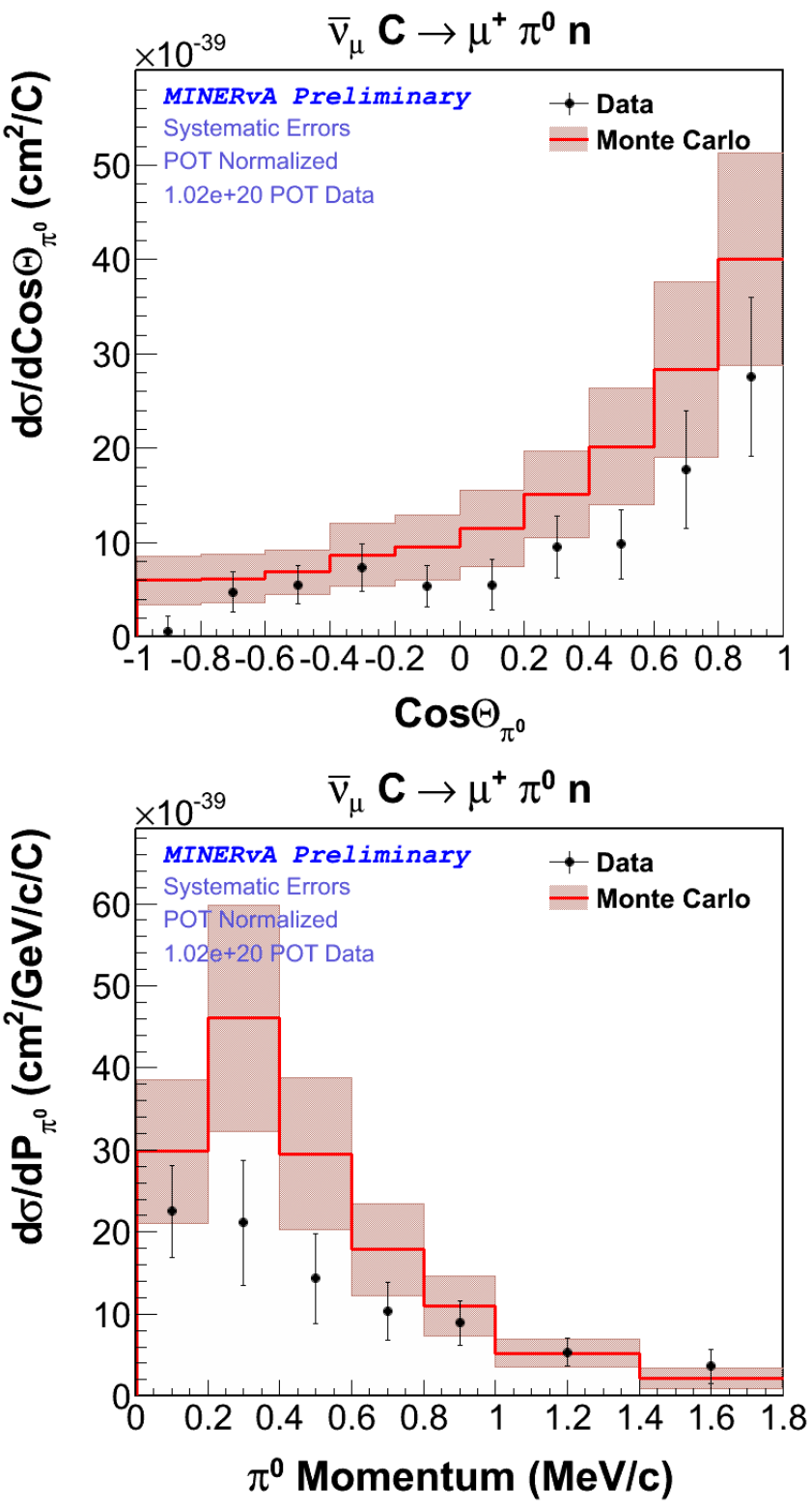

Figure 6.10: Top: $CC\pi^0$ exclusive differential cross section as a function of $cos\theta^0_\pi$.Bottom: $CC\pi^0$ exclusive differential cross section as a function of Q^2.

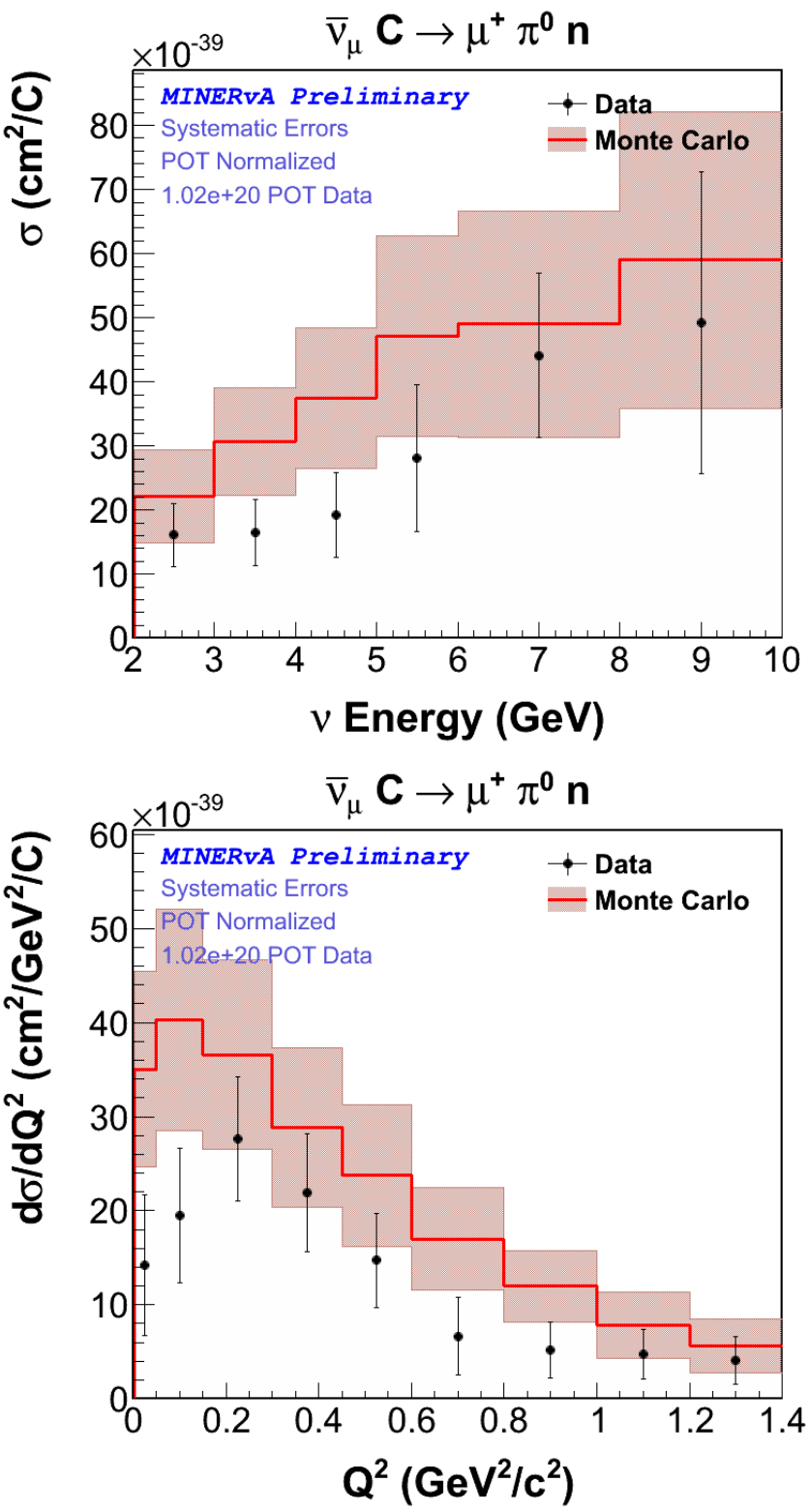

Figure 6.11: Top: The total observable cross-section as a function of neutrino energy for $CC\pi^0$ exclusive. Bottom: $CC\pi^0$ exclusive differential cross section as a function of Q^2.

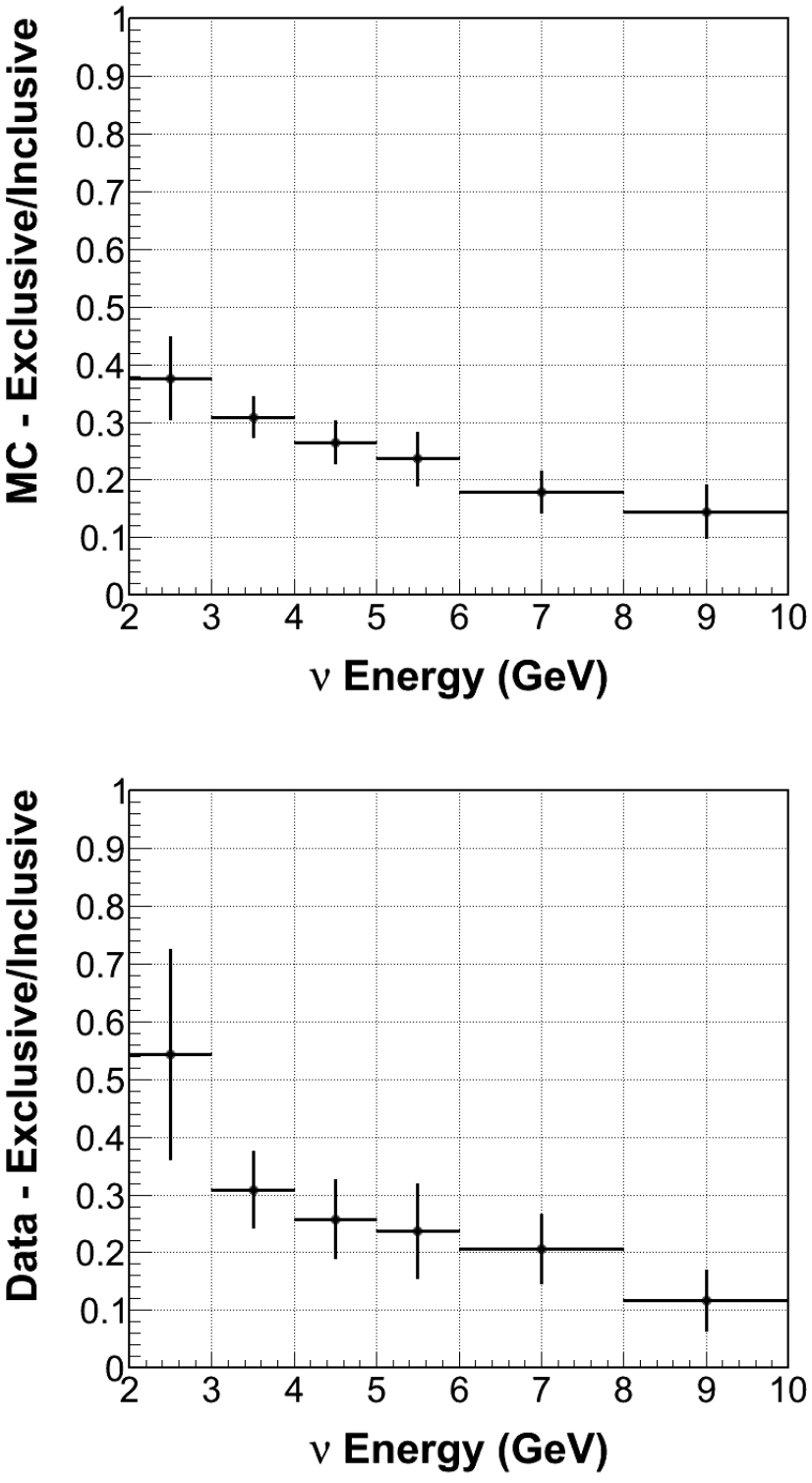

Figure 6.12: Ratio between $CC\pi^0$ inclusive and $CC\pi^0$ exclusive total cross section as a function of $E_{\bar{\nu}\mu}$ Top: Monte Carlo. Bottom: data.

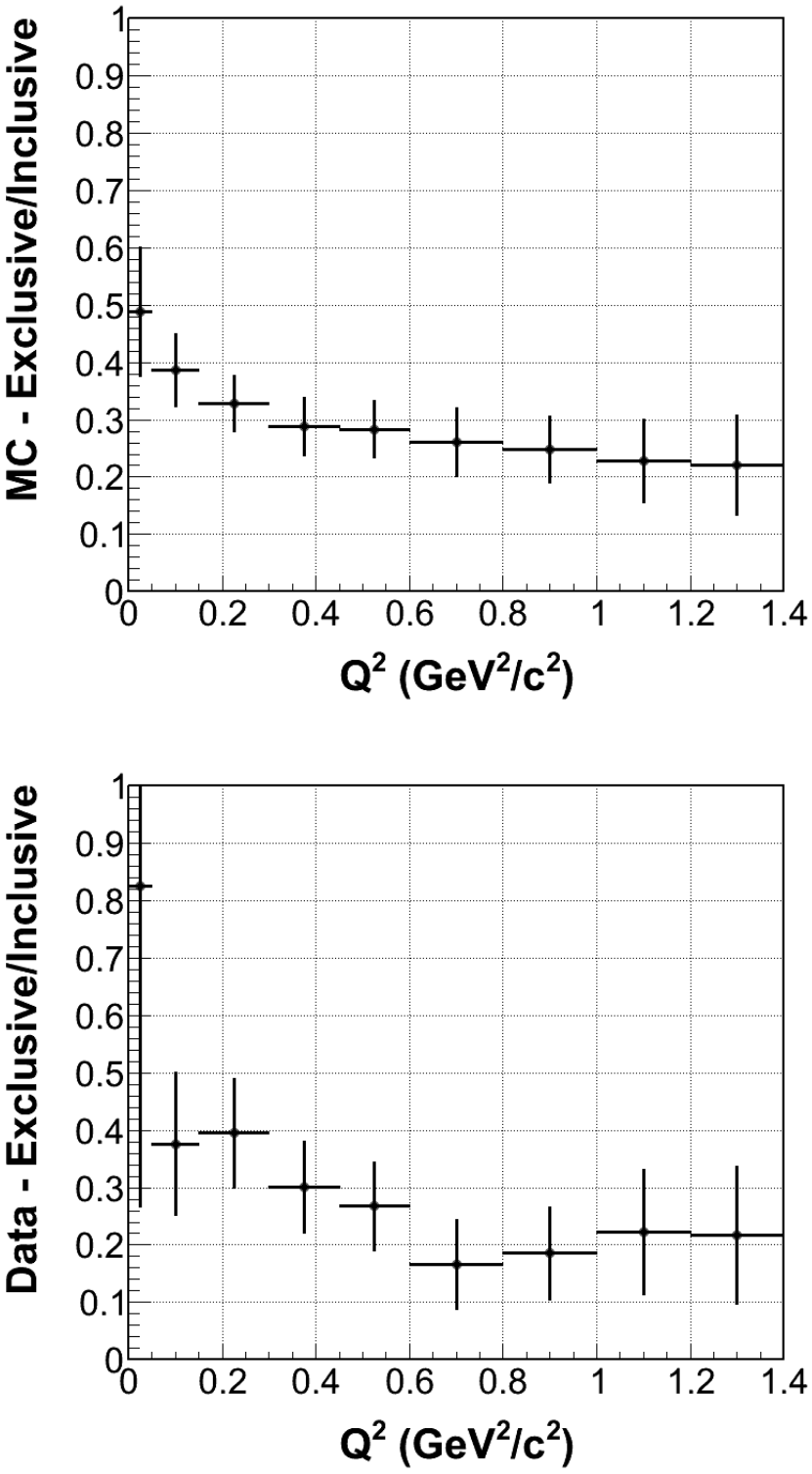

Figure 6.13: Ratio between $CC\pi^0$ inclusive and $CC\pi^0$ exclusive differential cross section as a function of Q^2 Top: Monte Carlo. Bottom: data.

Chapter 7

Conclusions

I have worked in the Electromagnetic Final State Working Group in the MINERνA experiment. My work is center around $\bar{\nu}$-Induced Charge-Current π^0 production, I have developed two methods for the π^0 reconstruction:

- Angle Scan, method described on the Section 4.2. The method is to clustering hits with angle dependence with respect to the event vertex. This method has good efficiency when the photons are well defined and do not traveling in same direction.
- Hough Transform, method described on the Section 4.3. We use the Hough Transformation to get the main direction of the gammas. This method is powerful when the photons are pretty close.

Both methods are used to isolate and reconstruct gammas coming from the π^0 decay. Our quality measurements like gamma energy ratio(1.08) and energy residual ($16MeV$) between reconstructed and true allow a good π^0 reconstruction. The residuals for the γ momentum are $1.69MeV$ for p_x, $0.88MeV$ for p_y and for p_z $1.28MeV$). For π^0 momentum our residuals $1.63MeV$ for p_x, 1.31 MeV for p_y and $2.64MeV$ for p_z. A important variable to quantify our π^0 reconstruction is the invariant mass calculation Angle Scan and for Hough Transform provide 135.3 and 135.3 MeV/c^2 as the π^0 invariant mass.

We use kinematics variables distribution to double-check our reconstruction, we select events for $CC\pi^0$ inclusive and $CC\pi^0$ exclusive samples, and then compare Monte Carlo and data. We have verified that our Monte Carlo and methods are working well.

Our measurements presented here provide the most complete understanding of $\bar{\nu}$ induced $CC\pi^0$ interactions at energies above 2 GeV to date. We have shown that our sample and Monte Carlo almost match perfectly. Every step in the calculation of Cross Sections has a good

confidence level. The reconstruction developed in this thesis allow the measurement of the full kinematics of the event and resulted in the measurement of six cross sections:

- The total cross section as a function of neutrino energy, for the $CC\pi^0$ inclusive
- Flux-averaged differential cross sections in Q^2, for the $CC\pi^0$ inclusive.
- The total cross section as a function of neutrino energy, for the $CC\pi^0$ exclusive
- Flux-averaged differential cross sections in Q^2, for the $CC\pi^0$ exclusive.
- Flux-averaged differential cross sections in π^0 Energy, for the $CC\pi^0$ exclusive.
- Flux-averaged differential cross sections in $Cos\theta_{\pi^0}$, for the $CC\pi^0$ exclusive.

The ratio between the total and diferential Cross Section between $CC\pi^0$ inclusive and $CC\pi^0$ exclusive, including errors, are in good agreement with our Monte Carlo model. There is an ongoing analysis applying the same methods to reconstruct π^0 events on Neutrino Interactions. We have applied the methods developed in this dissertation to a small sample of Neutrinos with encouraging results (Appendix A).

Appendix A

First test of ν-Induced Charged-Current π^0 Production

Our antineutrino sample is not 100% pure since it contains a small amount of neutrino events that is part of the noise. In order to test our methods of reconstruction, we do our reconstruction requiring muons (rather than anti-muons) in the final state.

$$\nu_\mu C \rightarrow \mu^- \pi^0 X \tag{A.1}$$

We plot the invariant mass, vertex energy and dispersed energy for "neutrino" events that pass our reconstruction. The figure A.1, shows the invariant mass.

Figure A.2 shows the vertex enrgy distribution. This distribution is quite different from our $\bar{\nu}$ $CC\pi^0$ reconstruction, where the vertex energy distribution shows a huge peak in $0MeV$. The difference may be associated to a proton and other particles coming out from the nucleus (at muon vertex) so the energy of the vertex is not zero. All clusters that are not part of any MINERνA object are grouped in a blob called dispersed blob. Figure A.3 shows the distribution of this dispersed energy.

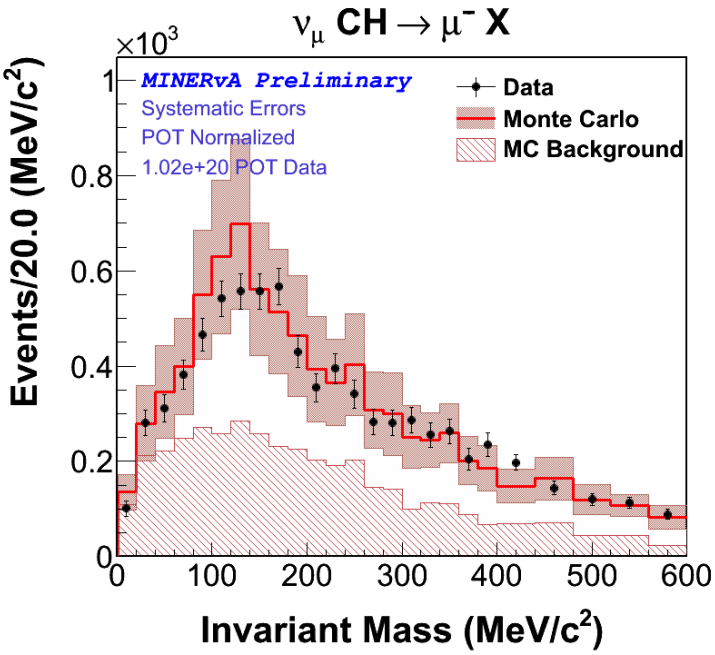

Figure A.1: Reconstructed π^0 invariant mass, data and Monte Carlo including Monte Carlo background prediction.

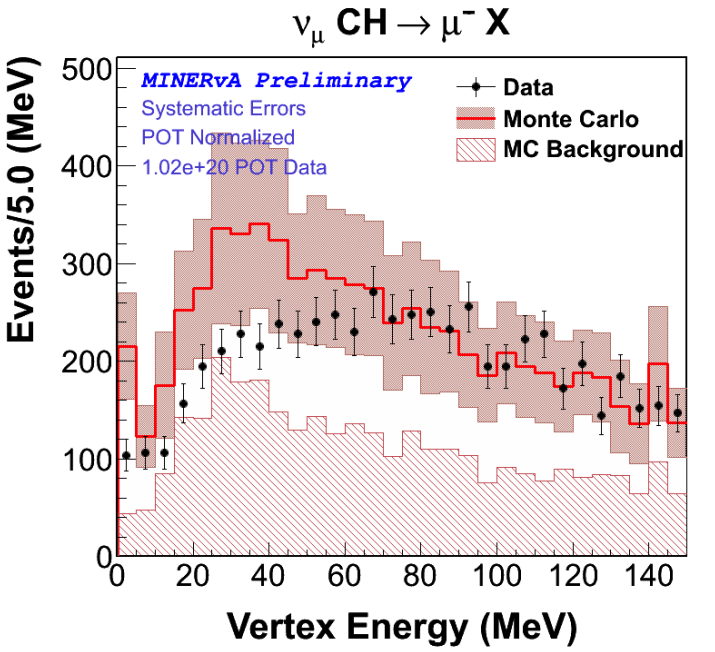

Figure A.2: Vertex energy for for reconstructed π^0 from ν_μ events, data and Monte Carlo including Monte Carlo background.

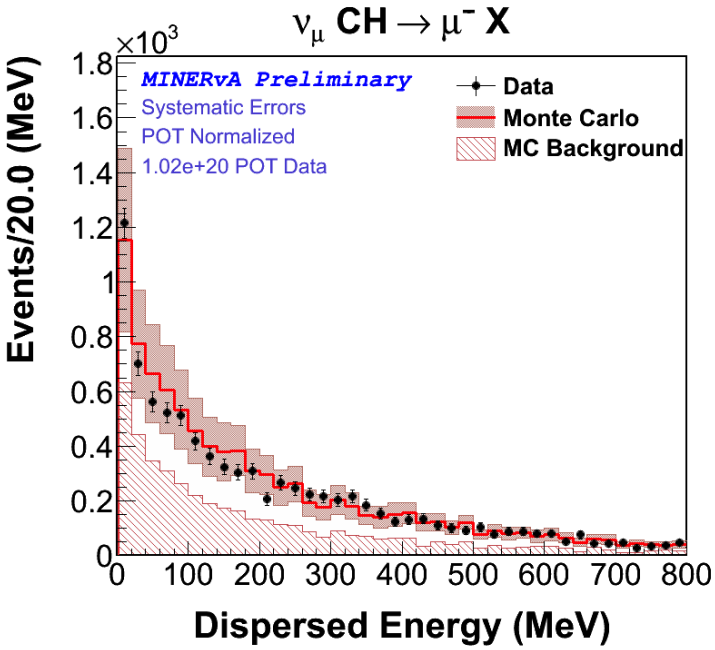

Figure A.3: Dispersed energy distribution for π^0 from ν_μ events

Appendix B

Resolution and Quality Plots for the $CC\pi^0$ Analysis

B.0.4 $CC\pi^0$ exclusive

In section 6.3.2 we calculate the $CC\pi^0$ exclusive cross section as function of the neutrino energy, Q^2, π^0 momentum and $cos\theta_{\pi^0}$. We have to deal with residuals (true - reconstructed) before completing any analysis. This residual distribution must be a symmetric around 0. Figure B.1 shows the residual distribution for π^0 momentum and $cos\theta_{\pi^0}$. Figure B.2 shows the residual distribution for Q^2 and $E_{\bar{\nu}_\mu}$. Figure B.3 shows efficiency and purity as a function of $E_{\bar{\nu}_\mu}$. Figure B.4 shows the efficiency and the purity as a function of Q^2.

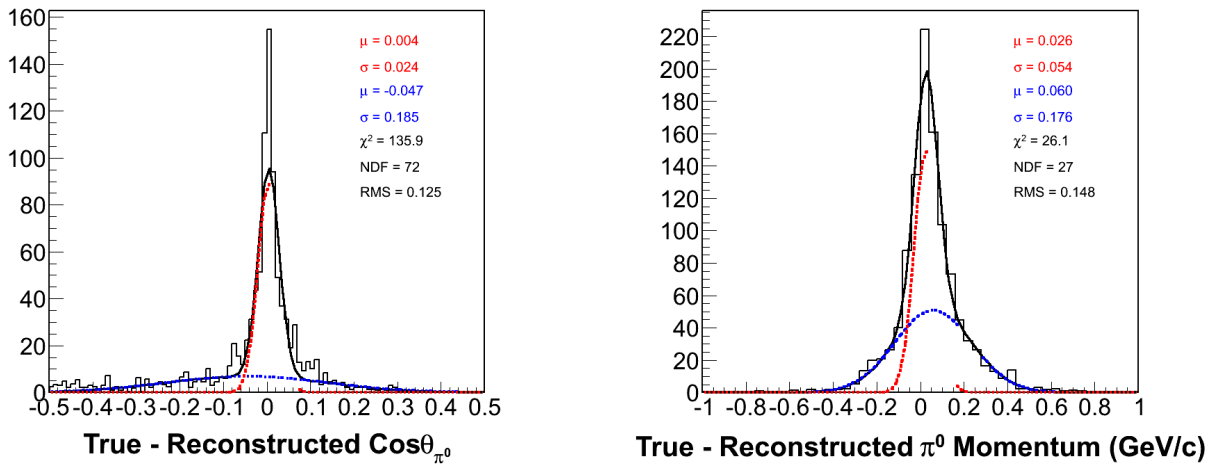

Figure B.1: Left: $cos\theta_{\pi^0}$ residuals for $CC\pi^0$ exclusive events. Right: π^0 momentum residuals for $CC\pi^0$ exclusive sample.

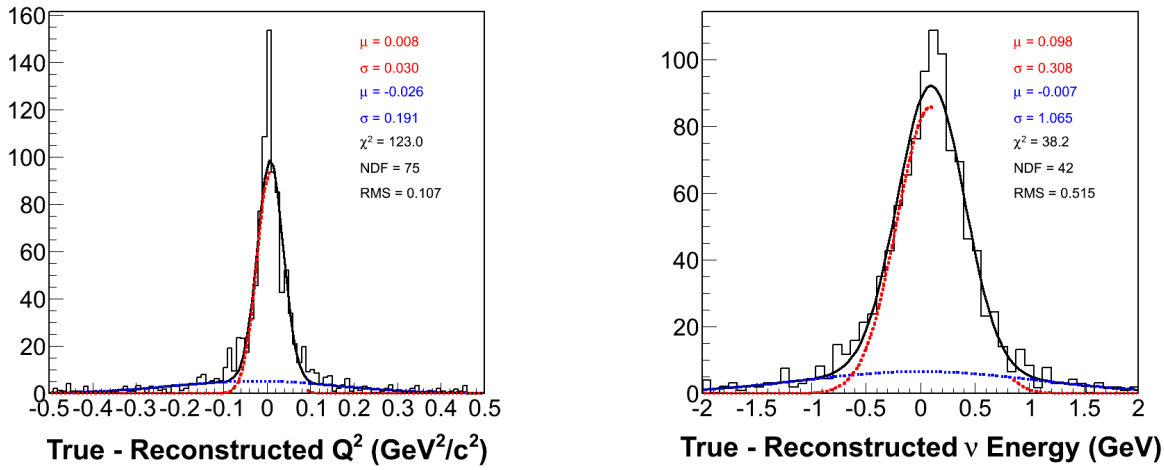

Figure B.2: Left: Q^2 residuals for $CC\pi^0$ exclusive sample. Right: $E_{\bar{\nu}_\mu}$ residuals for $CC\pi^0$ exclusive events.

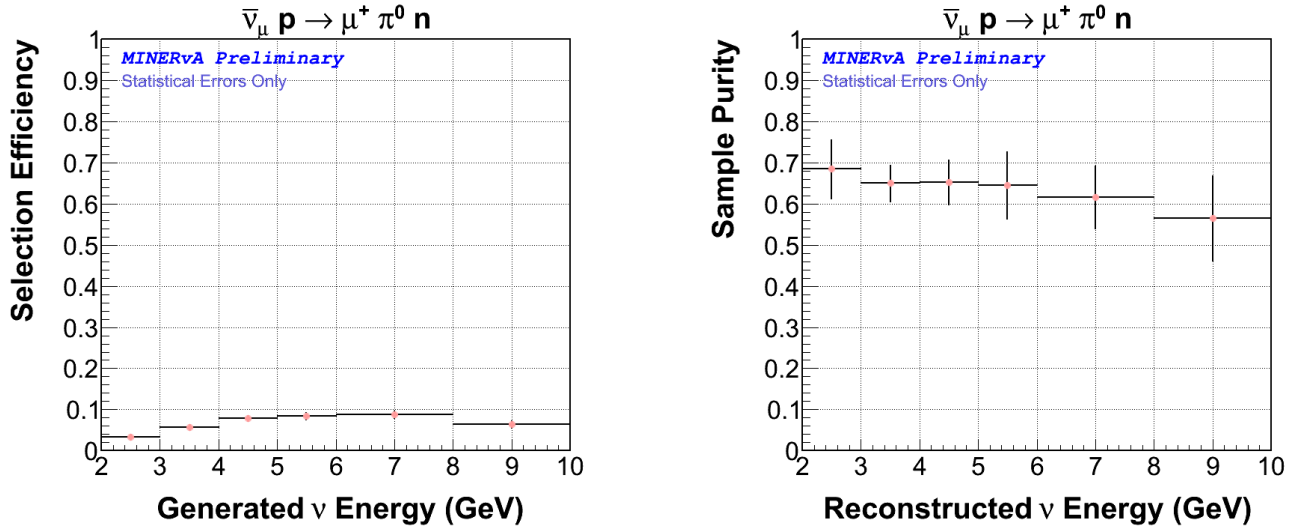

Figure B.3: Left: $E_{\bar{\nu}_\mu}$ efficiency for $CC\pi^0$ exclusive sample. Right: E_{μ^+} purity for $CC\pi^0$ exclusive sample.

Figure B.5 shows how many times Angle Scan and Hough Transform reconstruct π^0. Angle Scan reconstructs 62% of the generated π^0 and Hough Transform reconstructs 38%. Figure B.6 shows how many events are reconstructed using 2 views or 3 views.

B.0.5 $CC\pi^0$ inclusive

In section 6.3.1 we calculate the $CC\pi^0$ inclusive cross sections as a function of Q^2 and $E_{\bar{\nu_\mu}}$. Figure B.7 shows the residual distribution for those quantities. Note that the residual of

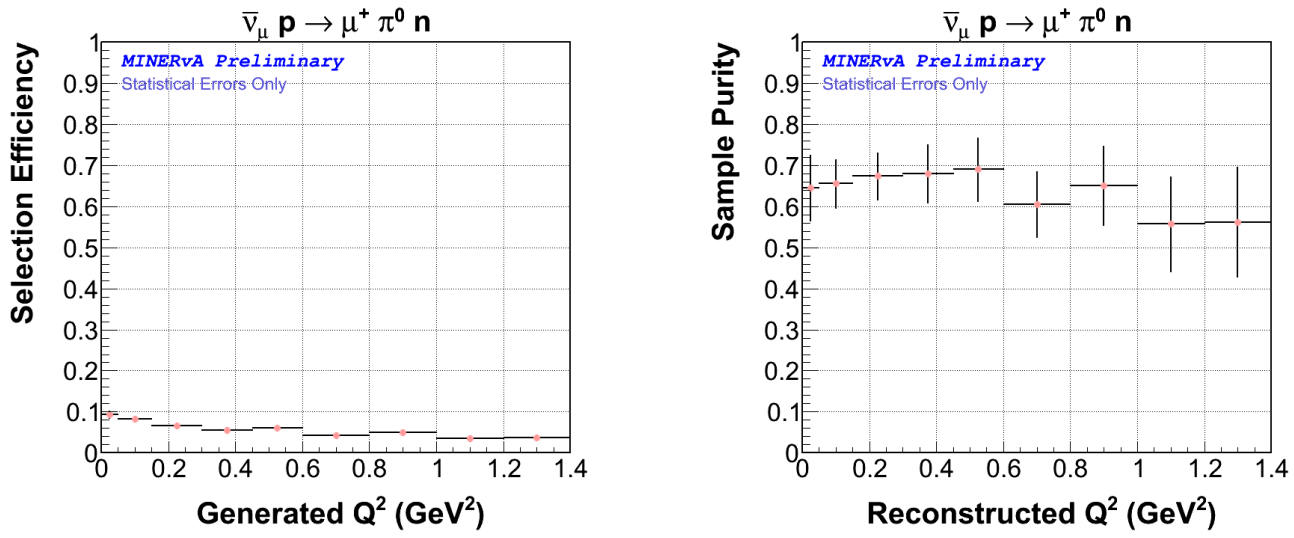

Figure B.4: Left: Q^2 efficiency for $CC\pi^0$ exclusive sample. Right: Q^2 purity for $CC\pi^0$ exclusive sample.

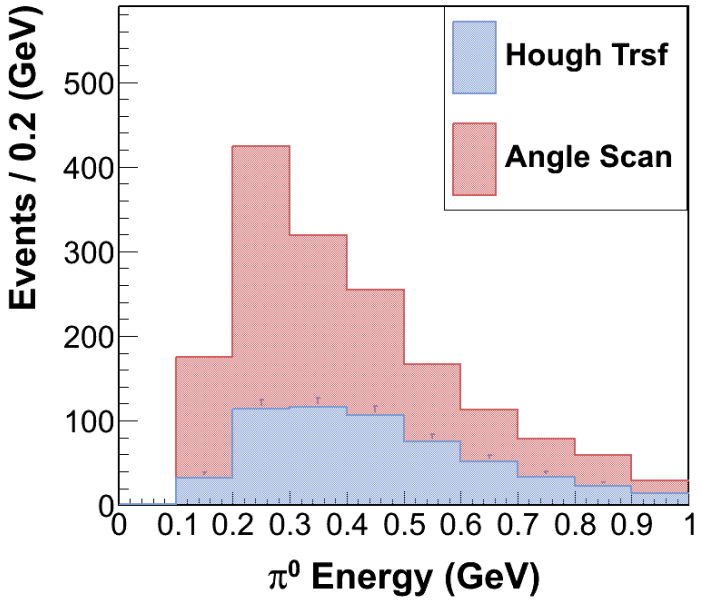

Figure B.5: Our Monte Carlo sample is 1773 events reconstructed for $CC\pi^0$ exclusive. Angle Scan reconstructs 1103 events(62%) and Hough Transform reconstructs 670 (38%)1773

E$_{\bar{\nu_\mu}}$ in the $CC\pi^0$ inclusive sample is $(148MeV)$ is bigger than the one in the $CC\pi^0$ exclusive sample $(105MeV)$. This difference is because the $CC\pi^0$ inclusive topology is more difficult to reconstruct. Our Neutrino Energy formula (Equation 2.32) assumes final state particles μ^+, n and π^0 but most of the $CC\pi^0$ inclusive events contains the final state particles μ^+, π^0 and X, where X can be any other particle(s). Figure B.8 shows the efficiency and purity as a function

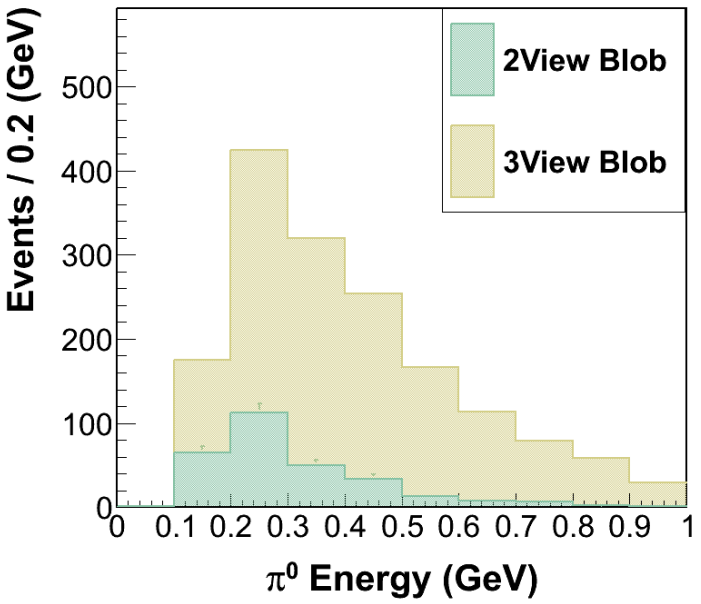

Figure B.6: We use $CC\pi^0$ exclusive sample, where 1477 evens were reconstructed using the 3 views, it represents (83%) and 296 events were reconstructed using just 2 views, which represents (17%).

of $E_{\bar{\nu_\mu}}$. Figure B.9 shows the efficiency and the purity as a function of Q^2.

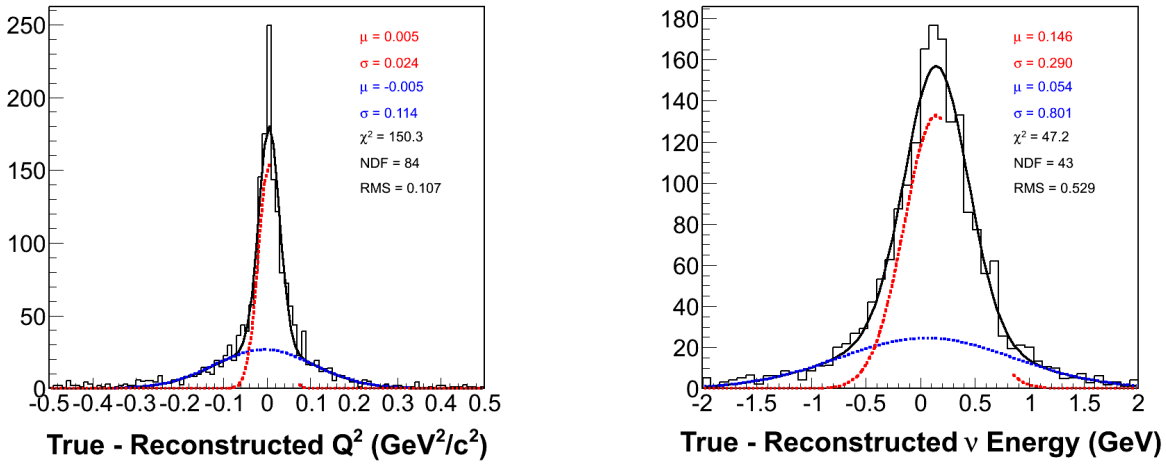

Figure B.7: Left: Q^2 residuals for $CC\pi^0$ inclusive sample. Right: $E_{\bar{\nu}_\mu}$ residuals for $CC\pi^0$ inclusive events.

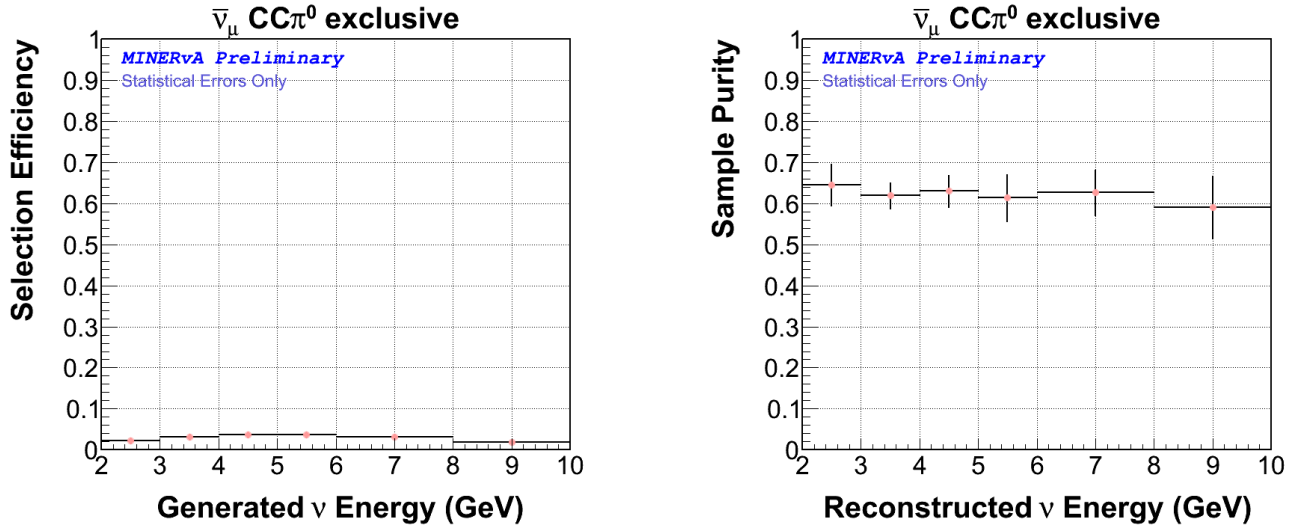

Figure B.8: Left: $E_{\bar{\nu}_\mu}$ efficiency for $CC\pi^0$ inclusive sample. Right: E_{μ^+} purity for $CC\pi^0$ inclusive sample.

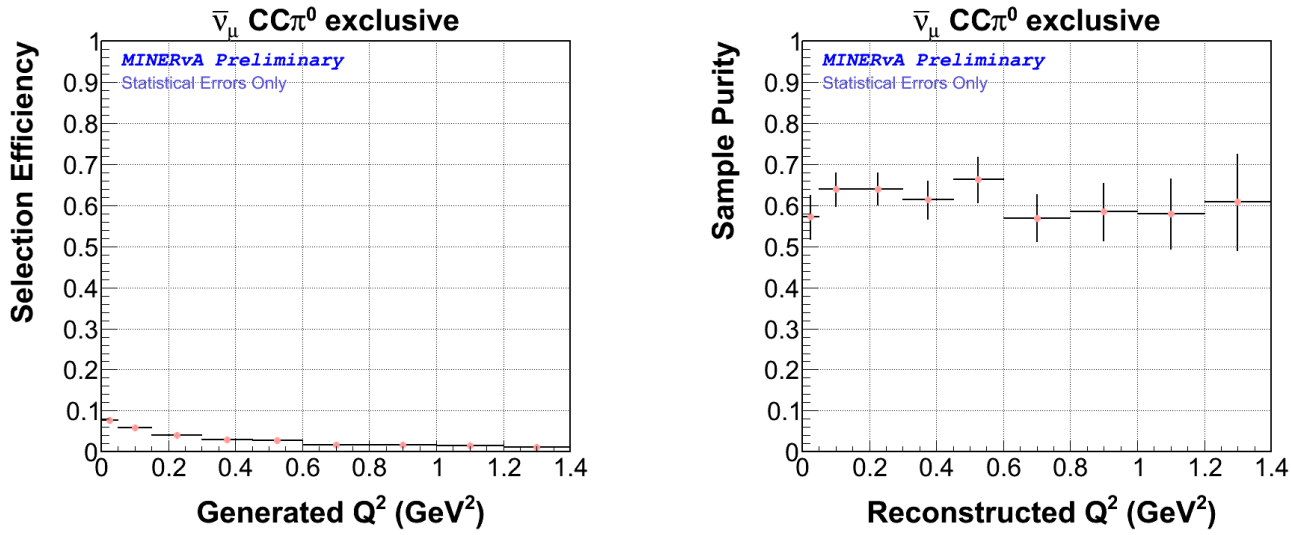

Figure B.9: Left: Q^2 efficiency for $CC\pi^0$ inclusive sample. Right: Q^2 purity for $CC\pi^0$ inclusive sample.

For $CC\pi^0$ inclusive 56% events were reconstruct by Angle Scan method and 44% events are reconstructed by the Hough Transform method. Figure B.10 the the distribution on reconstructed events, by both methods, as a function of E_{π^0}.

From our reconstructed Monte Carlo $CC\pi^0$ inclusive sample 17% events were reconstructed using 2 views and 83% events were reconstructed with clusters from the 3 views (X-U-V). Note how this proportion between 2 views blobs and 3 views blobs is the same found

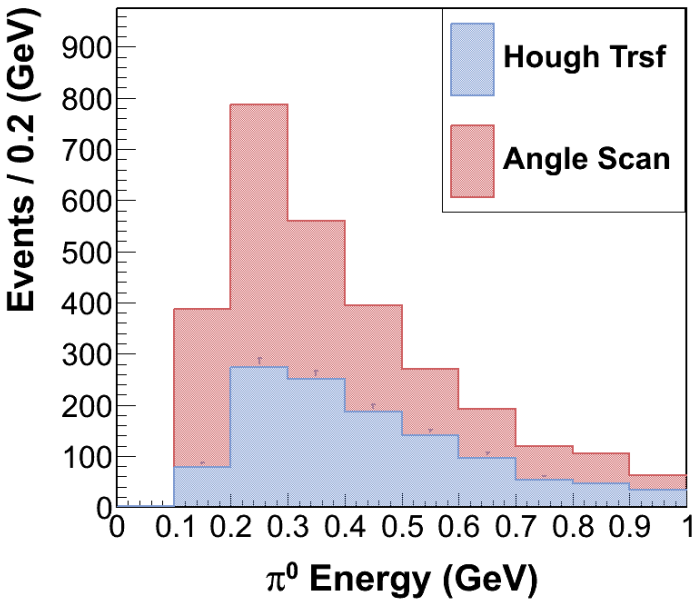

Figure B.10: Our Monte Carlo sample is 3326 events reconstructed for $CC\pi^0$ inclusive. Angle Scan reconstruct 1872 events (56%) and Hough Transform reconstruct 1454 events (44%).

for the $CC\pi^0$ exclusive sample. Our methods are related to the π^0 topology, and not to final state particles. Figure B.11 shows the distribution of reconstructed events.

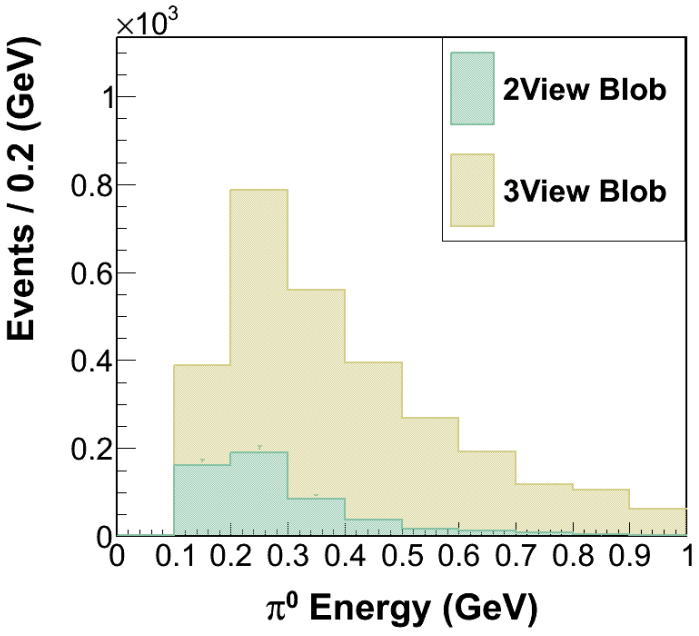

Figure B.11: The $CC\pi^0$ inclusive sample has 2775 events reconstructed with the 3 views (83%) and 551 events reconstructed with only 2 views (17%).

Appendix C

Electron and Gamma Discrimination using dE/dx

In order to test our π^0 reconstruction we apply the dE/dx technique to our reconstructed gammas from data and Monte Carlo. dE/dx tool is good for the identification of particles in EM showers. This technique was proposed to identify and separate photons from electrons in neutrino oscillation experiments where it is necessary to find if an electromagnetic shower is originated from a photon or from an electron.

Since a photon produces an electron-positron pair the energy deposition must be twice the electron energy deposition. Figure C.1 shows the dE/dx mean value predicted by our Monte Carlo and the value calculated from the michel electron sample (data - Monte Carlo).

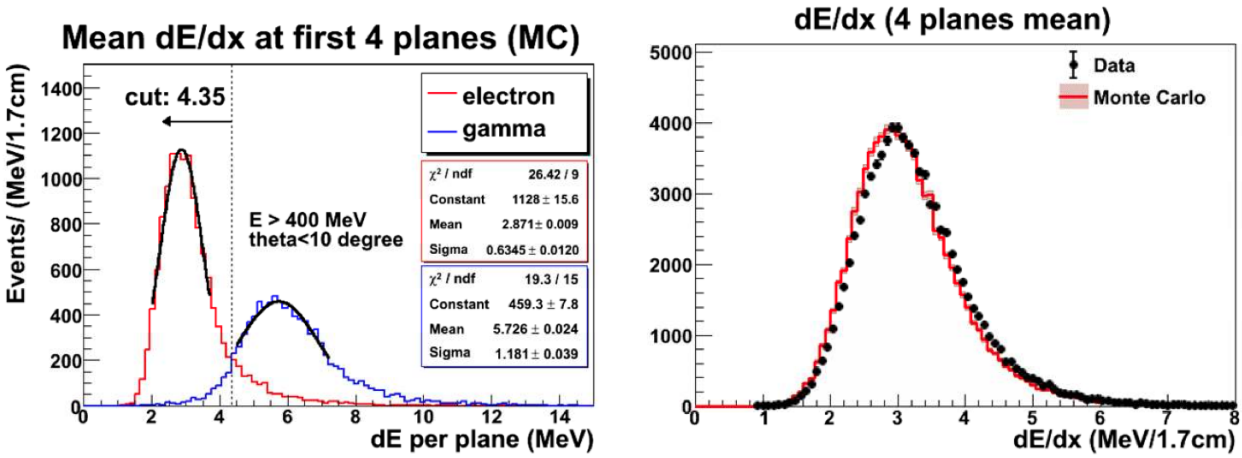

Figure C.1: Left: Monte Carlo prediction for average dE/dx in the first 4 planes. Right: Average dE/dx for Michel electrons. Figure courtesy of J. Park.

dE/dx mean value over the first 4 planes[1] from vertex is calculated according to,

$$\frac{dE}{dx} = \frac{1}{4}\sum_{i=1}^{4} dE_i \tag{C.1}$$

where dE_i is the energy loss in the i-th plane (i=1,2,3,4). We use our π^0 reconstruction to isolate γ coming from the π^0 decay from $CC\pi^0$ inclusive sample (figure C.2) and $CC\pi^0$ exclusive sample (figure C.3). We then apply the dE/dx calculation to both samples.

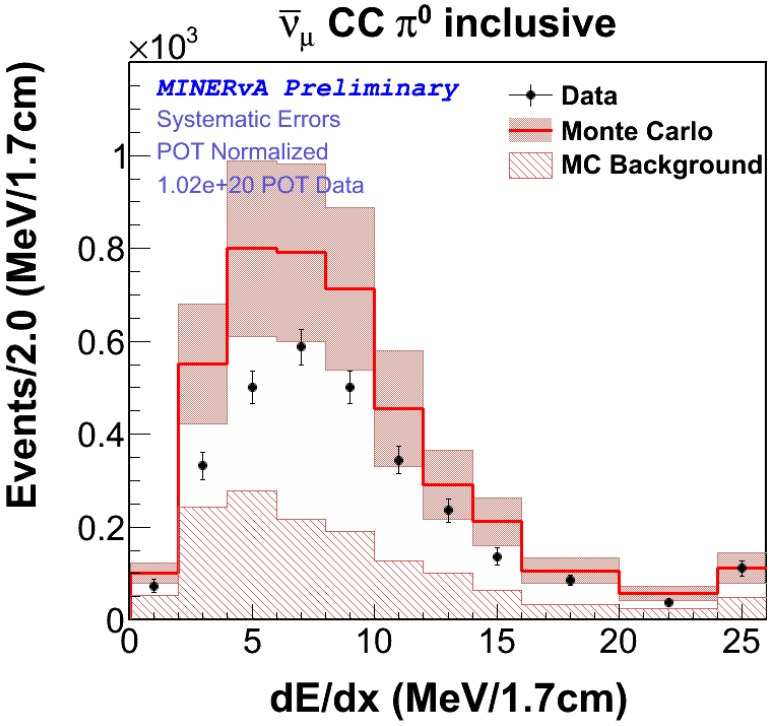

Figure C.2: $CC\pi^0$ inclusive sample. dE/dx calculated for photons from the π^0 decay. Monte Carlo and data. Monte Carlo background is shifting the peak position

The $CC\pi^0$ exclusive sample shows a better agreement between data and Monte Carlo. Note that the $CC\pi^0$ exclusive sample contains an almost pure sample of π^0. It is more difficult to reconstruct a π^0 in the $CC\pi^0$ inclusive sample.

Future oscillation experiments ($\nu_\mu - \nu_e$) can apply this technique to reduce the main source of background. Experiments looking for ν_e signal usually mis-reconstruct a γ coming from the π^0 decay as an electron.

[1]Plane distance in MINERνA is 1.7cm

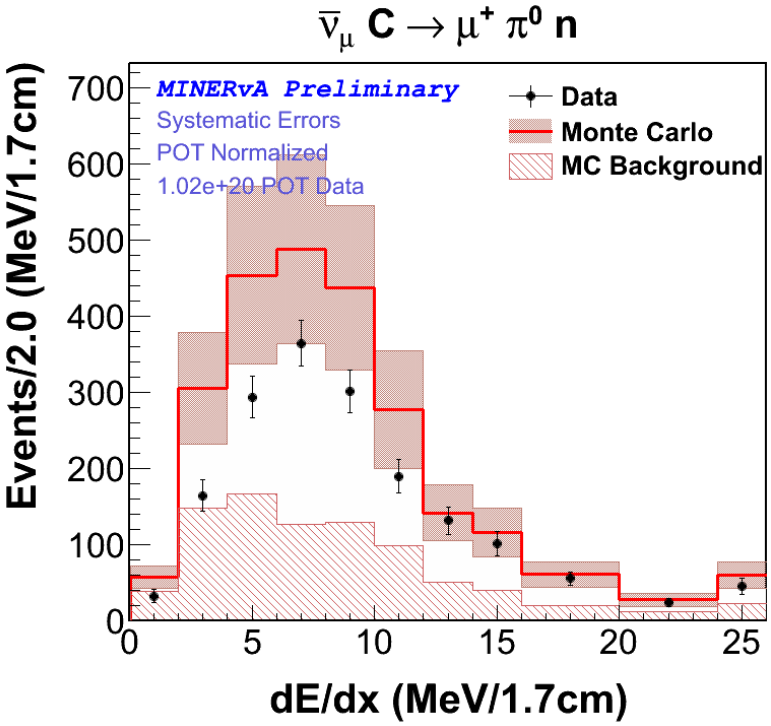

Figure C.3: $CC\pi^0$ exclusive sample. dE/dx calculated for photons from the π^0 decay. Monte Carlo an data. This sample shows a better agreement due to its higher π^0 purity.

Bibliography

[1] Karagiorgi, G.A. Aguilar-Arevalo, J.M. Conrad, and M.H. Shaevitz. Leptonic CP violation studies at MiniBooNE in the (3+2) sterile neutrino oscillation hypothesis, Phys Rev D 75 (2007)1.

[2] Z. Maki, M. Nakagawa, and S. Sakata, Prog. Theor. Phys. 28, 870 (1962).

[3] von Bayer, O. Hahn, L. Meitner, Phys. Zeitschrift, 12, January, 1911, p. 378

[4] C.D. Ellis, B.A. Wooster, The average energy of desintegration of Radium E,Proc. Roy. Soc. A117(1927) 109-123

[5] W. Pauli, carta enviada à Conferência de Tubingen, Dec. 1930.

[6] J. Chadwick, Possible existence of a neutron, Nature 129 (1932)12.

[7] E. Fermi, Ricercha Scient.**2** 12(1933).

[8] F.Perrin, Comptes rendues **197**, 1624(1933).

[9] E. Fermi, Z. Physik, **88** 161(1934).

[10] F. Reines and C.L. Cowan, The neutrino, Nature 178 (1956)446.

[11] M. Goldhaber, L. Grodzins, and A.W. Sunyar, Helicity of neutrinos, Phys. Rev. 109 (1958)1015.

[12] R. Davis and D.S. Harmer, Attempt to Observe the $Cl^37(\overline{\nu},e^-)Ar^37$ Reaction Induced by Reactor Antineutrinos, Bull. Am. Phys. Soc. 4, (1959)217.

[13] G. Danby et al., Observation of high-energy neutrino reactions and the existence of two kinds of neutrinos, Phys. Rev. Lett. 9 (1962)36.

[14] Gargamelle Neutrino Collaboration: F.J. Hasert et al., Observation of neutrino-like interactions without muon or electron in the Gargamelle neutrino experiment, Phys. Lett. B **46** (1973)138.

[15] R. Davis,D.S. Harner, and K.C. Hoffman, Search for neutrinos from the sun, Phys. Rev. Lett. 20 (1968)1205.

[16] V.N. Gribov and B. Pontecorvo, Phys. Lett B **28**(1969)493.

[17] DONUT COllaboration: T. Patzak, First direct observation of the tau neutrino, Europhys. News 32, 56 (2001).

[18] ALEPH Collaboration:D. Decamp et al., Determination of the Number of Light Neutrino Species, Phys. Lett. B **231**(1989)519.

[19] Delphi Collaboration:P.A. Aarnio et al.,Measurement of the Mass and Width of the Z0 Paricle from Multi-Hadronic Final States Produced in the e+ e- Annihilation, Phys. Lett. B **231** (1989)539.

[20] L3 Collaboration:B. Adeva et al.,A Determination of the Properties of the Neutral Intermediate Vector Boson Z0, phys. Lett. B **231** (1989)509.

[21] OPAL Collaboration:M.Z. Akrawy et al.,Measurement of the Z0 Mass and Width with the OPAL Detector at LEP, Phys. Lett. B bf 231 (1989)530.

[22] C. Athanassopoulos et ala., Candidate Events in a Search for Anti-Muon-Neutrino -> Anti-Electron-Neutrino Oscillations, Phys. Rev. Lett. 75, 2650, 1995.

[23] C.S. Wu et al., Phys. Rev. **105** (1957)1413.

[24] C. W. Kim, Neutrino Physics: Fundamentals of Neutrino Oscillations, Proceedings J. Korean Phys. Soc., Suppl. 1996. hep-ph/9607391

[25] A. W. Thomas and W. Weise, The Structure of the Nucleon, Wiley- VCH, Berlin, 2001

[26] 't Hooft, G., 1971, Phys. Lett. B 37, 195.

[27] J. Beringer et al. (Particle Data Group), Phys. Rev. D86, 010001 (2012).

[28] G. Aad et al. ATLAS Collaboration, "Observation of a new particle in the search for the Standard Model Higgs boson with the ATLAS detector at the LHC" Phys. Lett. B 716, 1 (2012) arXiv:1207.7214 (hep-ex)

[29] S. Chatrchyan et al. CMS Collaboration, "Observation of a new boson at a mass of 125 GeV with the CMS experiment at the LHC" Phys. Lett. B 716, 30 (2012) arXiv:1207.7235 (hep-ex).

[30] A. Salam, 1969, Proc. of the 8th Nobel Symposium on Elementary Particle Theory, Relativistic Groups and Analyticity, Stockholm, Sweden, 1968, edited by N. Svartholm, p. 367-377.

[31] S. Weinberg, Phys. Rev. Lett., 19, 1264-1266, 1967.
,

[32] http://minerva-docdb.fnal.gov/cgi-bin/ShowDocument?docid=6069

[33] J. A. Formaggio, G. P. Zeller, From eV to EeV: Neutrino cross sections across energy scales, Rev. Mod. Phys.: Volume 84.1307 (2012).

[34] C. H. Llewellyn Smith, Neutrino reactions at accelerator energies, Phys. Rept. 3 (1972) 261.

[35] Bernard, V., et al., 2002, J. Phys. G 28, R1.

[36] Smith, R. A., and E. J. Moniz, 1972, Nucl. Phys. B43, 605.

[37] Allasia, D., et al. (Amsterdam-Bologna-Padua-Pisa-Saclay-Turin Collaboration), 1983, Z. Phys. C 20, 95.

[38] Allen, P., et al. (Aachen-Birmingham-Bonn-CERN-London-Munich-Oxford Collaboration), 1986, Nucl. Phys. B264, 221.

[39] Jones, G., et al. (WA21 Collaboration, Birmingham-CERN-Imperial-Coll-Munich-Oxford-University Coll Collaboration), 1989, Z. Phys. C 43, 527.

[40] Barish, S., et al., 1980, Phys. Lett. B 91, 161.

[41] Bolognese, T., J. Engel, J. Guyonnet, and J. Riester, 1979, Phys. Lett. B 81, 393.

[42] Grabosch, H., et al. (SKAT Collaboration), 1989, Z. Phys. C 41, 527.

[43] Barish, S., et al., 1974, Phys. Rev. Lett. 33, 1446.

[44] Barish, S. J., et al., 1974, Phys. Rev. Lett. 33, 448.

[45] Derrick, M., et al., 1981, Phys. Rev. D 23, 569.

[46] Fogli, G. L., and G. Nardulli, 1980, Nucl. Phys. B165, 162.

[47] Krenz, W., et al., 1978a, Nucl. Phys. B135, 45.

[48] Lee, W., et al., 1977, Phys. Rev. Lett. 38, 202.

[49] Nienaber, P., 1988, Ph.D. thesis, (Univerity of Illinois at Urbana-Champaign).

[50] Nakayama, S., et al., 2005, Phys. Lett. B 619, 255.

[51] Rodriguez, A., et al., 2008, Phys. Rev. D 78, 032003.

[52] Mariani, C., et al., 2011, Phys. Rev. D 83, 054023.

[53] Aguilar-Arevalo, A. A., et al., 2009, Phys. Rev. Lett. 103, 081801.

[54] Aguilar-Arevalo, A. A., et al., 2010, Phys. Rev. D 81, 013005.

[55] Aguilar-Arevalo, A. A., et al., 2011a, Phys. Rev. D 83, 052007.

[56] A. A. Aguilar-Arevalo et al., Measurement of ν-induced charged-current neutral pion production cross sections on mineral oil at E 0.5-2.0 GeV, Phys. Rev. D 83, 052009 (2011)

[57] Kurimoto, Y., et al., 2010a, Phys. Rev. D 81, 033004.

[58] Robert H. Nelson, CCpi0 Event Reconstruction at MiniBooNE, AIP Conf.Proc.1189:201-206,2009

[59] Baker, N., et al., 1982, Phys. Rev. D 25, 617.

[60] Baranov, D., et al., 1979, Phys. Lett. B 81, 255.

[61] Ciampolillo, S., et al. (Gargamelle Neutrino Propane Collaboration, Aachen-Brussels-CERN-Ecole Poly-Orsay-Padua Collaboration), 1979, Phys. Lett. B 84, 281.

[62] Nakajima, Y., et al. (SciBooNE Collaboration), 2011, Phys. Rev. D 83, 012005.

[63] J. Hylen et al., NuMI Technical Design Handbook, Internal NuMI report (2003).

[64] R. M. Zwaska, Accelerator Systems and Instrumentation for the NuMI Neutrino Beam, PhD thesis University of Texas at Austin, 2005.

[65] FLUKA: A. Ferrari, P.R. Sala, A. Fasso, and J. Ranft, CERN-2005-10 (2005), INFN/TC 05/11, SLAC-R-773

[66] http://minerva-docdb.fnal.gov:8080/cgi-bin/ShowDocument?docid=2169

[67] H. Kluttig, J.G. Morfin e W.Van Doninck, Phys.Lett. B**71** (1977),446.

[68] O. Erriquez et al., Phys. Lett. B **73** (1978)350.

[69] W. Krenz et al.,Nucl. Phys. B**135** (1978)45.

[70] M. Pohl et al., Phys. Lett. B**82** (1979)461.

[71] W.-Y. Lee et al.,Phys. Rev. Lett. **38** (1977)202.

[72] S.J. Barrish et al., Phys. Rev. Lett **33** (1974)448.

[73] M. Derrick et al., Phys. Lett B **92** (1980)363.

[74] M. Derrick et al., Phys. Lett B **23** (1981)569.

[75] N.J. Baker et al., Phys. Rev. D **23** (1981)2495.

[76] HOUGH , P. V. C. Method and means for recognizing complex patterns. U. S. Patent 3, 069 654, December 18, 1962.

[77] Duda, R. O. and P. E. Hart, Use of the Hough Transformation to Detect Lines and Curves in Pictures, Comm. ACM, Vol. 15, pp. 11 15 January, 1972

[78] Sotelo,C. Reconstrução de π^0 no Experimento MINERνA , Master thesis (in Portuguese), CBPF (2012)

[79] C. Andreopoulos, A. Bell, D. Bhattacharya, F. Cavanna, J. Dobson, S. Dytman, H. Gallagher, P. Guzowski, R. Hatcher, P. Kehayias, A. Meregaglia, D. Naples, G. Pearce, A. Rubbia, M. Whalley, T. Yang, The GENIE Neutrino Monte Carlo Generator, Nucl. Instrum. Meth. A614:87-104, 2010.

[80] J. Allison et al., IEEE Transactions on Nuclear Science 53 No. 1 (2006) 270-278.

[81] J.B. Birks, Proc. Phys. Soc. A64: 874 (1951)

[82] J. Chvojka. Anti-Neutrino Charged Current Quasi-Elastic Scattering in MINERνA , Doctoral Thesis, University of Rochester(2012).

[83] Mike Kordosky, et al. MINERνA Technical Note No. 004: A brief documentation of the flux, available at http://minerva-docdb.fnal.gov:8080/cgi-bin/ShowDocument?docid=7634

[84] C. Alt et al., Inclusive production of charged pions in p + C collisions at 158 GeV/c beam momentum. Eur. Phys. J. C 49, 897917 (2007).

[85] D.S. Barton et al. Experimental study of the A dependence of inclusive hadron fragmentation, Phys. Rew. D Vol27 N 11.

[86] ROOT Collaboration, http:root.cern.ch.

[87] L. A. Ahrens, et al., Measurement of Neutrino - Proton and anti-neutrino - Proton Elastic Scattering, Phys. Rev. D35 (1987) 785.

[88] D. Rein and L. M. Sehgal, Neutrino Excitation Of Baryon Resonances And Single Pion Production, Annals Phys. 133, 79 (1981)

[89] R. P. Feynman, M. Kislinger, F. Ravndal, Current matrix elements from a relativistic quark model, Phys. Rev. D3 (1971) 2706-2732.

[90] D. Rein, L. M. Sehgal, Coherent π^0 production in neutrino reactions, Nucl. Phys. B223 (1983) 29.

[91] A. Bodek, I. Park and U. -k. Yang, Improved low Q2 model for neutrino and electron nucleon cross sections in few GeV region, Nucl. Phys. Proc. Suppl. 139, 113 (2005).

[92] W. J. Marciano, Z. Parsa, Neutrino-electron scattering theory, J. Phys. G29 (2003) 2629-2645.

[93] J. W. J. Williams. "Algorithm 232 - Heapsort", Communications of the ACM 7(6): 347348, (1964).

[94] R. Fruhwirth, Application of Kalman Filtering to Track and Vertex Fitting, Nucl. Instrum. Meth. A262 444-450, (1987).

[95] http://minerva-docdb.fnal.gov:8080/cgi-bin/ShowDocument?docid=8136

[96] G. D' Agostini A multidimensional unfolding method based on Baye′s theorem, Nucl. Instrum. Methods in Phys. Res. Sect. A 362 (1995) 487-49

[97] Ronald Ransome,available at http://minerva-docdb.fnal.gov:8080/cgi-bin/ShowDocument?docid=6016

[98] David W. Schmitz, MINERÎ$\frac{1}{2}$A Technical Note No. 008:Handling event generator uncertainties in a xsec analysis. available at http://minerva-docdb.fnal.gov:8080/cgi-bin/ShowDocument?docid=8151,

[99] Arturo Fiorentin, available at http://minerva-docdb.fnal.gov:8080/cgi-bin/ShowDocument?docid=7851

[100] Jeff Nelson, available at http://minerva-docdb.fnal.gov:8080/cgi-bin/ShowDocument?docid=7573